

CRASHWORTHINESS DESIGN OPTIMIZATION USING  
SURROGATE MODELS

by

CHENG-HO THO

Presented to the Faculty of the Graduate School of  
The University of Texas at Arlington in Partial Fulfillment  
of the Requirements  
for the Degree of

DOCTOR OF PHILOSOPHY

THE UNIVERSITY OF TEXAS AT ARLINGTON

August 2006

Copyright © by Cheng-Ho Tho 2006

All Rights Reserved

## ACKNOWLEDGEMENTS

First and foremost, the author wishes to express his deepest appreciation to Dr. Bo Ping Wang for his excellent guidance and supervision throughout the course of this dissertation. This dissertation would not have been completed without his constant inspiration and encouragement.

Special thanks to Dr. Wen S. Chan, Dr. Kent Lawrence, Dr. Seiichi Nomura, and Dr. Bill Corley for their time in serving as my committee members and providing me valuable comments and suggestions regarding this dissertation.

The author would like to thank the following personnel at Bell Helicopter Textron Inc. for their constant encouragement and support: Mr. Michael Smith, Dr. Ashish Sareen, Mr. David Popelka (Chief of Dynamics), Mr. Martin Peryea (former Director of Flight Technology and Simulation).

Many thanks are also due to the former colleagues and members of Safety and Optimization group at Ford Research Laboratory, especially Dr. Lei Gu and Dr. Ren-Jye Yang. Some of the work in this dissertation was evolved from the author's previous research work at the automotive industry. The author also would like to acknowledge Dr. Heung-Soo Kim and Professor Tomasz Wierzbicki of Impact and Crashworthiness Laboratory at Massachusetts Institute of Technology for the collaborative research on the foam-filled front rail optimization problem.

Finally, the author would like to dedicate this work to his parents, his family, and his girlfriend, Yindi, for their endless encouragement, understanding, love and support.

July 5, 2006

## ABSTRACT

### CRASHWORTHINESS DESIGN OPTIMIZATION USING SURROGATE MODELS

Publication No. \_\_\_\_\_

Cheng-Ho Tho, PhD.

The University of Texas at Arlington, 2006

Supervising Professor: Bo Ping Wang

Despite the advances in computer technology, the enormous computational cost associated with the large-scale and complex nonlinear crashworthiness simulations renders it to be impractical to rely exclusively on computer simulations for crashworthiness design optimization. A preferable strategy is to employ the computational efficient surrogate model in lieu of the expensive simulations to facilitate the optimization process and design concept exploration. An added advantage of the surrogate models is that they tends to eliminate the high-frequency numerical noise which may hinder the performance of the direct gradient-based optimization technique by constructing smooth crash responses in the crashworthiness analysis.

Even though the Design of Experiments with Response Surface Methodology technique has shown to be a promising way for crashworthiness design optimization over the years, it is still hampered by large number of function evaluations for large number of design variables or low numerical accuracy for small sample sizes. In this dissertation, we propose and develop an effective methodology based upon the sequential regularized multiquadric with output space mapping to reduce the computational cost. The proposed method overcomes the ill-conditioning of the coefficient matrix in the generalized multiquadric function for duplicate data when approaching to the optimal design. Unlike the traditional DOE/RSM methodology, the sampling point is added sequentially and thus becomes more manageable to deal with problems involving large number of design variables. Several numerical examples are employed to demonstrate the effectiveness and robustness of the methodology, including a large-scale full vehicle frontal impact problem and a helicopter skid landing gear hard landing problem. It is shown that the proposed SRMQ/OSM method reduces the computational cost by 50~70% as compared to the traditional DOE/RSM based methodology or direct gradient-based optimization technique.

In addition, this dissertation investigates and implements the Implicit Space Mapping optimization algorithm for solving the nonlinear crashworthiness design optimization problems.

## TABLE OF CONTENTS

ACKNOWLEDGEMENTS.....	iii
ABSTRACT .....	v
LIST OF ILLUSTRATIONS.....	xiii
LIST OF TABLES.....	xx
Chapter	Page
1. INTRODUCTION .....	1
1.1 Objective and Motivation .....	2
1.2 Literature Review of Crashworthiness Optimization .....	3
1.2.1 Gradient-Based Crashworthiness Optimization.....	3
1.2.2 Design of Experiment and Response Surface Based Crashworthiness Optimization .....	4
1.2.3 Successive or Sequential Crashworthiness Optimization.....	6
1.3 Contributions .....	7
1.4 Outline of Dissertation.....	8
2. FUNDAMENTAL OF NONLINEAR CRASHWORTHINESS ANALYSIS .....	10
2.1 Introduction.....	10
2.2 Explicit Formulation of Transient Dynamics .....	11
2.2.1 Governing Equations.....	12
2.2.2 Variational Principle .....	13

2.2.3 Discretized Variational Principle.....	14
2.3 Explicit Time Marching Integration .....	15
2.4 Elements for Crashworthiness Analysis .....	19
2.5 Contact-Impact Algorithm.....	21
2.6 Crashworthiness in Aerospace Industry .....	21
2.7 Crashworthiness in Automotive Industry .....	23
2.8 Column Collapse Modes Under Crush Loadings .....	25
2.8.1 Axial Collapse Mode .....	25
2.8.2 Bending Collapse Mode.....	27
2.9 Dynamic Effect on the Crash Resistance.....	30
3. CRASHWORTHINESS OPTIMIZATION USING DESIGN OF EXPERIMENTS AND RESPONSE SURFACE METHODOLOGY .....	33
3.1 Introduction.....	33
3.2 Design of Experiments .....	37
3.2.1 Latin Hypercube Sampling.....	38
3.2.2 Uniform Design .....	39
3.2.3 Halton Sequence .....	39
3.2.4 Sobol Sequence.....	42
3.2.5 Faure Sequence.....	43
3.3 Surrogate Models.....	44
3.3.1 Polynomial Regression .....	44
3.3.2 Stepwise Regression .....	45
3.3.2.1 Forward Selection.....	46



3.3.2.2 Backward Deletion .....	46
3.3.3 Moving Least Square .....	47
3.3.4 Kriging .....	48
3.3.5 Radial Basis Function .....	50
3.3.6 Adaptive and Interactive Modeling System (AIMS) .....	52
3.3.7 Multivariate Adaptive Regression Splines (MARS) .....	54
3.4 Comparative Study of Surrogate Models .....	55
3.4.1 Introduction .....	55
3.4.2 Finite Element Model .....	56
3.4.3 Numerical Results .....	57
3.5 Aluminum Foam-Filled Front Rail Impact Optimization .....	65
3.5.1 Introduction .....	65
3.5.2 Finite Element Model .....	65
3.5.3 Surrogate-Based Optimization Algorithm .....	68
3.5.4 Numerical Results .....	71
3.5.5 Weight Efficiency .....	74
3.6 Full Vehicle Multidisciplinary Design Optimization .....	76
3.6.1 Introduction .....	76
3.6.2 MDO Problem Formulation .....	78
3.6.3 MDO Procedure .....	80
3.6.4 MDO Numerical Results .....	83
3.7 Conclusions .....	86

4. SEQUENTIAL REGULARIZED MULTIQUADRIC AND OUTPUT SPACE MAPPING .....	87
4.1 Introduction.....	87
4.2 Regularized Multiquadric .....	89
4.3 Proposed Algorithms for Crashworthiness Optimization.....	93
4.3.1 Sequential Regularized Multiquadric (SRMQ).....	93
4.3.2 Sequential Regularized Multiquadric with Output Space Mapping.....	95
4.4 Numerical Examples .....	97
4.4.1 One Dimensional Function .....	97
4.4.2 Two Dimensional Function.....	105
4.5 Rectangular Tube Crush Optimization Problem.....	108
4.5.1 Finite Element Model.....	108
4.5.2 Problem Definition.....	109
4.5.3 Numerical Results .....	110
5. LARGE-SCALE SYSTEM OPTIMIZATION USING SRMQ/OSM ALGORITHM .....	119
5.1 Helicopter Skid Landing Gear Hard Landing Optimization.....	119
5.1.1 Design Considerations .....	119
5.1.1.1 Crashworthiness Considerations .....	120
5.1.1.2 Ground Resonance Frequency Considerations.....	121
5.1.2 Finite Element Model .....	122
5.1.3 Problem Definition .....	125

5.1.4 Numerical Results.....	128
5.1.5 Concluding Remarks .....	138
5.2 Full Vehicle Frontal Impact Optimization.....	140
5.2.1 Finite Element Model .....	140
5.2.2 Problem Definition .....	141
5.2.3 Numerical Results .....	143
5.2.4 Concluding Remarks .....	150
6. IMPLICIT SPACE MAPPING CRASHWORTHINESS OPTIMIZATION.....	151
6.1 Introduction.....	151
6.2 Review of Space Mapping Optimization Algorithm.....	153
6.2.1 Space Mapping Optimization Basic Concepts.....	153
6.2.2 Original Space Mapping Optimization Algorithm.....	154
6.2.3 Aggressive Space Mapping (ASM) Optimization Algorithm .....	156
6.2.4 Thrust Region Aggressive Space Mapping (TRASM) Optimization Algorithm.....	157
6.3 Rectangular Tube Crush Optimization Using Implicit Space Mapping .....	158
6.3.1 Implicit Space Mapping Optimization Algorithm .....	159
6.3.2 Finite Element Models .....	161
6.3.3 Problem Definition.....	164
6.3.4 Numerical Results .....	166
6.4 Conclusions.....	178

7. CONCLUSIONS AND RECOMMENDATIONS.....	179
7.1 Conclusions.....	179
7.2 Recommendations for Future Study .....	180
Appendix	
A. DERIVATION OF THE GENERAL FORM OF THE REGULARIZATON THEORY .....	181
B. COMPUTER INTEGRATION IMPLEMENTATION FOR IMPLICIT SPACE MAPPING OPTIMIZAION ALGORITHM.....	185
REFERENCES .....	187
BIOGRAPHICAL INFORMATION.....	199

## LIST OF ILLUSTRATIONS

Figure	Page
2.1 Notation for System of Equations .....	13
2.2 Critical Time Step Comparison for Explicit and Implicit Techniques in Nonlinear Finite Element Analysis.....	16
2.3 Schematic of Explicit Time Marching Integration.....	17
2.4 Critical Time Step Factors for Shell and Solid Elements.....	19
2.5 Schematic of Surface-to-Surface and Self-Surface Contact Algorithms: (a) Surface-to-Surface Contact, (b) Self-Surface Contact .....	21
2.6 Crash Energy Absorption Approaches for Various Types of Aircraft.....	23
2.7 Crashworthiness Applications in Aerospace Industry: (a) ATR42 Commuter, (b) Helicopter Composite Fuselage, (c) Rotorcraft Water Impact.....	23
2.8 Crashworthiness Applications in Automotive Industry: (a) Frontal Offset Impact, (b) Side Impact, (c) Occupant Restraint System.....	25
2.9 Axial Collapse Mode of Column under Axial Crush Loading.....	26
2.10 Bending Collapse Mode of Column under Moment Crush Loading .....	28
3.1 Schematic of Design of Experiments and Response Surface Methodology Based Computer Simulations .....	35
3.2 An Illustrative Sampling Example Using Scrambled Halton Sequence: (a) Before Scrambling, (b) After Scrambling .....	41
3.3 Frontal Impact Finite Element Model and Selected Design Variables for Comparative Study of Surrogate Models.....	55

3.4	Occupant Restraint System Model to Evaluate Injury Numbers for Comparative Study of Surrogate Models.....	57
3.5	RMS Error vs. Sample Size for Toe-Board Intrusion in the Frontal Impact Problem: (a) Real Scale, (b) Log-Log Scale.....	61
3.6	RMS Error vs. Sample Size for HIC Injury Number Predicted by Occupant Restraint System Analysis in the Frontal Impact Problem: (a) Real Scale, (b) Log-Log Scale.....	62
3.7	Surface Plot Comparison for Normalized Toe-Board Intrusion Using 36 <i>N</i> Sample Size in Frontal Impact Problem .....	63
3.8	Surface Plot Comparison for Normalized HIC Injury Number Using 36 <i>N</i> Sample Size in Frontal Impact Problem .....	64
3.9	Front Rail Finite Element Model .....	66
3.10	Mechanical Properties of Aluminum Foam under Compression .....	67
3.11	Surrogate-Based Optimization Algorithm .....	70
3.12	Rigid Wall Forces of Optimal Designs and Original Baseline Model for Aluminum Foam-Filled Front Rail .....	74
3.13	Comparison of the Specific Energy Absorption between Original Baseline Design and Foam-Filled Optimal Designs .....	75
3.14	Relation Between Structural Weight and Energy Absorption .....	76
3.15	NVH and Crashworthiness Finite Element Models for Multidisciplinary Design Optimization.....	78
3.16	Multidisciplinary Design Optimization Data Flow .....	80
3.17	Multidisciplinary Design Optimization Flow Chart .....	82
3.18	Objective and Constraint Design History for Multidisciplinary Design Optimization.....	84
3.19	DOE Matrix for Frontal Crash ( $P_{total}$ vs. Weight) .....	85

3.20	DOE Matrix for Offset Crash (Maximum Intrusion vs. Weight).....	85
4.1	Flow Chart for SRMQ Optimization Algorithm.....	94
4.2	Flow Chart for SRMQ/OSM Optimization Algorithm .....	96
4.3	One Dimensional Problem Using SRMQ/OSM Optimization Algorithm (Sampling Points: $x=0.5, 1.5$ ): (a) 1 <sup>st</sup> Iteration, (b) 2 <sup>nd</sup> Iteration, (c) 3 <sup>rd</sup> Iteration, (d) 4 <sup>th</sup> Iteration, (e) 5 <sup>th</sup> Iteration, (f) 6 <sup>th</sup> Iteration .....	100
4.4	One Dimensional Problem Using SRMQ/OSM Optimization Algorithm (Sampling Points: $x=4, 6$ ): (a) 1 <sup>st</sup> Iteration, (b) 2 <sup>nd</sup> Iteration, (c) 3 <sup>rd</sup> Iteration, (d) 4 <sup>th</sup> Iteration, (e) 7 <sup>th</sup> Iteration.....	101
4.5	Correction Factor for One Dimensional Problem Using SRMQ/OSM Optimization Algorithm: (a) $x = 0.5, 1.5$ , (b) $x = 4, 6$ .....	102
4.6	Logarithm Regularized Parameter vs. Absolute Error Percentage .....	103
4.7	Surface Plot of the Two Dimensional Peak Function .....	106
4.8	The Peak Function Using SRMQ/OSM (3 Sampling Points, $r=1 \times 10^{-3}$ ) .....	106
4.9	The Peak Function Using SRMQ/OSM (3 Sampling Points, $r=1 \times 10^{-6}$ ) .....	107
4.10	The Peak Function Using SRMQ/OSM (4 Sampling Points, $r=1 \times 10^{-6}$ ) .....	107
4.11	LS-DYNA Finite Element Model of the Rectangular Tube Crush Problem .....	109
4.12	Design History Comparisons for Objective Function Using SRMQ, SRMQ/OSM, ISM, Direct and Hybrid Optimization Methods.....	112
4.13	Design Constraint History Using SRMQ/OSM Optimization Method .....	113

4.14	Design Constraint History Using SRMQ Optimization Method .....	113
4.15	Design Constraint History Using Direct Optimization Method.....	114
4.16	Design Variable History Using SRMQ/OSM Optimization Method .....	115
4.17	Design Variable History Using SRMQ Optimization Method .....	115
4.18	Design Variable History Using Direct Optimization Method.....	116
4.19	Rigid Wall Force Comparisons Using SRMQ, SRMQ/OSM, ISM, Direct and Hybrid Optimization Methods.....	117
4.20	Internal Energy Comparisons Using SRMQ, SRMQ/OSM, ISM, Direct and Hybrid Optimization Methods.....	117
5.1	Helicopter Skid Landing Gear LS-DYNA Finite Element Model .....	124
5.2	Design Variables for Hollow Rectangular Cross-Section Crosstube .....	126
5.3	Design Domain and DOE Design Sampling for Design Variables 10 and 11 Generated by Halton Sequence.....	127
5.4	Objective Function Design History for Helicopter Skid Landing Gear Optimization Problem.....	129
5.5	Constraint Function Design History for Helicopter Skid Landing Gear Optimization Problem.....	130
5.6	Normalized Fuselage CG Acceleration (Initial vs. Optimum).....	131
5.7	Normalized Crossbeam Attachment Fitting Force (Initial vs. Optimum): (a) Fwd Crossbeam, (b) Aft Crossbeam.....	133
5.8	Normalized Crossbeam Deformation (Initial vs. Optimum): (a) Fwd Crossbeam, (b) Aft Crossbeam.....	134
5.9	Normalized Crossbeam Strain Energy (Initial vs. Optimum).....	135



5.10	Structural Impact Sequence of Helicopter Skid Landing Gear (Initial vs. Optimum): (a) Initial, (b) Optimum.....	136
5.11	C2500 Pick-Up LS-DYNA Frontal Impact Finite Element Model .....	140
5.12	C2500 Pick-Up 35 mph Frontal Impact Test Correlation .....	141
5.13	Thickness and Material Design Variables for Full Vehicle Frontal Impact Optimization Problem .....	142
5.14	Full Vehicle Frontal Impact Design Domain and DOE Sampling for Design Variables 7 and 10 Generated by Halton Sequence .....	143
5.15	Objective Function Design History for Full Vehicle Frontal Impact Using SRMQ/OSM Optimization Algorithm.....	144
5.16	Constraint Function Design History for Full Vehicle Frontal Impact Using SRMQ/OSM Optimization Algorithm.....	145
5.17	Original and Final Specific Internal Energy Comparison for Full Vehicle Frontal Impact Using SRMQ/OSM Optimization Algorithm .....	146
5.18	Original and Final Rigid Wall Force Comparison for Full Vehicle Frontal Impact Using SRMQ/OSM Optimization Algorithm .....	146
5.19	Left Seat Velocity (Original vs. Final) Comparison for Full Vehicle Frontal Impact Using SRMQ/OSM Optimization Algorithm .....	147
5.20	Left Seat Acceleration (Original vs. Final) Comparison for Full Vehicle Frontal Impact Using SRMQ/OSM Optimization Algorithm .....	147
6.1	Schematic of Implicit Space Mapping Optimization Algorithm Concepts .....	159
6.2	Implicit Space Mapping Optimization Algorithm .....	161
6.3	Fine LS-DYNA Finite Element Model for Rectangular Tube Crush Problem .....	163

6.4	Coarse LS-DYNA Finite Element Model Rectangular Tube Crush Problem .....	163
6.5	Plastic Strength Scale Factor for the Preassigned Parameter in the ISM Optimization Algorithm.....	165
6.6	Objective Function Design History for Rectangular Tube Crush Problem Using ISM Optimization Algorithm .....	168
6.7	Constraint Function Design History for Rectangular Tube Crush Problem Using ISM Optimization Algorithm .....	168
6.8	Design Variables and Preassigned Parameter Design History for Rectangular Tube Crush Problem Using ISM Optimization Algorithm .....	170
6.9	Original and Final Internal Energy Comparison for Rectangular Tube Crush Problem Using ISM Optimization Algorithm .....	171
6.10	Original and Final Rigid Wall Force Comparison for Rectangular Tube Crush Problem Using ISM Optimization Algorithm .....	172
6.11	Rigid Wall Force for Rectangular Tube Crush Problem Using ISM Optimization Algorithm: (a) Before ISM, (b) After ISM.....	174
6.12	Internal Energy for Rectangular Tube Crush Problem Using ISM Optimization Algorithm: (a) Before ISM, (b) After ISM.....	175
6.13	Original and Final Structural Deformation Comparison for Rectangular Tube Crush Problem Using ISM Optimization Algorithm .....	176
6.14	Original and Final Structural Crash Mode Comparison of Fine Model for Rectangular Tube Crush Problem Using ISM Optimization Algorithm .....	177
6.15	Original and Final Structural Crash Mode Comparison of Coarse Model for Rectangular Tube Crush Problem Using ISM Optimization Algorithm .....	177

B.1 Flow Chart for Implementation of ISM Based Crashworthiness Optimization Algorithm .....	186
--	-----

## LIST OF TABLES

Table	Page
2.1 Comparison of Explicit and Implicit Integration Techniques.....	15
2.2 Critical Time Step Factors for Shell and Solid Elements.....	18
3.1 An Illustrative Sampling Example Using Halton Sequence .....	41
3.2 Commonly Used Radial Basis Functions.....	52
3.3 Description of Design Variable, Lower Bound, Upper Bound and DOE Levels for Frontal Impact Problem.....	59
3.4 Model Accuracy Comparison Using RSM Error for Toe-Board Intrusion in Frontal Impact Problem.....	63
3.5 Model Accuracy Comparison Using RSM Error for HIC Injury Number in Frontal Impact Problem.....	64
3.6 Optimal LHS DOE matrix and Finite Element Response Matrix for Foam-Filled Front Rail Optimization Problem .....	71
3.7 Design History for Single Objective Formulation 1 .....	72
3.8 Design History for Single Objective Formulation 2 .....	73
3.9 Design History for Single Objective Formulation 3 .....	73
3.10 Design History for Multidisciplinary Design Optimization.....	84
4.1 Parametric Study for Prediction Error using Different Regularization Parameter $r$ .....	102
5.1 Design Variable Design History for Helicopter Skid Landing Gear Optimization Problem.....	137
5.2 Response Design History Using SRMQ Optimization Algorithm .....	138

5.3 Response Design History Using SRMQ/OSM Optimization Algorithm .....	138
5.4 DOE Matrix and Design Variable History for Full Vehicle Frontal Impact Using SRMQ/OSM Optimization Algorithm.....	148
5.5 Response Matrix and Design History for Full Vehicle Frontal Impact Using SRMQ/OSM Optimization Algorithm.....	149
6.1 Design History of Structure Weight and Internal Energy for Rectangular Tube Crush Problem Using ISM Optimization Algorithm .....	169
6.2 Design History of Normalized Constraints, SIE and Error Norm for Rectangular Tube Crush Problem Using ISM Optimization Algorithm .....	169
6.3 Design Variables and Preassigned Parameter Design History for Rectangular Tube Crush Problem Using ISM Optimization Algorithm .....	170

## CHAPTER 1

### INTRODUCTION

Nowadays, the manufacturing industry is continuously challenged by new ways of managing the design process yielding reduction in design cycle time, cost saving and product quality improvement. With the advances of computer technology, computer simulations for solving the highly nonlinear, transient-dynamic crashworthiness analysis have greatly been enhanced over the past decades. While the physical crash tests are extremely expensive, engineers, more than ever, are driven by using computer simulations to assist them in crashworthiness design and analysis to ultimately achieve the goal of ‘certification by analysis only’.

Computer simulations play a vital role particularly in the early preliminary design stage when several design concepts need to be evaluated. Traditional ways of using trial-and-error method and engineering experience have resulted in long design cycle time, high engineering cost and high risk of design turn back. Numerical design optimization offers a systematic way of assisting engineers in achieving a compromised, improved design in a shorter design cycle time. Over the years, there has been tremendous growing interest in developing strategies and methodologies for crashworthiness design optimization. Crashworthiness design optimization of large-scale systems, perhaps among the most challenging optimization problems, possesses

several inherent factors such as extremely long simulation time, noisy behavior, and unavailability of sensitivity analysis etc.

In recent years, the surrogate model based crashworthiness design optimization using the Design of Experiments (DOE) along with response surface methodology (RSM) has shown to be a promising method. The use of surrogate models or metamodeling has lead to new areas of research in simulation-based design optimization. Surrogate model based approaches have advantages over the traditional direct gradient-based optimization technique especially when dealing with the noisy responses and/or high computational cost characteristics of many computer simulations. However, the DOE/RSM method is still hampered by large number of function evaluations for large number of design variables or low accuracy for small sample size.

### 1.1 Objective and Motivation

There are two main thrusts in this dissertation.

1. Develop effective and robust surrogate model based optimization algorithms or framework for solving computational expensive simulation based optimization problems – using limited computational demands.
2. Implement and apply the developed algorithms to solve nonlinear crashworthiness design optimization problems for enhanced impact performance.

Even though the focus of this dissertation is on the crashworthiness design optimization problems, it is noted that the developed algorithms may be applied to tackle with other applications involving extensive simulation time such as the metal forming in the manufacturing process, drop impact of the electronic devices etc.

## 1.2 Literature Review of Crashworthiness Optimization

The literature for crashworthiness optimization is reviewed in this section. We broadly divide the crashworthiness optimization methods into the following three major categories:

1. Gradient-based crashworthiness optimization
2. Design of experiment and response surface based crashworthiness optimization
3. Successive or sequential crashworthiness optimization

### *1.2.1 Gradient-Based Crashworthiness Optimization*

Yang *et al.* (1994) [94] conducted the feasibility study of using the gradient-based numerical optimization technique to optimize a simplified vehicle front horn problem by integrating Pro/ENGINEER, PDA/PATRAN3, RADIOSS in the optimization algorithm. Both single- and multiple-objective formulations were used in the study and an improved design was achieved. They concluded that the crashworthiness optimization using the gradient-based approach is feasible but requires good quality of the finite element mesh during the design iterations.

Yang and Tho *et al.* (1999) [95] integrated an explicit crash code (FCRASH) and commercial available optimization package (iSIGHT) to solve a front rail crashworthiness optimization problem using three approaches: gradient-based, design of experiment/penalty/gradient-based, and design of experiment/penalty/ response surfaces. They found that the crash functions are very noisy and used 5% step size to compute the sensitivity using the finite difference method.



### *1.2.2 Design of Experiment and Response Surface Based Crashworthiness Optimization*

Etman *et al.* (1996) [24] adopted the sequential approximate optimization technique to deal with the noisy objective and constraint functions, as well as the high computational costs of the numerical analysis. In this work, the linear model functions are built based upon the responses calculated for a multipoint experimental design in a restricted design space. The linear programming is used to solve the optimization problem within the search subregion. In each iteration, the optimal solution obtained from previous iteration is used as the starting point of the approximate optimization.

Johnson *et al.* (1996) [42] demonstrated the use of regression and Kriging metamodels for surface estimation in multidimensional optimality analysis for linear programming. The methodology was demonstrated using a small example problem, a three source-four destination transportation problem and a multiperiod manufacturing problem. It was shown that these metamodels provide remarkably accurate predictions of the optimal objective function value.

Schramm and Thomas (1998) [77] attempted to use the sequential polynomial regression for crashworthiness design optimization problems. The quadratic polynomial is employed to construct the crash objective and constraint response surface functions globally. In their implementation, only a subset of the polynomial coefficients is computed depending on the number of design points and number of analyses in each of the design iteration.

Kurtaran *et al.* (2002) [52] applied the successive response surface approximation to solve the crashworthiness design optimization problems. In this

approach, the sizes of the successive subregions are highly influential on the accuracy of the approximations to be constructed. In general, the smaller the size of the subregion, the better the accuracy of the approximation. A scheme is adopted to determine the size of the subregions in their work.

Sobieski *et al.* (2000) [80] employed the response surface methodology to optimize the vehicle weight under the constraints of NVH (noise, vibration and harshness) and crash requirements. They reported a very significant reduction in elapsed computing time for such a large-scale multidisciplinary design optimization (MDO) problem (from 9 months to 1 day) through the efficient use of shared memory multiprocessor systems.

Kodiyalam *et al.* (2001) [50] extended Sobieski's previous work to increase the computational complexity by addressing multiple safety impact scenarios including frontal crash, offset crash, side impact and roof crush, in addition to the NVH discipline. The MDO problem was solved using multiple approximation models, sensitivity based approximation model for NVH responses and Kriging metamodels for the crash responses.

Miura *et al.* [61] attempted to combine the response surface methodology and numerical optimization technique in a commercial optimization, iSIGHT (Engineous Software), to improve the crash performance of a knee impact problem.

Craig *et al.* (2005) [21] employed a screening method based on the response surface methodology (linear) to select a reduced subset of design variables in the optimization process for the knee impact and frontal impact problems.

Lanzi *et al.* (2005) [53] used the response surface methodology constructed by radial basis functions and coupled with genetic algorithm to optimize the shape of composite absorbers with elliptical cross-sections under the impact requirements.

### *1.2.3 Successive or Sequential Crashworthiness Optimization*

Toropov *et al.* (1993) [87] attempted to use multipoint explicit approximations to fit objective and constraint functions and to reduce the total number of finite element analyses needed to solve the optimization problem. In each iteration, the subregion of the initial region in the design space, as defined by move limits, is chosen. Several design points are selected in this subregion, for which response analyses and design sensitivity analyses are carried out. The explicit expressions are formulated using the weighted least-squares method. The method was demonstrated to solve a MADYMO frontal impact problem.

Polynkin *et al.* (1995) [69] employed the multipoint approximation approach to solve the optimization of the geometrically nonlinear thin-walled structures. The approach is an iterative technique. The approximations are formulated by means of multiple regression analysis. In each iteration, the technique uses the results gained at several previous design points within a subregion as defined by the move limit.

Roux *et al.* (1998) [74] investigated the use of response surface methodology for structural optimization problems. They found that the approximation domain is the strongest determinant of the accuracy of the response surface. They claimed that the approximation accuracy can be improved by using a windowing strategy with a series of small regions. Substantial reduction in the approximation region, with corresponding

improvement in accuracy can be obtained by using a reasonable design strategy to limit the approximation domain.

### 1.3 Contributions

The author contributed substantially to the following original developments presented in this dissertation:

1. Proposed and developed an effective and robust framework based on the Sequential Regularized Multiquadric with Output Space Mapping (SRMQ/OSM) algorithm for solving large-scale, computational expensive simulation-based design optimization problems.
2. Implemented SRMQ/OSM algorithm by integrating the explicit nonlinear finite element code with the surrogate model in the numerical optimization framework.
3. Demonstrated the algorithm on several real-world crashworthiness applications including a helicopter skid landing gear hard surface impact optimization and a full vehicle frontal impact optimization problem.
4. Developed an efficient optimization framework based on the Implicit Space Mapping (ISM) technique for large-scale, nonlinear crashworthiness design optimization problems.
5. Implemented the ISM optimization technique by directly coupling with finite element code and demonstrated the algorithm for a rectangular tube crush optimization problem.

#### 1.4 Outline of Dissertation

The fundamental of the nonlinear crashworthiness analysis is presented in Chapter 2. The governing equation for solving the nonlinear finite element is given. A weak form solution in the sense of weighted residuals to convert the complex partial differential equation of motion, coupling with appropriate boundary conditions and initial conditions, is discussed. The comparison of using explicit and implicit techniques in the time marching algorithm is presented.

The design of experiments techniques to produce uniform sampling in exploring the design space as well as the surrogate model methods to construct “cheap-to-run”, smooth approximation responses are discussed in Chapter 3. A comparative study of surrogate models for a full vehicle frontal impact problem is given to pursuit a better understanding of the surrogate models and numerical behavior of the crash functions. The DOE/RSM technique is applied to optimize a foam-filled frontal rail impact problem as well as a full vehicle Multidisciplinary Design Optimization problem considering the noise, vibration and harshness (NVH), and crash function requirements.

Chapter 4 presents the sequential regularized multiquadric and output space mapping optimization (SRMQ/OSM) algorithms. The numerical behavior of the developed method is studied using several numerical examples including a rectangular tube crush optimization problem using the commercial nonlinear transient analysis code.

In Chapter 5, the SRMQ/OSM method is applied to solve for two large-scale optimization problems: helicopter skid landing gear impact optimization (an aerospace

industry application) and full vehicle frontal impact optimization (an automotive industry application). The numerical results of these two real-world applications by using the developed method are discussed.

The basic concepts and algorithms of the space mapping optimization are reviewed in Chapter 6, including the original space mapping, aggressive space mapping, trust region aggressive space mapping, and implicit space mapping. The crashworthiness design optimization based on the implicit space mapping technique is given in this chapter. The method is implemented and applied to solve a rectangular crush tube optimization problem by using the plastic strength scale factor as the preassigned parameter.

The conclusions along with recommendations for future research are given in Chapter 7.

## CHAPTER 2

### FUNDAMENTAL OF NONLINEAR CRASHWORTHINESS ANALYSIS

#### 2.1 Introduction

Numerical simulations of complex nonlinear transient-dynamic events such as crash analysis have greatly been enhanced with the recent advances in computer technology. In aviation and automotive industries, safety engineers and designers have heavily relied on crash simulations as the Computer Aided Engineering (CAE) tool to assist them in designing, testing and achieving certification (such as occupant seats to dynamic impact criteria in Aviation Safety). Early development of nonlinear crashworthiness dynamic finite element codes was funded by the government. From late 1960's to early 1970's, NASA and the FAA funded Grumman Corporation to develop a nonlinear static structural finite element code called Plastic Analysis of Structures (PLANS) and later the Dynamic Crash Analysis of Structures (DYCAST). About the same time, the U.S. Army funded the Lockheed California Company to develop a semi-empirical kinematic finite element aircraft crash analysis coded called KRASH. In 1970's and 1980's, a large group at Lawrence Livermore National Laboratories was funded by the U.S. Department of Energy to assemble much of the nonlinear dynamic structural and material knowledge and to develop a suite of nonlinear finite element codes including DYNA2D, DYNA3D, NIKE2D, and NIKE3D. Today, a number of commercial spinoffs including LS-DYNA, PAMCRASH,

RADIOSS, and MSC.DYTRAN are originally based on the public domain source code of the DYNA3D.

## 2.2 Explicit Formulation of Transient Dynamics

The crashworthiness analysis is among the most challenging nonlinear problems in structural mechanics. In the crash events, the structure experiences high impact loads that produce localized plastic hinges and buckling. This can ultimately lead to large deformations and rotations with contact and stacking among the various components. The deformation initially involves wave effects, associated with high stresses. Once these stresses exceed the yield strength of the material and/or its critical buckling load, localized structural deformations occur during a few wave transmits in the structure. This is followed by inertial effects, which dominate the subsequent transient response. Of particular interest are the structural integrity and associated kinematics and stacking of components, forces transmitted through the various members, stresses, strains, and energy absorption. Closed form analytical solutions of crash analysis for complex structures are formidable. The numerical technique appears to be the practical option.

The finite element (FE) method of structural dynamics solves a set of nonlinear partial differential equations of motion in the space-time domain, coupled with material stress-strain relations along with definition of appropriate initial and boundary conditions. The solution first discretizes the equations in space by formulating the problem in a weak variational form and assuming an admissible displacement field. This yields a set of second order differential equations in time. Next, the system of equations is solved by the classical Newmark-Beta method. The technique is called



implicit if the selected integration parameters render the equations coupled, and in this case the solution is unconditionally stable. If the integration parameters are selected to decouple the equations, the solution is called explicit and is conditionally stable. The following section gives the details of the FE method formulations:

### 2.2.1 Governing Equations

Consider the momentum equation in  $\Omega$  as shown in Figure 2.1:

$$\sigma_{ij,j} + \rho f_i = \rho \ddot{x}_i \quad 2.1$$

satisfying the following boundary conditions:

1. Traction boundary conditions on  $\Gamma_s$

$$\sigma_{ij} n_j = t_i \quad 2.2$$

2. Displacement boundary condition on  $\Gamma_u$

$$u_i = U_i^0(t) \quad 2.3$$

3. Contact discontinuity on  $\Gamma_c$

$$(\sigma_{ij}^+ - \sigma_{ij}^-) n_j = 0 \quad 2.4$$

where

$\sigma_{ij}$  Cauchy stress

$\rho$  Density

$f_i$  Body force

$a_i$  Acceleration

$n_j$  Unit outward normal to a boundary element

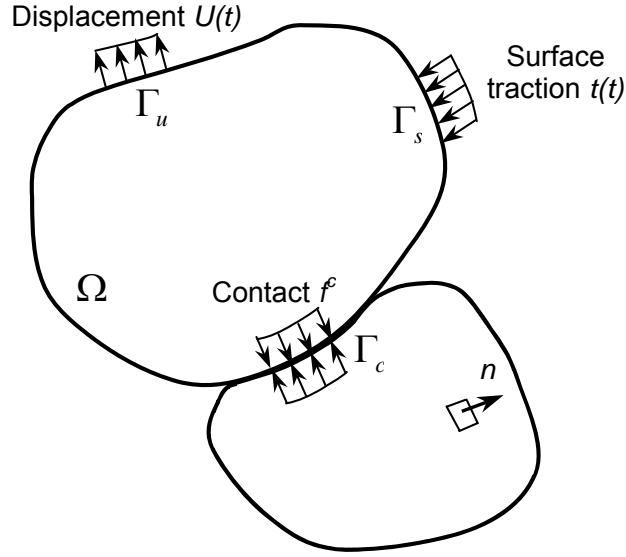


Figure 2.1 Notation for System of Equations

### 2.2.2 Variational Principle

The foregoing system of equations is too complex to integrate directly. Therefore, a weak form solution in the sense of weighted residuals (or so-called Galerkin Method) is desired and can be written as:

$$\int_{\Omega} (\rho \ddot{\mathbf{x}}_i - \sigma_{ij,j} - \rho \mathbf{f}_i) \delta \mathbf{x}_i dv + \int_{\Gamma_s} (\sigma_{ij} \mathbf{n}_j - \mathbf{t}_i) \delta \mathbf{x}_i ds + \int_{\Gamma_c} (\sigma_{ij}^+ - \sigma_{ij}^-) \mathbf{n}_j \delta \mathbf{x}_i ds = 0 \quad 2.5$$

where  $\delta \mathbf{x}_i$  is the arbitrary test functions satisfying the boundary conditions

Applying the Gauss divergence theorem gives:

$$\int_{\Omega} (\sigma_{ij} \delta \mathbf{x}_i)_{,j} dv = \int_{\Gamma_s} \sigma_{ij} \mathbf{n}_j \delta \mathbf{x}_i ds + \int_{\Gamma_c} (\sigma_{ij}^+ - \sigma_{ij}^-) \mathbf{n}_j \delta \mathbf{x}_i ds = 0 \quad 2.6$$

Note that:

$$(\sigma_{ij} \delta \mathbf{x}_i)_{,j} \sigma_{ij,j} \delta \mathbf{x}_i = \sigma_{ij} \delta \mathbf{x}_{i,j} \quad 2.7$$

Therefore Equation 2.1 leads to the weak form of the equilibrium equations as a statement of the Principle of Virtual Work as:

$$\delta\pi = \int_{\Omega} \rho \ddot{\mathbf{x}}_i \delta \mathbf{x}_i dv + \int_{\Omega} \boldsymbol{\sigma}_{ij} \delta \mathbf{x}_{i,j} dv - \int_{\Omega} \rho \mathbf{f}_i \delta \mathbf{x}_i dv - \int_{\Gamma_s} \mathbf{t}_i \delta \mathbf{x}_i ds = 0 \quad 2.8$$

### 2.2.3 Discretized Variational Principle

By superimposing a mesh of finite elements interconnected at nodal points on a reference configuration and tracking particles through time yields:

$$\mathbf{x}_i(\mathbf{X}, t) = \sum_{j=1}^k \boldsymbol{\varphi}_j(\xi, \eta, \zeta) \mathbf{x}_i^j(t) \quad 2.9$$

where  $\boldsymbol{\varphi}_j$  are the shape (interpolation) functions of the parametric coordinates  $(\xi, \eta, \zeta)$ ,  $k$  is the number of nodal points defining the element, and  $\mathbf{x}_i^j$  is the nodal coordinate of the  $j^{th}$  node in the  $i^{th}$  direction.

Summing Equation 2.8 over the  $n$  elements gives:

$$\sum_{m=1}^n \left( \int_{\Omega_m} \rho \ddot{\mathbf{x}}_i \boldsymbol{\Phi}_i^m dv + \int_{\Omega_m} \boldsymbol{\sigma}_{ij}^m \boldsymbol{\Phi}_{i,j}^m dv - \int_{\Omega_m} \rho \mathbf{f}_i \boldsymbol{\Phi}_i^m dv - \int_{\Gamma_s} \mathbf{t}_i \boldsymbol{\Phi}_i^m ds \right) = 0 \quad 2.10$$

where  $\boldsymbol{\Phi}_i^m = (\boldsymbol{\varphi}_1, \boldsymbol{\varphi}_2, \dots, \boldsymbol{\varphi}_k)_i^m$ , or in the matrix form as:

$$\sum_{m=1}^n \left( \int_{\Omega_m} \rho \mathbf{N}^T \mathbf{N} \ddot{\mathbf{x}} dv + \int_{\Omega_m} \mathbf{B}^T \boldsymbol{\sigma} dv - \int_{\Omega_m} \rho \mathbf{N}^T \mathbf{b} dv - \int_{\Gamma_s} \mathbf{N}^T \mathbf{t} ds \right)^m = 0 \quad 2.11$$

where  $\mathbf{N}$  is the shape function matrix,  $\boldsymbol{\sigma}$  is the stress vector,  $\mathbf{B}$  is the strain-displacement matrix,  $\ddot{\mathbf{x}}$  is the nodal acceleration vector,  $\mathbf{b}$  is the body force load vector, and  $\mathbf{t}$  is the applied traction loads.

### 2.3 Explicit Time Marching Integration

The explicit FE technique solves a set of hyperbolic wave equations in the zone of influence of the wave front, and accordingly does not require coupling of large number of equations. On the other hand, the unconditionally stable implicit solves provides a solution for all coupled equation of motion, which require assembly of a global stiffness matrix. The time step for implicit solvers is about two to three orders of magnitude of the explicit time step, as shown in Figure 2.2. Table 2.1 compares the differences between explicit and implicit techniques. For crash simulations involving extensive use of contact, multiple material models and a combination of non-traditional elements, it turned out that explicit solvers are more robust and computationally more efficient than implicit solvers. The FE simulation for structural crashworthiness by explicit solvers appears to be first introduced by Belytschko.

Table 2.1 Comparison of Explicit and Implicit Integration Techniques

	<b>Explicit</b>	<b>Implicit</b>
Matrix	No matrix assembly and matrix inversion is not required	Require matrix assembly and inversion
Time step	Small time step (conditional stable)	Large time step (unconditional stable)
Implementation	Easy and robust solution procedure even for high degree of nonlinearities	Solution procedure becomes complicated with increasing degree of nonlinearities

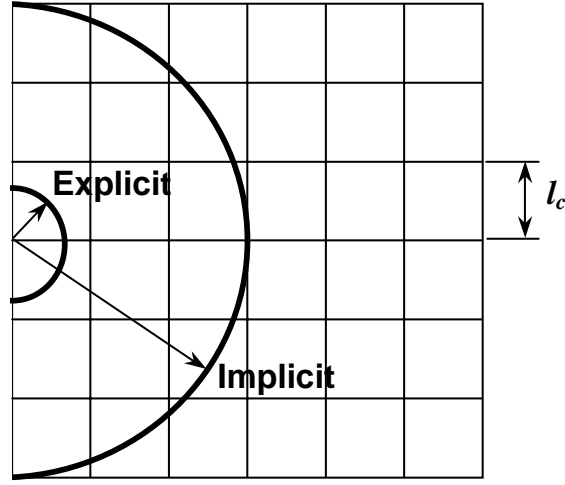


Figure 2.2 Critical Time Step Comparison for Explicit and Implicit Techniques in Nonlinear Finite Element Analysis

The semi-discretized (i.e. discretized in space domain but continuous in time domain) momentum equations of Equation 2.11 in Lagrangian mesh can be written as:

$$\mathbf{M}\ddot{\mathbf{x}} = \mathbf{f}^{ext} - \mathbf{f}^{int} \quad .12$$

where  $\mathbf{M}$  is the inertia matrix of the structure,  $\mathbf{f}^{ext}$  is the external nodal force vector and  $\mathbf{f}^{int}$  is the internal nodal force vector.

The central difference technique is employed in the explicit time integration. The explicit time marching scheme is depicted in Figure 2.3.

$$\ddot{\mathbf{x}}^{(n)} = \mathbf{M}^{-1} \left( \mathbf{f}^{ext(n)} - \mathbf{f}^{int(n)} \right) \quad 2.13$$

$$\dot{\mathbf{x}}^{(n+1)/2} = \dot{\mathbf{x}}^{(n-1)/2} + \ddot{\mathbf{x}}^{(n)} \Delta t^{(n)} \quad 2.14$$

$$\mathbf{x}^{(n+1)} = \mathbf{x}^{(n)} + \dot{\mathbf{x}}^{(n+1)/2} \Delta t^{(n+1)/2} \quad 2.15$$

$$\Delta t^{(n+1)/2} = \frac{\Delta t^{(n)} + \Delta t^{(n+1)}}{2} \quad 2.16$$

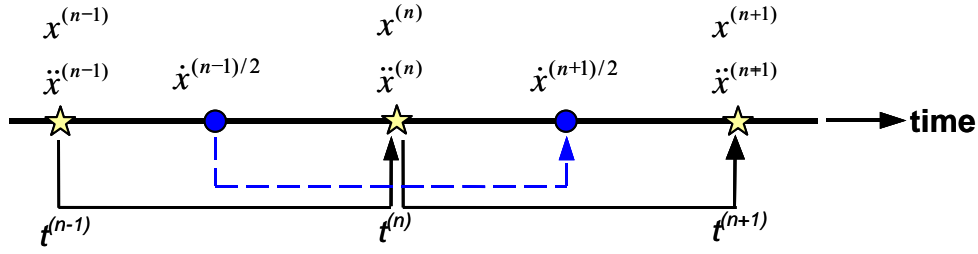


Figure 2.3 Schematic of Explicit Time Marching Integration

The drawbacks of the explicit algorithm are the conditional stability and inability of treating static problems. The conditional stability means that the integration time step must be smaller or equal to the Courant Criterion. The Courant Criterion is based on the minimum time required for an acoustic stress wave to propagate across an element. For beam and truss elements, smallest time step is:

$$\Delta t = S \frac{l_c}{c} = S l_c \sqrt{\frac{\rho}{E}} \quad 2.17$$

where  $S$  is the time step scale factor,  $l_c$  is the element characteristic length,  $c$  is the sound speed,  $\rho$  is the density and  $E$  is the Young's Modulus.

A shell element can be interpreted as a series of beam elements located next to each other. The geometry confines the Poisson's ratio effects in the plane of the shell during the longitudinal compression and therefore increases the longitudinal stiffness as well as the wave speed. Therefore, the critical time step for shell elements with an elastic material and constant bulk modulus becomes:

$$\Delta t = \alpha S l_c \sqrt{\frac{\rho}{E}} \quad 2.18$$

where

$$\alpha = \sqrt{1 - \nu^2} \quad 2.19$$

For solid elements, the Poisson's ratio effects can be interpreted to confine in both transverse directions during the longitudinal compression. Consequently, the membrane stiffness and the acoustic wave speed increase significantly. For an elastic material with constant bulk modulus, the critical time step of solid elements is:

$$\Delta t = \beta S l_c \sqrt{\frac{\rho}{E}} \quad 2.20$$

where

$$\beta = \sqrt{\frac{(1+\nu)(1-2\nu)}{(1-\nu)}} \quad 2.21$$

Table 2.2 and Figure 2.4 show the critical time step factor of shell and solid elements compared to beam elements. Note that when the material is incompressible (i.e.  $\nu=0.5$  or  $\beta=0$ ), the critical time step is zero.

Table 2.2 Critical Time Step Factors for Shell and Solid Elements

$\nu$	0.0	0.20	0.30	0.40	0.45	0.49	0.50
$\alpha$	1.0	0.980	0.954	0.917	0.893	0.872	0.866
$\beta$	1.0	0.949	0.862	0.683	0.513	0.242	0.000

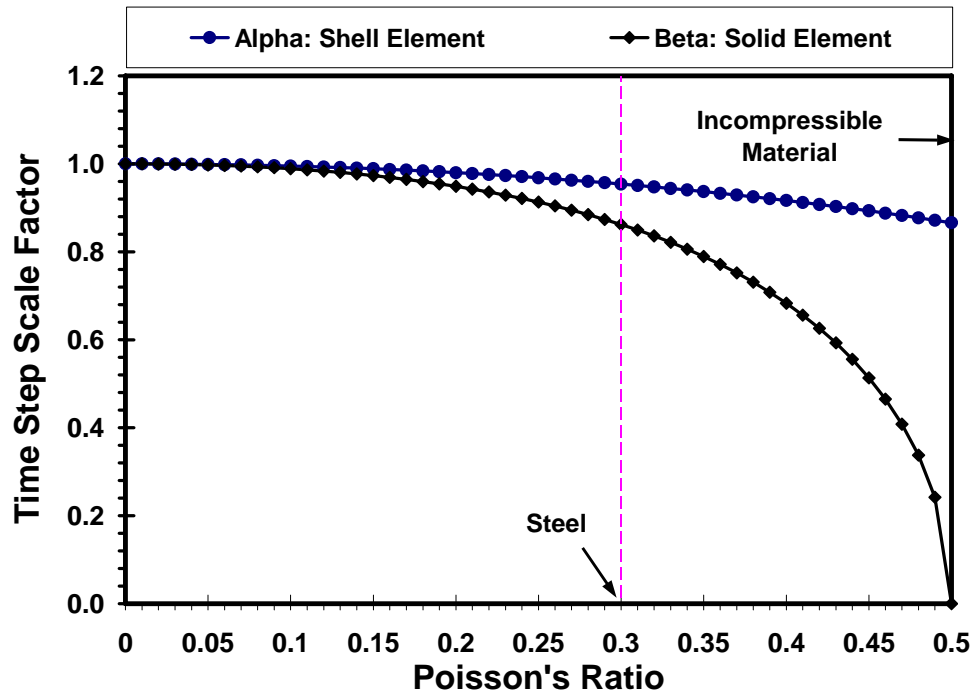


Figure 2.4 Critical Time Step Factors for Shell and Solid Elements

#### 2.4 Elements for Crashworthiness Analysis

The 4-noded Belytschko-Tsay shell element [12] is discussed in this section since it has widely been used for crashworthiness simulations due to its computational efficiency and numerical robustness by the manufacturing industry, particularly the automotive and aerospace industries. The Belytschko-Tsay shell element is based on a combined co-rotational and velocity-strain formulation. The efficiency of the element is obtained from the mathematical simplifications that result from these two kinematic assumptions. The co-rotational portion of the formulation avoids the complexities of nonlinear mechanics by embedding a coordinate system in the element. The choice of



velocity strain, or rate of deformation, in the formulation facilitates the constitutive evaluation, since the conjugate stress is the more familiar Cauchy stress.

The Belytschko-Tsay is a bilinearly interpolated isoparametric element. The use of under-integrated points makes it very efficient in terms of computational cost. The drawback of using under-integration, however, is that a number of zero-energy or so-called hourglass energy modes may exist in the element. Due to the simplifications of evaluating the element strain-displacement matrix, certain deformation modes result in a zero-strain calculation, and consequently, no stresses and nodal forces are evaluated. Most crash codes implemented hourglass control algorithms to prevent the non-physical hourglass modes from occurring. However, if too much hourglass energy is required to suppress the phenomenon, the crash solution becomes invalid.

In spite of a number of choices that clearly include a loss of generality and trade-off for numerical robustness and computational efficiency, the results obtained in thousands of crashworthiness simulations using the Belytschko-Tsay element during the past two decades have been good enough to establish its usefulness to the industry.

## 2.5 Contact-Impact Algorithm

The most common used contact for crashworthiness applications is the penalty-based method. There are two penalty-based methods of calculating the contact force. In the first method, the contact force on a node is based on a penetration distance times the material stiffness. In the second method, the contact force is proportional to the penetration distance divided by the time-step squared multiplied by an effective mass. Figures 2.5 (a) and (b) show two frequent used contacts based on the penalty-based method: surface-to-surface contact and self-surface contact, respectively.

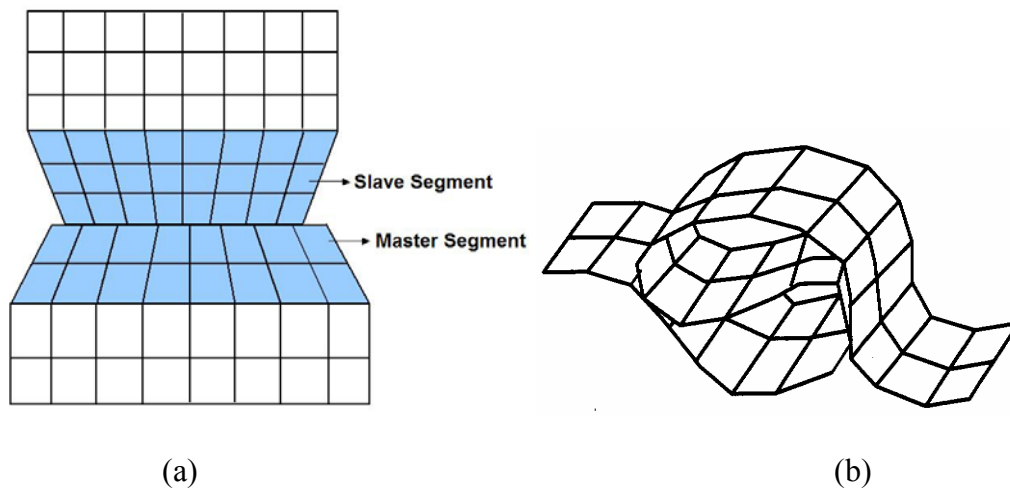


Figure 2.5 Schematic of Surface-to-Surface and Self-Surface Contact Algorithms: (a) Surface-to-Surface Contact, (b) Self-Surface Contact

## 2.6 Crashworthiness in Aerospace Industry

First used in the aerospace industry in the early 1950's, the term “crashworthiness” provided a measure of the ability of a structure and any of its components to protect the occupants in survivable crashes. Crashworthiness of general aviation aircraft is a complex subject involving human tolerance, the crash environment (impact surface, terrain, aircraft velocities and attitudes), seats and restraint systems,

cabin environment, landing gear, and the airframe structure. Figure 2.6 depicts the crash energy absorption approaches for various types of aircraft (transport, light fixed-wing, and helicopter). Various types of aircraft may affect the crashworthiness design approach. For example, to provide control of deceleration loads of seated occupants in a vertical impact, a different design approach would probably be used for a large transport aircraft compared to a light fixed-wing general aviation aircraft or a helicopter. The large transport structure having considerable depth of crushable structure may not require energy-absorbing landing gear and seats. On the other hand, light fixed-wing aircraft and helicopters having relatively little crushable airframe structure would require energy absorption in the landing gear and seats, as well as the fuselage structure, to prevent injury to occupants in potentially survivable crashes.

When designing a crashworthy airframe structure, there are many factors to consider. Of prime importance is the design of the airframe to maintain structural integrity and a livable space for the occupants. The airframe structure should incorporate a high-strength protective shell or cage around the occupants. This structure should provide roll-over strength, a strong support structure for restraint of large mass items and seats, as well as maintain the integrity of the normal exits for emergency egress. The forward fuselage structure should be designed to minimize plowing and to absorb energy during longitudinal impacts. In addition, the crushable structure in an aircraft should be designed to carry normal airframe loads as well as absorb as much energy as possible in a crash. If the seat support structure is allowed to crush, it must maintain enough structural capability to support the seat loads. If the

seats are energy absorbing, the crushing structure must not interface with the stroking seats. Figures 2.7 (a) to (c) show several crashworthiness applications in the aerospace industry including the hard surface impact of the ATR42 commuter aircraft, hard surface impact of the helicopter composite fuselage, and water impact of the rotorcraft.

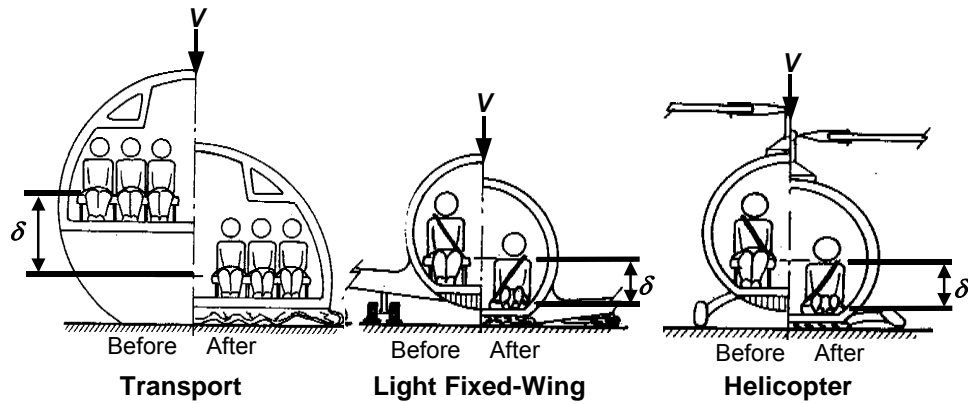


Figure 2.6 Crash Energy Absorption Approaches for Various Types of Aircraft

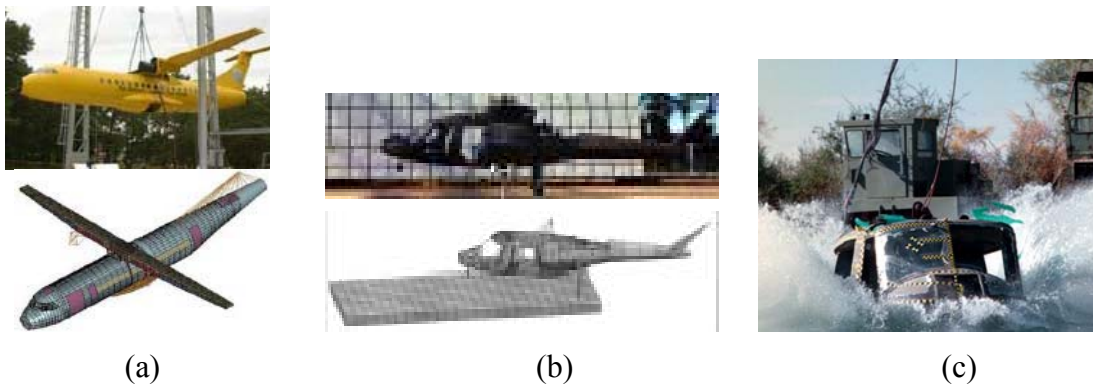


Figure 2.7 Crashworthiness Applications in Aerospace Industry: (a) ATR42 Commuter, (b) Helicopter Composite Fuselage, (c) Rotorcraft Water Impact

## 2.7 Crashworthiness in Automotive Industry

In the automotive industry, crashworthiness connotes a measure of the vehicle's structural ability to plastically deform and yet maintain a sufficient survival space for its

occupants in crashes involving reasonable deceleration loads. Restraint systems and occupant packaging can provide additional protection to reduce severe injuries and fatalities. The goal of crashworthiness is an optimized vehicle structure that can absorb the crash energy by controlling vehicle deformations while maintaining adequate space so that the residual crash energy can be managed by the restraint systems to minimize crash loads transfer to the vehicle occupants.

For crashworthiness requirements, the vehicle structure should be sufficiently stiff in bending and torsion for proper ride and handling. It should minimize high fore-aft vibrations that give rise to harshness. In addition, the structure should yield a deceleration pulse that satisfies the following requirements:

- Deformable, yet stiff, front structure with crumple zone to absorb the crash kinetic energy resulting from frontal collisions by plastic deformation and prevent intrusion into the occupant compartment.
- Deformable rear structure to maintain integrity of the rear passenger compartment and protect the fuel tank.
- Properly designed side structures and doors to minimize intrusion in side impact and prevent doors from opening due to crash loads.
- Strong roof structure for rollover protection.
- Properly designed restraint systems that work in harmony with the vehicle structure.

Figure 2.8 shows some crashworthiness applications in the automotive industry including the frontal offset impact, side impact, and occupant restraint system.

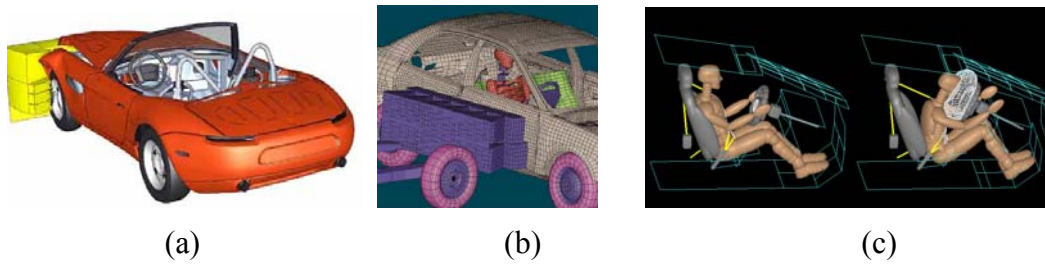


Figure 2.8 Crashworthiness Applications in Automotive Industry: (a) Frontal Offset Impact, (b) Side Impact, (c) Occupant Restraint System

### 2.8 Column Collapse Modes Under Crush Loadings

In the energy absorption management, there are two basic collapse modes or mechanisms encountered for thin-walled structural columns: axial collapse mode and bending collapse mode. Pure axial collapse can be achieved only in the energy-absorbing structures and only during direct frontal/rear impacts. Therefore, most of the structural members are subject to mixed modes comprised of axial collapse and bending. In a well-designed and executed energy-absorbing structure, the mixed modes can be avoided to assure predictable performance during crash. The sheet metal closure/shear and outer skin panels are likely to collapse by predominantly irregular folding or crumpling. The degree of folding regularity depends on the panel's size-to-thickness ratio and geometric stiffness (or curvature).

#### *2.8.1 Axial Collapse Mode*

Axial folding crush mode is considered to be the most effective mechanism for energy absorption. It is also, perhaps, the most difficult one to achieve in real structures because of the instability problems associate with it. Figure 2.9 shows a typical stable axial collapse mode of a square column under axial crush loading.

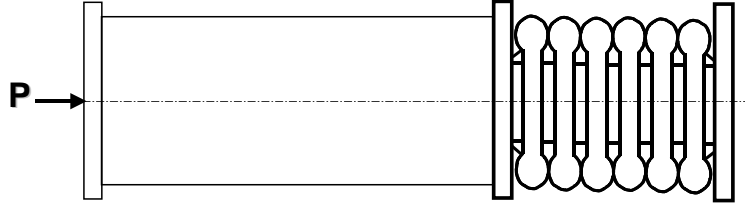


Figure 2.9 Axial Collapse Mode of Column under Axial Crush Loading

Wierzbicki and Abramowicz [91] developed a theory of crushing behavior of thin-walled, plate-type columns. The expression for the mean crush load is derived from the energy balance by equating the external work done by the crush load with energies dissipated in different types of deformation mechanisms as they occur in a folding process. Based upon this, the mean crush load  $P_m$  can be expressed as:

$$P_m = 38.27 M_0 C^{1/3} t^{-1/3} \quad 2.22$$

$$M_0 = \frac{\sigma_0 t^2}{4} \quad 2.23$$

$$\sigma_0 = (0.9 \sim 0.95) \sigma_u \quad 2.24$$

$$C = \frac{1}{2}(b + d) \quad 2.25$$

where  $M_0$  is the fully plastic moment,  $\sigma_0$  is the average flow stress,  $\sigma_u$  is the ultimate tensile strength of the material,  $b$  and  $d$  are the width and height of a rectangular box column, and  $t$  is the wall thickness. For a square tube, for which  $C = d = b$ , the mean crush load of the previous equation can be simplified to:

$$P_m = 9.56 \sigma_0 t^{5/3} b^{1/3} \quad 2.26$$

Magee and Thornton [58] employed experimental data from crush tests of columns of several different section geometries to derive the mean crush load  $P_m$  for square thin-walled columns:

$$P_m = 17\sigma_u t^{1/8} b^{0.2} \quad 2.27$$

However, none of the formulations given by Equations 2.1 and 2.6 consider the material elasticity. Mahmood and Paluszny [56] realized the shortcoming and developed a quasi-analytical approach to derive  $P_m$  for square thin-walled columns:

$$P_m = 3270\beta^{-0.43}\sigma_y^{0.57}t^{1.86}b^{0.14} \quad 2.28$$

where  $\beta$  is the material strain hardening factor, and  $\sigma_y$  is the material yield strength.

### 2.8.2 Bending Collapse Mode

The bending mode, which involves formation of local hinge mechanisms and linkage-type kinematics, is a lower energy mode. Figure 2.10 shows a typical bending collapse mode of a thin-walled structural component under moment crush loading. Pure bending failures are extremely rare in vehicle structures. In most crash scenarios, mixed modes involving axial compression and bending or sometimes torsion, will prevail. In these situations, component failure will be triggered at the location where compressive stress reaches the critical value, causing the side of flange of the section to buckle locally, which initiates formation of a plastic hinge-type mechanism.

There are three different types of collapse modes observed in box-type columns subjected to bending. The first mode is associated with the collapse of a compressively loaded flange of a compact section that is identified by a uniform hinge mechanism



composed of straight yield lines. The second mode is initiated by the flange collapse of non-compact sections, identified by non-uniform hinge mechanisms composed of curved yield lines. The third mode is initiated by the web collapse of narrow of stiffened flange columns.

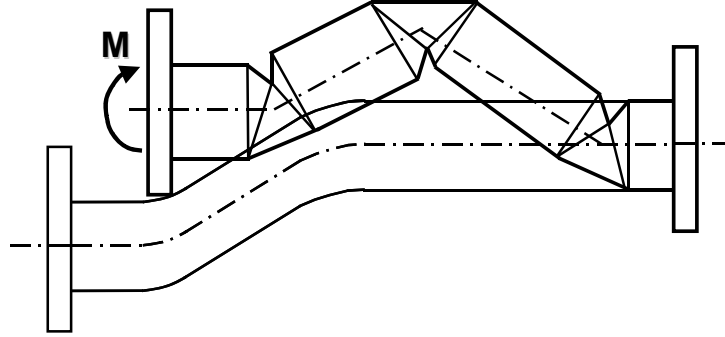


Figure 2.10 Bending Collapse Mode of Column under Moment-Crush Loading

Kocman [48] postulated that the bending collapse is initiated by local buckling of the compressively loaded flange and used the concept of “effective flange width” to develop expressions for the maximum bending strength capacity of a rectangular box section. If the critical local buckling stress  $\sigma_{cr}$  is less than the material yield stress  $\sigma_y$ , the compressively loaded flange will buckle elastically, producing a non-linear stress distribution with the middle portion carrying considerably less load than the corners. Thus, in terms of the corner stress, the effective width of the flange has been reduced:

$$d_e = d \left( 0.7 \frac{\sigma_{cr}}{\sigma_y} + 0.3 \right) \quad 2.25$$

The critical local buckling stress is given by:

$$\sigma_{cr} = \frac{K_f \pi^2 E (t/d)^2}{12(1-\nu^2)} \quad 2.26$$

$$K_f \approx 5.23 + 0.16 \frac{d}{b} \quad 2.27$$

where  $K_f$  is the flange buckling coefficient,  $b$  and  $d$  are the sides of the section.

Different formulations are used for the maximum moment depending on the magnitude of the critical local buckling stress relative to the material yield strength:

$$M_{\max} = \begin{cases} M_p^t + (M_p - M_p^t) \left( \frac{\sigma_{cr} - \sigma_y}{\sigma_y} \right) & \text{if } \sigma_{cr} > \sigma_y \\ M_p & \text{if } \sigma_{cr} \leq \sigma_y \end{cases} \quad 2.28$$

$$M_{\max}^t = \frac{\sigma_y t b [2d + b + d_e (3a/b + 2)]}{3(d + b)} \quad 2.29$$

$$M_p^t = \sigma_y t b (d + b/3) \quad 2.30$$

$$M_p = \sigma_y t \left[ d(b - t) + \frac{(b - 2t)^2}{2} \right] \quad 2.31$$

## 2.9 Dynamic Effect on the Crash Resistance

A dynamic collapsing process in the thin-walled structures involves many interacting effects that are not present in the static collapse. There are two most important factors identified in dynamic collapse under the impact velocity in the most of crash accidents where the strain rates are below  $100 \text{ sec}^{-1}$ . The first is the strain effect, which is a material property, whereby the yield or flow stress is raised. The second factor is the inertia effect developed within the structure by the rapid acceleration during the collapse.

While the inertia effects were shown to be responsible for peak magnitudes of the instantaneous resisting forces and therefore do not contribute the crash energy dissipation, many studies have been conducted on the strain rate empirically or analytically yielding simple equations relating the dynamic crash resistance and the static crush resistance. Ohkubo *et al* [67] suggested an empirical formula for dynamic load factor in closed-hat axially compressed columns. By fitting experimental data, a ratio of dynamic to static crushing force was approximated linearly:

$$\frac{P_d}{P_s} = 1 + 0.0668V_0 \quad 2.32$$

where  $P_d$  is the dynamic crash force,  $P_s$  is the static crushing force, and  $V_0$  is the initial impact velocity. A different empirical formula was obtained by Wimmer for square mild steel columns:

$$\frac{P_d}{P_s} = 1 + 0.07V_0^{0.82} \quad 2.33$$

The Cowper-Symonds equation [20] has widely been used to relate the dynamic flow stress  $\sigma_0^d$  to the static flow stress  $\sigma_0^s$ :

$$\frac{\sigma_0^d}{\sigma_0^s} = 1 + \left( \frac{\dot{\epsilon}}{C} \right)^{1/p} \quad 2.34$$

where  $\dot{\epsilon}$  is the strain rate,  $C$  and  $p$  are material constants to be determined from the dynamic tensile tests on the material.

Based on the strain rate sensitivity on the yield stress of material, Masanori and Funahashi [57] derived the following equation for mild steel structure by simply applying the Cowper-Symonds equation with one-dimensional uniform deformation assumption:

$$\frac{P_d}{P_s} = 1 + \left( \frac{V_0}{2.475 \times 10^{-4} L} \right)^{0.2} \quad 2.35$$

where  $L$  is the crushing distance.

Wierzbicki and Akerstrom [91] derived the following equation with the consideration of complex folding mechanism of axially compressed mild steel box column:

$$\frac{P_d}{P_s} = 1 + 0.11 V_0^{0.714} \quad 2.36$$

For impact velocities used in crash barrier tests, the dynamic correction factor is in the range of  $P_d/P_s = 1.2 \sim 1.4$  [46]. This of course applies to utilized steel body structures. Aluminum alloy have no or very little strain rate sensitivity. All general

application purposes, no dynamic correction factor needs to be introduced in all aluminum vehicle bodies. Wierzbicki [91] observed from the comparison of static and dynamic tests of crushing of thin-walled structures that the deformation patterns of sheet metal components differ little between static and dynamic loading conditions.

## CHAPTER 3

### CRASHWORTHINESS OPTIMIZATION USING DESIGN OF EXPERIMENTS AND RESPONSE SURFACE METHODOLOGY

#### 3.1 Introduction

Today, manufacturing industry, particularly automotive industry, still relies intensively on Computer Aided Engineering (CAE) for crashworthiness design to reduce the design cycle time and development cost in the early design stage, while satisfying different design functionality requirements and disciplines. Numerical optimization technique, on the other hand, provides a systematic approach to achieve the objective within competitive time constraint. However, numerical crashworthiness optimization faces a lot of technical challenges. The traditional gradient-based direct optimization technique requires many function evaluations and hence is prohibitive since the computation of crash analysis for large-scale systems is very costly due to the very small time step requirement in the explicit nonlinear finite element method. The crash pulse functions in the crashworthiness analysis are very noisy and irregular due to impact-contact algorithms in the explicit nonlinear dynamic finite element method. The sensitivity of the crash pulse with respect to the design parameters depends on the finite element mesh and the finite difference step size. The bottom line is that numerically computed design sensitivities are prone to error and therefore it is extremely difficult to

obtain accurate sensitivities for routine use in the gradient-based direct optimization technique.

Alternatively, many researchers have achieved prominence by using the surrogate-model based optimization that combines the Design of Experiments (DOE) and Response Surface Methodology (RSM) to explore the design space and construct approximate crash functions for solving crashworthiness design optimization problems in recent years. RSM based optimization refers to the idea of speeding optimization processes by using the surrogate models for the objective and constraint functions. RSM is a statistical method for constructing smooth approximations to functions in a multi-dimensional space. Thus the local effect caused by the ‘noisy’ functions is alleviated and the method attempts to find a representation of the design response within a bounded design space. Based on the extraction of global information of these “efficient-to-compute” surrogate models (or so-called metamodels), designer can access the main effect and perform approximate optimization, multi-criteria trade-off analysis, robustness assessment, as well as robust design using alternative design formulations. The quality of RSM is extremely crucial in those stages as poor RSM will be misleading, causing the optimization solution diverged and increasing the design cycle time.

Typically the surrogate model based optimization method involves the following procedures:

1. Choose an experimental design to sample the region of interest (of design space);
2. Perform analyses (or simulations) based upon the selected sample data;

3. Construct the surrogate model (or RSM, meta-model) to the observed sample data;
4. Perform approximate optimization to find the predicted optimal design;
5. Validate the predicted optimal design by conducting an analysis on the fine model (or true function);
6. Check for convergence (stop if within convergence tolerance);
7. Update surrogate model using new data points;
8. Iterate until convergence.

Figure 3.1 illustrates the procedures for Steps 1 to 3. The motivation of the method is to take advantage of the effectiveness of search algorithms used in the numerical optimization more efficiently using DOE generated data to construct surrogate models in an approximate optimization algorithm.

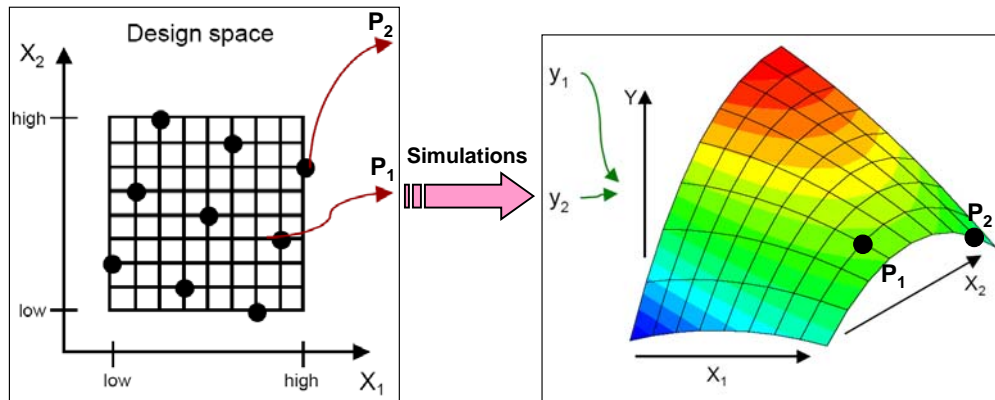


Figure 3.1 Schematic of Design of Experiments and Response Surface Methodology Based Computer Simulations

Over the years, there have seen several researchers conducted the comparative study of the surrogate models. Wang and Liu (1998) [90] employed linear regression model, piecewise linear regression model, quadratic regression model and multivariate



adaptive regression splines (MARS) to construct surrogate models for a body-in-white vehicle model containing five design parameters. They found that the accuracy of the approximation is decided by the choice of regression model and the number of data points used. When very little information is available, the result is almost the same no matter which model to use. When a large number of evaluations are available ( $> 5N$ ), using a more complex regression model can generate a better approximation.

Jin *et al.* (2000) [40] compared four popular metamodeling techniques (polynomial regression, multivariate adaptive regression splines, radial basis functions and kriging) based on multiple performance criteria using fourteen test problems representing different classes of problems. They concluded that for small and scarce sample sets, radial basis function performs the best when both average accuracy and robustness are considered. Kriging appears to be a more expensive metamodeling technique in terms of efficiency while polynomial and radial basis function are the easiest to implement in terms of simplicity. It is very important to obtain uniform samples to improve metamodeling performance.

Krishnamurthy (2005) [51] compared surrogate models constructed the moving least square, kriging, and radial basis function with the global least square method for three numerical examples for derivative generation capability. He found that the surrogate models constructed by kriging and radial basis function interpolation yields more accurate results compared to the moving least square and global least square methods.

Fang et al (2005) [51] compared the polynomial regression and kriging methods in multi-objective crashworthiness optimization of a full-scale vehicle model. The study showed that the Multiquadric function is the more stable compared to the first- and second-order of polynomial, as well as other radial basis functions (such as inverse Multiquadric).

### 3.2 Design of Experiments

Design of experiments (DOE) offers a systematic approach to study the effects of multiple design parameters by providing a structured set of analyses in a design matrix. Specifically, DOE techniques allow designers to sample the design space to generate sample data to create surrogate models for each of the responses of interest. It can be used for screening experiments to identify significant factors and reduce the number of interested design parameters. Among some of the popular DOE methods are central composite design, D/G-Optimal designs, Box-Behnken design, and orthogonal arrays. Among these, the orthogonal arrays (OA) appear to be more attractive it allows to avoid a costly full factorial experiment, in which all combinations of all factors at different levels are studied. Namely, a fractional factorial experiment can be performed by executing a certain fractional subset of the full factorial set of experiments while maintaining orthogonality among the various factors and specified interactions. Orthogonal arrays were formulated as early as the late 1800's by Hadamard and have been used in design since as early as the 1940's by Plackett and Burman, who formulated saturated designs which now referred to as Plackett-Burman designs. Orthogonal arrays were primarily popularized by Taguchi, who developed a

standardized family of OAs to study interaction effects and focused on improving design quality by reducing variation from the target.

Properly selection of experimental designs is essential for design and analysis of computer experiments. In the classical design and analysis of physical experiments (e.g. central composite, full factor design etc.), random variation is accounted by spreading the sample points out in the design space and by taking multiple data points (replicates). Sacks *et al.* (1989) stat that the classical notions of experimental blocking, replication, and randomization are irrelevant when it comes to deterministic computer experiments. Thus, sample points should be chosen to fill the design space uniformly for computer experiments. In this dissertation, several “space filling” experimental designs are reviewed.

### 3.2.1 Latin Hypercube Sampling

Latin hypercube sampling (LHS) was the first type of design proposed specifically for computer experiments by Mckay *et al.* (1979) [60]. LHS is a form of simultaneous stratification on all  $d$  dimensions. It offers flexible sample sizes while ensuring stratified sampling, i.e. each of the input variables is sampled at  $n$  levels. Mckay (1979) introduced a version of LHS for computer experiments:

$$X_i^j = \frac{\pi_j(i) - U_i^j}{n} \quad 3.1$$

where  $\pi_j$  are uniform random permutations of the integer  $1, \dots, n$ , the  $U_i^j$  are  $U[0,1]$  random variables. All of the  $\pi_j$  and  $U_i^j$  are independent.

An older version of LHS, due to Patterson (1954) [68] is

$$X_i^j = \frac{\pi_j(i) - 0.5}{n} \quad 3.2$$

### 3.2.2 Uniform Design

A uniform design (UD) provides uniformly scatter design points in the experimental domain. A uniform design is a type of fractional factorial design with an added uniformity property. If the experimental domain is finite, UD is very similar to LHS. When the experimental domain is continuous, the fundamental difference between these two designs is that in LHS, the sampling points are selected at random from cells, whereas in a UD, the sampling points are selected from the center of the cells. Furthermore, LHS requires one-dimensional balance of all levels for each factor, while UD requires one-dimensional balance and n-dimensional uniformity. Therefore these two designs are similar in one-dimension but are very different in higher dimensions.

### 3.2.3 Halton Sequence

Halton Sequence (Halton, 1960) [36] is used to generate a “uniform design” of the sampling points. Let the base  $b \geq 2$  be an integer, any positive integer  $n \geq 0$  can be written as the following form:

$$(n)_b = (d_j \cdots d_2 d_1 d_0)_b \quad 3.3$$

or

$$\phi_b(n) = \sum_{k=0}^j d_k b^k \quad 3.4$$

The radical inverse function  $\phi_b(n)$  for base  $b$  can be obtained by reversing the digits in  $(n)_b$  using the Van der Corput sequence (Niederreiter, 1992) [66] and the  $n^{\text{th}}$  Halton number in base  $b$  is:

$$\phi_b(n) = \frac{d_0}{b} + \frac{d_1}{b^2} + \cdots + \frac{d_j}{b^{j+1}} = (0.d_0d_1d_2 \cdots d_j)_b \quad 3.5$$

or

$$\phi_b(n) = \sum_{k=0}^j d_k b^{-(k+1)} \quad 3.6$$

Thus, Halton sequence in  $s$ -dimensional can be expressed as:

$$X_n = \{\phi_{b_1}(n), \phi_{b_2}(n), \phi_{b_s}(n)\} \quad 3.7$$

Note that  $b$  must be a prime number. The above algorithms generate numbers from 0 to 1. For high dimensions, different prime numbers are used for each dimension. The points generated by Halton Sequence fills the  $(0, 1)$  hypercube “uniformly”.

As an example to illustrate the algorithm, we expand  $n = 38_{10}$  using base  $b = 5$ :

$$n = 38_{10} = 123_5 = 1 \times 5^2 + 2 \times 5^1 + 3 \times 5^0$$

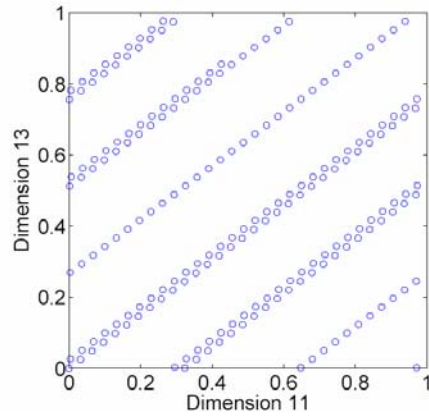
Applying the radical inverse function gives:

$$\phi_5(38_{10}) = 0.321_5 = \frac{3}{5} + \frac{2}{5^2} + \frac{1}{5^3} = 0.688_{10}$$

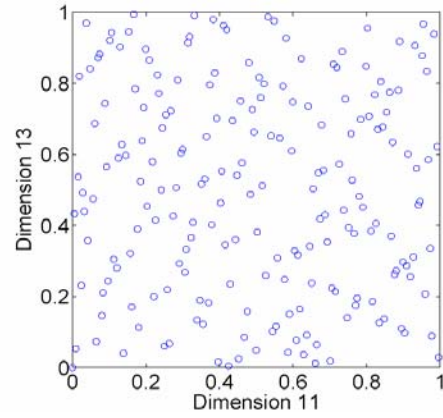
Table 3.1 shows the illustrative sampling generated by using the Halton Sequence.

Table 3.1 An Illustrative Sampling Example Using Halton Sequence

	$b=2$	$b=3$	$b=5$	...
$n=0$	0	0	0	...
$n=1$	0.5000	0.3333	0.2000	...
$n=2$	0.2500	0.6667	0.4000	...
$n=3$	0.7500	0.1111	0.6000	...
...	...	...	...	...



(a)



(b)

Figure 3.2 An Illustrative Sampling Example Using Scrambled Halton Sequence: (a) Before Scrambling, (b) After Scrambling

It is noted that the sampling generated by the Halton sequence using the radical inverse function may degrade in the higher dimension as shown in Figure 3.2(a), which is constructed using 200 Halton sampling points. A solution to resolve the issues is to employ the scrambled Halton Sequence. Figure 3.2(b) shows the projections after

scrambling. In the scramble Halton Sequence, the scrambled radical inverse function is employed in lieu of the radical inverse function as shown in Equation 3.5. Namely,

$$S_b(n) = \frac{\pi_b(d_0)}{b} + \frac{\pi_b(d_1)}{b^2} + \dots + \frac{\pi_b(d_j)}{b^{j+1}} \quad 3.8$$

where  $\pi_b$  is a permutation on the digits  $(0, 1, \dots, b-1)$  which holds 0 fixed.

To illustrate the algorithm, the scrambled radical inverse function is employed to expand the same integer using the same base as shown previously (i.e.  $n = 38_{10}$  using base  $b = 5$ ) to obtain:

$$\begin{aligned} S_5(38) &= \frac{\pi_5(3)}{5} + \frac{\pi_5(2)}{5^2} + \frac{\pi_5(1)}{5^3} \\ &= \frac{4}{5} + \frac{1}{5^2} + \frac{3}{5^3} = 0.413_5 = 0.864_{10} \end{aligned}$$

Many researchers have also proposed the scrambled version of the Halton Sequence (Warnock, 1972; Braaten and Weller, 1979; Faure, 1992; Warnock PhiCf, 1995; Tuffin, 1996; Mascagni and Chi, 2004; Atanassov, 2004).

#### 3.2.4 Sobol Sequence

The Sobol sequence (Sobol, 1967) [81] solved the problem of dependency in higher dimensions using only the prime 2. The Sobol sequence is generated using a set of so-called direction numbers  $v_k = \frac{m_k}{2^k}$ , where  $m_k$  are odd positive integers less than  $2^k$ . The values of  $m_k$  are chosen to satisfy a recurrence relation using the coefficient of a primitive in the Galois Field of order 2. A primitive polynomial is irreducible (i.e.

cannot be factored into polynomials of smaller degree) and does not divide the polynomial  $x^r + 1$  for  $r < 2^p - 1$ . Thus, the Sobol sequence can be expressed as:

$$\phi_b(n) = \sum_{k=0}^j d_k \nu_k b^{-(k+1)} \quad 3.9$$

Several authors have concluded that the Sobol sequence appears to resist the degradation effect better than the Halton sequence in higher dimensions. Galanti and Jung (1997) [32] showed that the Sobol sequence presented no degradation at all up to the dimension 260. Morokoff and Caflisch (1995) [62] concluded that for lower dimensions ( $n=6$  or lower) the Halton sequence exhibited the best results, whereas for higher dimensions the Sobol sequence were better off

### 3.2.5 Faure Sequence

The Faure sequence (Faure, 1992) [27] is similar to the Halton sequence in that each dimension is a permutation of a van der Corput sequence. As mentioned earlier in

Halton sequence, the Van der Corput sequence is mapped from  $\phi_b(n) = \sum_{k=0}^j d_k b^k$  into

$\phi_b(n) = \sum_{k=0}^j d_k b^{-(k+1)}$ . In Faure sequence, different permutation coefficients are used:

$$\phi_b(n) = \sum_{k=0}^j c_k b^{-(k+1)} \quad 3.10$$

where

$$c_k = \sum_{m=k}^j \binom{m}{k} (i-1)^{m-k} d_m \text{ mod } b \quad 3.11$$



Notice that only the last  $t - k + 1$  values of  $d_k$  are used to generate  $c_k$ . The Faure sequence has better regularity properties than the Halton sequence particularly in high dimensions. For example, consider the case  $n = 2$  and  $b = 2$ . The first 10 Faure numbers are:

$$\begin{array}{cccccccccc} 0 & 1/2 & 1/4 & 3/4 & 1/8 & 5/8 & 3/8 & 7/8 & 1/16 & 9/16 \\ 0 & 1/2 & 3/4 & 1/4 & 5/8 & 1/8 & 3/8 & 7/8 & 15/16 & 7/16 \end{array}$$

The first row corresponds to the Van der Corput numbers and the second row obtained from the first row by permuting the values with the same denominator.

Cheng and Druzdzel (2000) tested Halton, Sobol and Faure sequences concluding that for higher dimensions the Sobol sequences outperformed the other two.

### 3.3 Surrogate Models

#### *3.3.1 Polynomial Regression*

By far, the polynomial regression perhaps is the most popular technique for building the response surface or surrogate model (Myers and Montgomery, 1995) [64]. For complex engineering systems such as crashworthiness, the linear (1<sup>st</sup> order) or quadratic (2<sup>nd</sup> order) polynomial regression models are typically applied to construct “cheap-to-compute” surrogate models. The linear and quadratic polynomial models can be expressed as:

$$\hat{y} = \beta_0 + \sum_{i=1}^m \beta_i x_i \quad 3.12$$

$$\hat{y} = \beta_0 + \sum_{i=1}^m \beta_i x_i + \sum_{i=1}^m \beta_{ii} x_i^2 + \sum_{i=1}^{m-1} \sum_{j=i+1}^m \beta_{ij} x_i x_j \quad 3.13$$

where  $\hat{y}$  is the approximate function,  $m$  is the total number of design variables,  $x_i$  is the  $i^{\text{th}}$  design variable, and the  $\beta$ s are the unknown coefficients. The foregoing equation can be expressed in a matrix form as:

$$\mathbf{y} = \mathbf{X}\hat{\boldsymbol{\beta}} \quad 3.14$$

where  $\mathbf{X}$  is the design matrix of sampling points. The vector of unknown coefficients  $\hat{\boldsymbol{\beta}}$  represents the least-square estimator and is solved using the method of least squares as:

$$\hat{\boldsymbol{\beta}} = (\mathbf{X}^T \mathbf{X})^{-1} (\mathbf{X}^T \mathbf{y}) \quad 3.15$$

It is noted that the number of function evaluations required to construct the full quadratic function increases dramatically when the number of design variables increases.

### 3.3.2 Stepwise Regression

The stepwise regression is often referenced to an algorithm proposed by Efroymson (1960) [23]. The stepwise regression procedure starts off by choosing an equation containing the single best  $X$  variable and then attempts to build up with subsequent additions  $X$ 's one at a time as long as these additions are worthwhile. The order of addition is determined by using the partial  $F$ -test values to select which variable should enter next. The higher partial  $F$ -value is compared to an (selected or default) ' $F$ -to-enter' value. After a variable has been added, the equation is examined to see if any variable should be deleted. The procedure is described in the following:

### 3.3.2.1 Forward Selection

Let  $RSS_p$  denotes the residue sum of square (RSS) with  $p$  polynomial and constant terms in the regression model. The RSS is given by:

$$RSS = \sum_{i=1}^m (y_i - \hat{y}_i)^2 \quad 3.16$$

where  $m$  is the total number of sampling points ( $m > p$ ).  $y_i$  and  $\hat{y}_i$  are the “exact” and “approximate” responses of the sampling points, respectively.

Suppose the smallest  $RSS$  that can be obtained by adding another polynomial term set is  $RSS_{p+1}$ . The following ratio is calculated and compared with an ‘ $F$ -to-enter’ value,  $F_e$ :

$$R = \frac{RSS_p - RSS_{p+1}}{RSS_{p+1} / (m - p - 2)} \quad 3.17$$

If  $R$  is greater than  $F_e$ , the polynomial term is added to the selected set.

### 3.3.2.2 Backward Deletion

Having  $p$  terms (including the constant term) selected, let  $RSS_{p-1}$  be the smallest  $RSS$  that can be obtained after deleting any terms from the previously selected terms. The following ratio is calculated and compared with an ‘ $F$ -to-delete’ value,  $F_d$ :

$$R = \frac{RSS_{p-1} - RSS_p}{RSS_p / (m - p - 1)} \quad 3.18$$

If  $R$  is less than  $F_d$ , the polynomial term is deleted from the selected set.

### 3.3.3 Moving Least Square

Moving least square (MLS) was originated in curve and data fitting in 1981 (Lancaster *et al.*) [54]. The MLS approach has become quite popular since it has been used to construct shape functions in mesh-free method. In MLS, the interpolant  $u^h(x)$  of the function  $u(x)$  is:

$$u^h(x) = \sum_{i=1}^m P_i(x) \alpha_i(x) = \mathbf{P}^T(x) \mathbf{\alpha}(x) \quad 3.19$$

A linear basis and a quadratic basis in 1- $D$  are provided as:

$$\mathbf{P}^T(x) = [1 \quad x], \quad \mathbf{P}^T(x) = [1 \quad x \quad x^2] \quad 3.20$$

The coefficients  $\alpha_i(x)$  are obtained at any point  $x$  by minimizing a weighted, discrete  $L_2$  norm:

$$J = \sum_{i=1}^n w(x - x_i) [\mathbf{P}^T(x) \mathbf{\alpha}(x) - u_i]^2 \quad 3.21$$

where  $n$  is the number of points in the domain of influence. The stationary condition of  $J$  with respect to  $\mathbf{\alpha}(x)$  leads to:

$$\mathbf{\alpha}(x) = \mathbf{A}^{-1}(x) \mathbf{B}(x) \mathbf{u} \quad 3.22$$

where

$$\mathbf{A}(x) = \sum_{i=1}^m w(x - x_i) \mathbf{P}(x_i) \mathbf{P}(x_i)^T \quad 3.23$$

$$\mathbf{B}(x) = [w(x - x_1) \mathbf{P}(x_1) \quad w(x - x_2) \mathbf{P}(x_2) \quad \cdots \quad w(x - x_n) \mathbf{P}(x_n)] \quad 3.24$$

Hence we have:

$$u^h(x) = \sum_{i=1}^m P_i(x) \alpha_i(x) = \mathbf{p}^T(x) \mathbf{a}(x) = \sum_{i=1}^n N_i(x) u_i \quad 3.25$$

where the interpolant function  $N_i(x)$  is given by:

$$N_i(x) = \sum_{j=1}^m P_j(x) [\mathbf{A}^{-1}(x) \mathbf{B}(x)]_{ji} \quad 3.26$$

### 3.3.4 Kriging

Kriging is an interpolation method that originated in geostatistics. The method is named after D. G. Krige, who applied empirical methods for determining true ore grade distributions based on sampled ore grades. Kriging uses the properties of the spatial correlation among the data samples. In arriving at an interpolated value at some point in the parameter space, Kriging more heavily weights data samples that are “nearby” rather than giving all data samples equal weight. In Kriging, interpolation is achieved by setting the mean residue error to zero and minimizing the variance of the errors.

A spatial correlation metamodel is a combination of a polynomial model and departures of the following form:

$$y(\mathbf{x}) = f(\mathbf{x}) + Z(\mathbf{x}) \quad 3.27$$

where  $y(\mathbf{x})$  is the unknown function of interest,  $f(\mathbf{x})$  is a known polynomial and  $Z(\mathbf{x})$  is the localized deviations and the departure from the standard polynomial.  $Z(\mathbf{x})$  represents the realization of a stochastic component with mean zero, variance  $\sigma^2$  and non-zero covariance.

While  $f(\mathbf{x})$  “globally” approximates the design space,  $Z(\mathbf{x})$  creates “localized” deviations so that the kriging model interpolates the  $n_s$  sampled data points. The covariance of  $Z(\mathbf{x})$  that dictates the local deviations is given by:

$$\text{Cov}[Z(\mathbf{x}^i), Z(\mathbf{x}^j)] = \sigma^2 \mathbf{R}([R(\mathbf{x}^i, \mathbf{x}^j)]) \quad 3.28$$

where  $\mathbf{R}$  is the correlation matrix,  $R(\mathbf{x}^i, \mathbf{x}^j)$  is the correlation function between two sampled data points  $\mathbf{x}^i$  and  $\mathbf{x}^j$ .  $\mathbf{R}$  is a  $(n_s \times n_s)$  symmetric positive definite matrix with unit diagonal. The correlation function could be an exponential, Gaussian, cubic or any such kind of an approximation function. For a Gaussian correlation function,  $\mathbf{R}$  is given by:

$$R(\mathbf{x}^i, \mathbf{x}^j) = \exp \left[ - \sum_{k=1}^{ndv} \theta_k |x_k^i - x_k^j|^2 \right] \quad 3.29$$

where  $ndv$  is the number of design variables,  $\theta_k$  are the unknown correlation parameters, and  $|x_k^i - x_k^j|$  is the distance between the  $k^{\text{th}}$  components of points  $\mathbf{x}^i$  and  $\mathbf{x}^j$ . Once the correlation function has been selected, the predicted estimate of the response  $\hat{y}(\mathbf{x})$  at the untried values of  $\mathbf{x}$  is given by:

$$\hat{y}(\mathbf{x}) = \hat{\beta} + \mathbf{r}^T(\mathbf{x}) \mathbf{R}^{-1}(\mathbf{y} - \mathbf{f} \hat{\beta}) \quad 3.30$$

where  $\mathbf{r}^T(\mathbf{x})$  is the correlation vector between a predicted  $\mathbf{x}$  and the  $n_s$  sampling points,  $\mathbf{y}$  represents the responses at each sampling point and  $\mathbf{f}$  is an  $n_s$ -vector of ones (in the case that  $f(\mathbf{x})$  is taken as a constant). The vector  $\mathbf{r}$  and scalar  $\hat{\beta}$  are given by:

$$\mathbf{r}^T(\mathbf{x}) = [R(\mathbf{x}, \mathbf{x}^1), R(\mathbf{x}, \mathbf{x}^2), \dots, R(\mathbf{x}, \mathbf{x}^{n_s})]^T \quad 3.31$$

$$\hat{\beta} = (\mathbf{f}^T \mathbf{R}^{-1} \mathbf{f})^{-1} \mathbf{f}^T \mathbf{R}^{-1} \mathbf{y} \quad 3.32$$

The estimate of variance, of the sampling data, from the underlying global model is:

$$\hat{\sigma}^2 = \frac{(\mathbf{y} - \mathbf{f}\hat{\beta})^T \mathbf{R}^{-1} (\mathbf{y} - \mathbf{f}\hat{\beta})}{n_s} \quad 3.33$$

The maximum likelihood estimates for  $\theta_k$  can be found by solving the following constrained maximization problem:

$$\begin{aligned} \text{Maximize:} \quad & \Phi(\theta) = \frac{-[n_s \ln(\hat{\sigma}^2) + \ln|\mathbf{R}|]}{2} \\ \text{Subject to:} \quad & \theta \geq 0, \theta \in \mathfrak{R}^n \end{aligned} \quad 3.34$$

where both  $\hat{\sigma}$  and  $|\mathbf{R}|$  are functions of  $\Theta$ .  $\mathbf{R}$  is adaptively regularized because of potential ill-conditioning. The net effect is that the approximating functions no longer interpolate the observed response values exactly, but still closely approximate the observations.

### 3.3.5 Radial Basis Function

Given data set  $(\mathbf{x}_i, \mathbf{f}_i)$ ,  $i=1$  to  $n$ ,  $\mathbf{x}_i \in \mathfrak{R}^n, \mathbf{f}_i \in \mathfrak{R}$ , the interpolation of a radial basis function  $f(\mathbf{x})$  is expressed as a linear combination as:

$$f(\mathbf{x}) = \sum_{j=1}^n C_j \phi(\|\mathbf{x} - \mathbf{x}_j\|) \quad 3.35$$

where  $C_j$  are the interpolation constants to be determined,  $\phi$  are the radial basis functions,  $\|\mathbf{x} - \mathbf{x}_j\|$  is Euclidean norm representing the distance  $r$  of the point  $\mathbf{x}$  from the center node  $\mathbf{x}_j$ .

The unknown interpolation coefficients  $C_i$  can be determined by minimizing the  $L_2$  norm

$$J = \left[ \mathbf{f}_i - \sum_{i=1}^N C_j \phi(\mathbf{x}_i - \mathbf{x}_j) \right]^2 \quad 3.36$$

or in matrix form as:

$$[\mathbf{A}]\{\mathbf{C}\} = \{\mathbf{f}\} \quad 3.37$$

where

$$[\mathbf{A}] = \|\mathbf{x} - \mathbf{x}_j\| \quad 3.38$$

$$\{\mathbf{C}\}^T = \{C_1, C_2, \dots, C_N\} \quad 3.39$$

$$\{\mathbf{f}\}^T = \{f_1, f_2, \dots, f_N\} \quad 3.40$$

Note that the matrix  $[\mathbf{A}]$  is always invertible, provided that the data are not redundant. The commonly used classical radial basis functions are provided in Table 3.2.



Table 3.2 Commonly Used Radial Basis Functions

Type	Radial Basis Function
Linear	$\phi = hr$
Cubic	$\phi = (r + h)^3$
Thin Plate Spline	$\phi = r^2 \log(hr^2)$
Gaussian	$\phi = e^{-hr^2}$
Multiquadric	$\phi = \sqrt{r^2 + h}$
Inverse Multiquadric	$\phi = 1/\sqrt{r^2 + h}$

where  $r = \|\mathbf{x} - \mathbf{x}_j\|$ .

### 3.3.6 Adaptive and Interactive Modeling System (AIMS)

Adaptive and Interactive Modeling System (AIMS) is a hybrid metamodeling system [55]. It uses machine learning and statistical techniques to induce models from training examples that are generally obtained from math models through simulation or from physical experiments. AIMS uses a recursive decomposition method to split the design space into less complicated sub-regions and fits each region with an appropriate surrogate model.

The AIMS consists of two major components: Competitive Relation Learner (CRL) and Induction/Selection Optimizer (ISO). The CRL is the learning component. It is responsible for generating metamodels from training examples. It has many control parameters (called biases) that can influence the properties of the metamodels. The CRL evaluates multiple competing learning strategies and chooses the most appropriate

one for each sub-region in the design space. The decision of choosing a particular learning strategy depends on the modeling objectives. The current implementation of the CRL contains statistical regression, inductive learning strategies, such as linear regression, prototype and neural nets, and decomposition algorithms that are based on distance or population measures. Both learning strategies and decomposition algorithms have biases that affect the accuracy, formation time, and the form of the resulting surrogate models. The ISO is the optimization component in AIMS. It uses a multiple-objective optimization method to select the most appropriate modeling strategies and associated control parameters (biases), such as the decomposition method, the learning method, and the number of layers and neurons of neural nets for the CRL. These biases are designed to satisfy user specified modeling objectives such as model accuracy and evaluation time. ISO uses an induction-based procedure for optimizing the bias space formed by the learning strategies and decomposition algorithms. The inputs to ISO are a bias space and modeling objectives, and the output is a set of optimal biases. Optimization in the ISO is iterative, consisting of three steps: selection, evaluation, and induction. In a typical AIMS application, ISO first selects a bias from the bias space randomly. The CRL uses this bias to generate a metamodel based on training examples. The ISO evaluates the model by checking its objective score against the objective functions and selects the next bias. The CRL uses the new bias to generate a new metamodel with the same training examples. The iteration continues until a desirable set of metamodels is obtained.

### 3.3.7 Multivariate Adaptive Regression Splines (MARS)

Multivariate Adaptive Regression Splines is a nonlinear regression technique that fits high dimensional data to an expansion in multivariate basis functions. The number of basis functions, the product degree, and the knot locations are automatically determined by, and adaptive to, the data. The model produces strictly continuous approximation with continuous derivatives, and identifies the contributions from additive terms and multivariable interactions. The approximation takes the form of an expansion in multivariate spline basis functions:

$$\hat{y} = a_0 + \sum_{m=1}^M a_m B_m(x_1, \dots, x_n) \quad 3.41$$

where:

$$B_m(x_1, \dots, x_n) = \prod_{k=1}^{K_m} b_{km}(x_{v(k,m)} | t_{km}) \quad 3.42$$

with:

$$B_o(x_1, \dots, x_n) = 1 \quad 3.43$$

The  $\{a_m\}_0^M$  are the coefficients of the expansion, obtained by minimizing a generalized cross-variance criterion that is the average squared residual of the fit to the data times a penalty to account for the increased variance associated with increasing model complexity. Each multivariate spline basis function  $B_m$  is the product of univariate spline basis function  $b_{km}$  which is either order 1 or cubic, depending on the

degree-of-continuity of the approximation, each of a single input variable  $x_{v(k,m)}$  and characterized by a knot at  $t_{km}$ . The multivariate spline basis functions  $B_m$  are adaptive.

### 3.4 Comparative Study of Surrogate Models

#### *3.4.1 Introduction*

In this section, a real-world full vehicle frontal impact problem, as shown in Figure 3.3, is studied using five metamodeling techniques: Stepwise Regression (SR), Moving Least Square (MLS), Kriging (KG), Multiquadric (MQ), and Adaptive and Interactive Modeling System (AIMS). These metamodels are used to investigate the model accuracy for two safety performance attributes: toe-board intrusion and Head Injury Criteria (HIC).

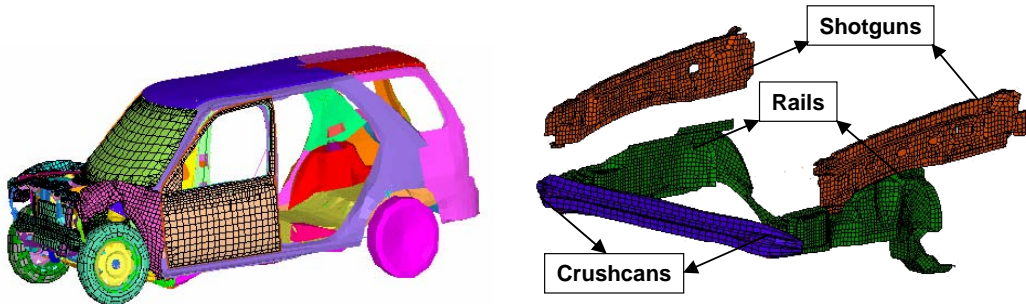


Figure 3.3 Frontal Impact Finite Element Model and Selected Design Variables for Comparative Study of Surrogate Models

Vehicle safety design is one of the major attributes in vehicle product development. The vehicle must be designed to absorb enough impact energy through structural deformation and attenuate the impact force to a tolerable level to protect the occupants when impact occurs. More and more impact scenarios are now required to

evaluate the vehicle performance such as: full frontal impact, frontal offset impact, roof crush, rear impact and side impact. The full frontal impact is commonly used to design and validate the vehicle front-end structures while satisfying the federal safety regulations for FMVSS (Federal Motor Vehicle Safety Standards) 208 as well as corporate requirements. The key performance measures in the full frontal impact include: toe-board intrusion, HIC, chest G and chest deflection.

#### *3.4.2 Finite Element Model*

The full vehicle finite element model is used in this paper. It contains about 75,500 shell elements, as shown in Figure 3.3. The simulation speed is 35 mph against a rigid wall. The simulation time used in this study is 80ms. The computing time for one such analysis requires about 17 hours on a CRAY J916/16 machine using 8 CPUs. The explicit finite element commercial software, RADIOSS from MECALOG, is used to solve this highly nonlinear, transient, dynamic, and large deformation frontal impact simulation. Four major components in the frontal impact event are chosen as the design variables. They are the thicknesses of the crush cans, the inner and outer parts of the rails, and the shotguns, as shown in Figure 3.3. Two major performance measures, toeboard intrusion and HIC (Head Injury Criteria), are selected for investigating the accuracy and convergence rate of the metamodels. The HIC number is calculated using a commercial multi-body occupant simulation product, MADYMO from TNO by importing the rocker/B-Pillar acceleration pulse from the RADIOSS analysis results. The occupant model used in this study consists of: restraint system with airbag, seat model, steering wheel model, dummy model, and simplified model of the drivers space

with toeboard, dashboard, and windshield, as shown in Figure 3.4. The HIC number is calculated as:

$$HIC = \left( \left[ \frac{1}{t_2 - t_1} \int_{t_1}^{t_2} a dt \right]^{2.5} (t_2 - t_1) \right)_{\max} \quad 3.44$$

where  $a$  is the acceleration pulse in G's,  $t_1, t_2$  is expressed in second and measured during impact,  $(t_2 - t_1)$  is within 36ms.

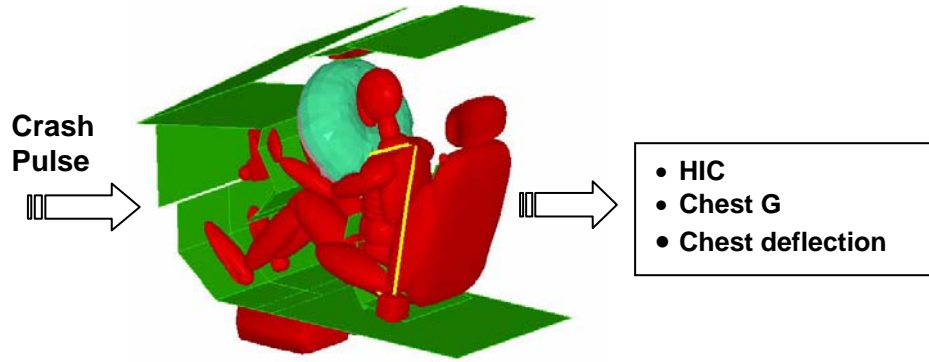


Figure 3.4 Occupant Restraint System Model to Evaluate Injury Numbers for Comparative Study of Surrogate Models

### 3.4.3 Numerical Results

The so-called adjusted coefficient of determination or  $R^2_{adjusted}$  is commonly used as an error indicator in regression fit to check the accuracy and examine whether the regression model is overfitting. However, since the KG and MQ metamodels pass through all sampling points, it is unsuitable to use the  $R^2_{adjusted}$  in this study. Instead, the Root Mean Square (RMS) error is employed as the error indicator and is defined as follows:

$$RMS = \sqrt{\frac{1}{k} \sum_{i=1}^k \varepsilon_i^2} \quad 3.45$$

where  $\varepsilon_i$  is the error at each evaluated point and  $k$  is the number of the evaluation data sets.

The optimal Latin Hypercube Sampling is chosen to explore the design space in this particular problem. As mentioned earlier that unlike the conventional factorial DOE, the LHS is capable of capturing the higher order of nonlinearity using a larger number of levels with fewer design points. To ensure the uniformity of the sampling points within the region of interest, a combinatorial optimization algorithm is performed based on an entropy criterion to minimize the bias part of Mean Square Error (MSE). Five sampling data sets are created for studying the accuracy and convergence rate of each metamodel, i.e.  $3N$ ,  $6N$ ,  $9N$ ,  $18N$  and  $36N$ , where  $N$  is the number of design variables. The sample sizes are selected for achieving uniformity and balancing of the sampling points within the design domain.

Since AIMS is a hybrid system that includes statistical regression and inductive learning strategies, only the pure neural network is selected to fit the nonlinear functions for the purpose of consistency. The SR uses up to the quadratic polynomial. The CAE data of the frontal impact is based on a full factorial design. Based on the number of levels defined in Table 3.3, a total of 144 ( $3 \times 4 \times 4 \times 3$ ) simulations are performed. Additional 24 points, which scatter over the design domain but excluded from the training data, are generated to evaluate the accuracy and convergence rate.

Table 3.3 Description of Design Variable, Lower Bound, Upper Bound and DOE Levels for Frontal Impact Problem

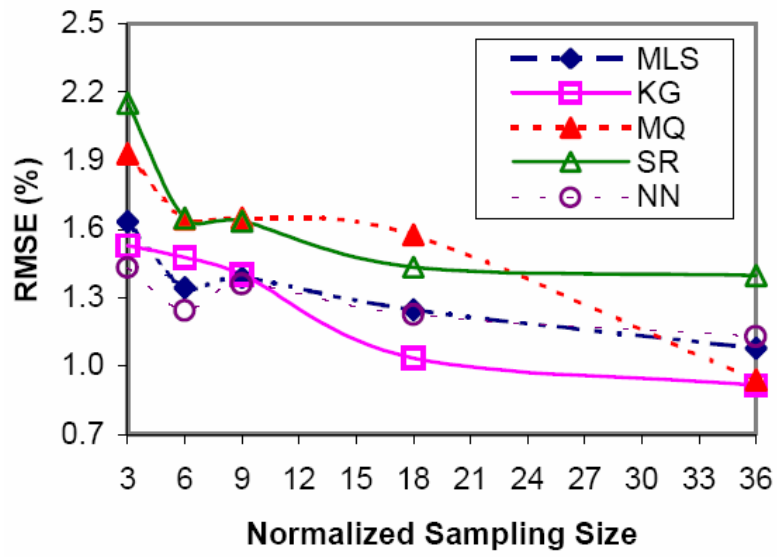
Design Variable	Bounds (mm)	Level	No. of Levels
Crushcan	[0.8, 2.0]	[1.2, 1.5, 1.75]	3
Rail Inner	[2.0, 3.0]	[1.75, 2.0, 2.3, 2.5]	4
Rail Outer	[2.0, 3.0]	[1.75, 2.0, 2.3, 2.5]	4
Shotgun	[0.8, 2.0]	[1.2, 1.5, 1.75]	3

The plots of the RMS error vs. sample size in real scale for the toe-board intrusion and HIC number are shown in Figures 3.5 (a) and 3.6 (a), respectively. Figures 3.5 (b) and 3.6 (b) shows the RMS error vs. sample size in log-log scale. The corresponding RMS percentage is given in Tables 3.4 and 3.5. Note that the sample size is normalized with respect to the number of design variables,  $N$ . It is observed that for sample size less than  $9N$ , all metamodels appear to perform poorly. In general, the results of the RMS error vs. normalized sample size oscillate and lack of consistency. For sample size larger than  $9N$ , although it is not clear to identify the best metamodel for both the toe-board intrusion and HIC, the trends appear to be smoother and much more consistent. The accuracy and convergence rate of the MQ seem to be better than the others. The convergence rate is poorer and the results do not improve much when more training data are added. The KG outperforms other methods for the toe-board intrusion but has the poorest performance for HIC.

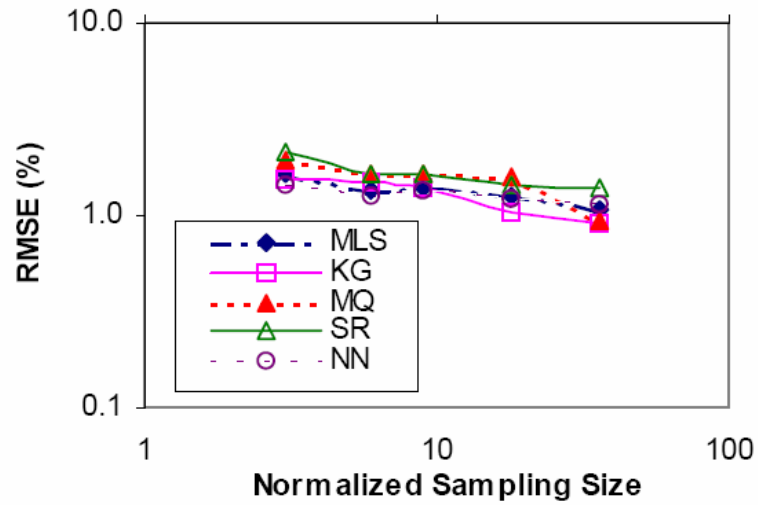
To get more insights into these metamodels, the surface plots for the toe-board intrusion and HIC are generated, using the complete full factorial data ( $36N$ ), as shown



in Figures 3.7 and 3.8, respectively. For the toe-board intrusion, both the MQ and KG give very similar and accurate approximations, evidenced by the lowest and the same RMS error (0.9%). The SR shows the worst surface plot. Although it captures the trend, the accuracy for local regions is poor. It becomes more obvious for the HIC. It is shown from Table 3.5 that the most accurate surface plot comes from the MQ (RMS error=2.3%) with sample size of  $36N$ . Assuming this represents the true model, the surface plots using KG and MQ are still quite good and similar, even though some of the local regions are not well represented. As for the SR, it completely missed the local minimum region and it will not be able to find the global optimal design.

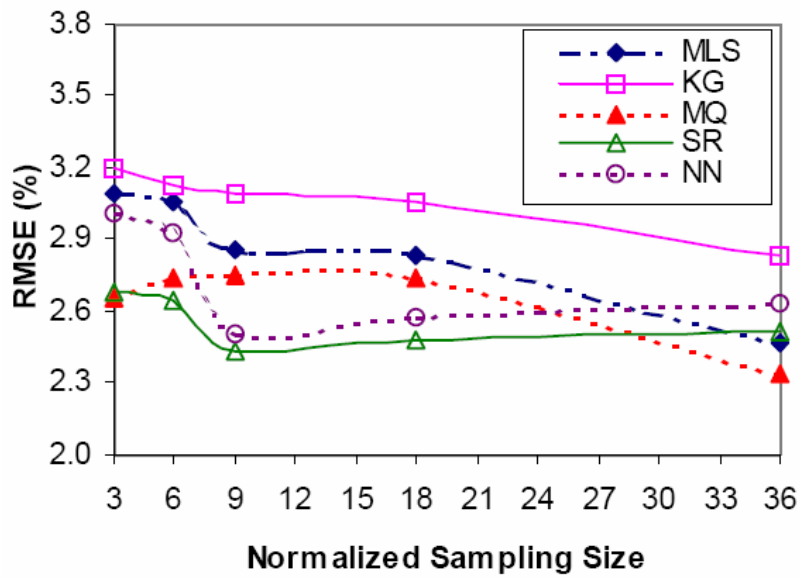


(a)

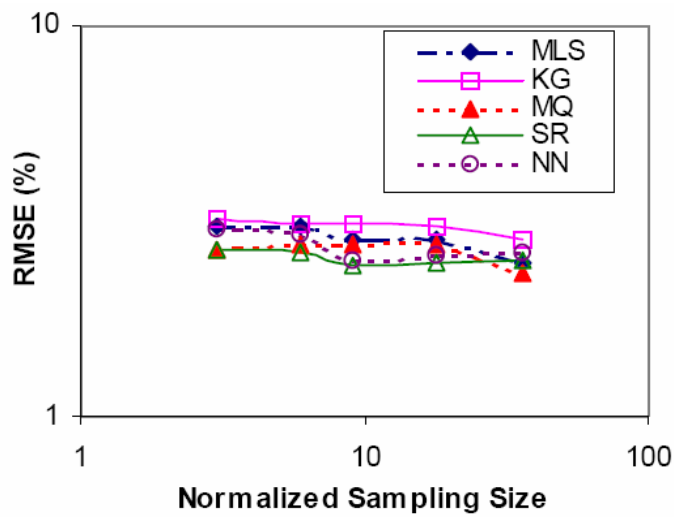


(b)

Figure 3.5 RMS Error vs. Sample Size for Toe-Board Intrusion in the Frontal Impact Problem: (a) Real Scale, (b) Log-Log Scale



(a)



(b)

Figure 3.6 RMS Error vs. Sample Size for HIC Injury Number Predicted by Occupant Restraint System Analysis in the Frontal Impact Problem: (a) Real Scale, (b) Log-Log Scale

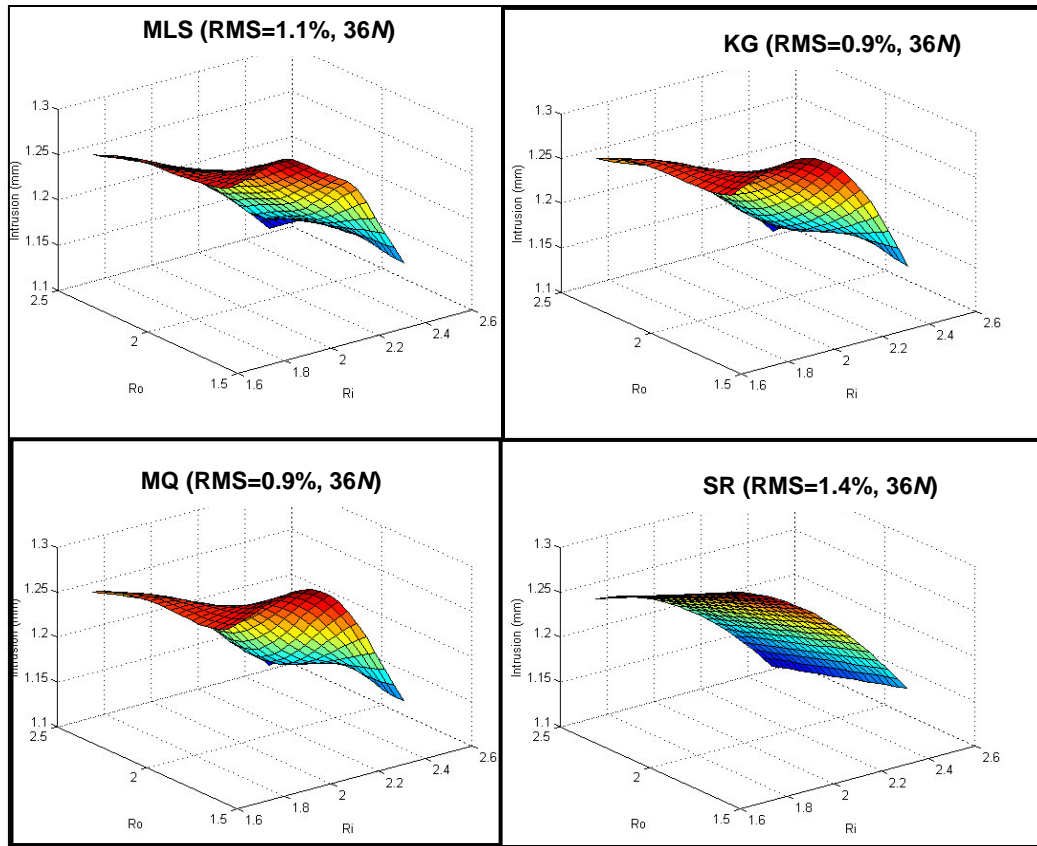


Figure 3.7 Surface Plot Comparison for Normalized Toe-Board Intrusion Using 36N Sample Size in Frontal Impact Problem

Table 3.4 Model Accuracy Comparison Using RSM Error for Toe-Board Intrusion in Frontal Impact Problem

Sample Size	MLS	KG	MQ	SR	AIMS (NN)
3N	1.6	1.5	1.9	2.2	1.4
6N	1.3	1.5	1.6	1.7	1.2
9N	1.4	1.4	1.6	1.6	1.4
18N	1.2	1.0	1.6	1.4	1.2
36N	1.1	0.9	0.9	1.4	1.1

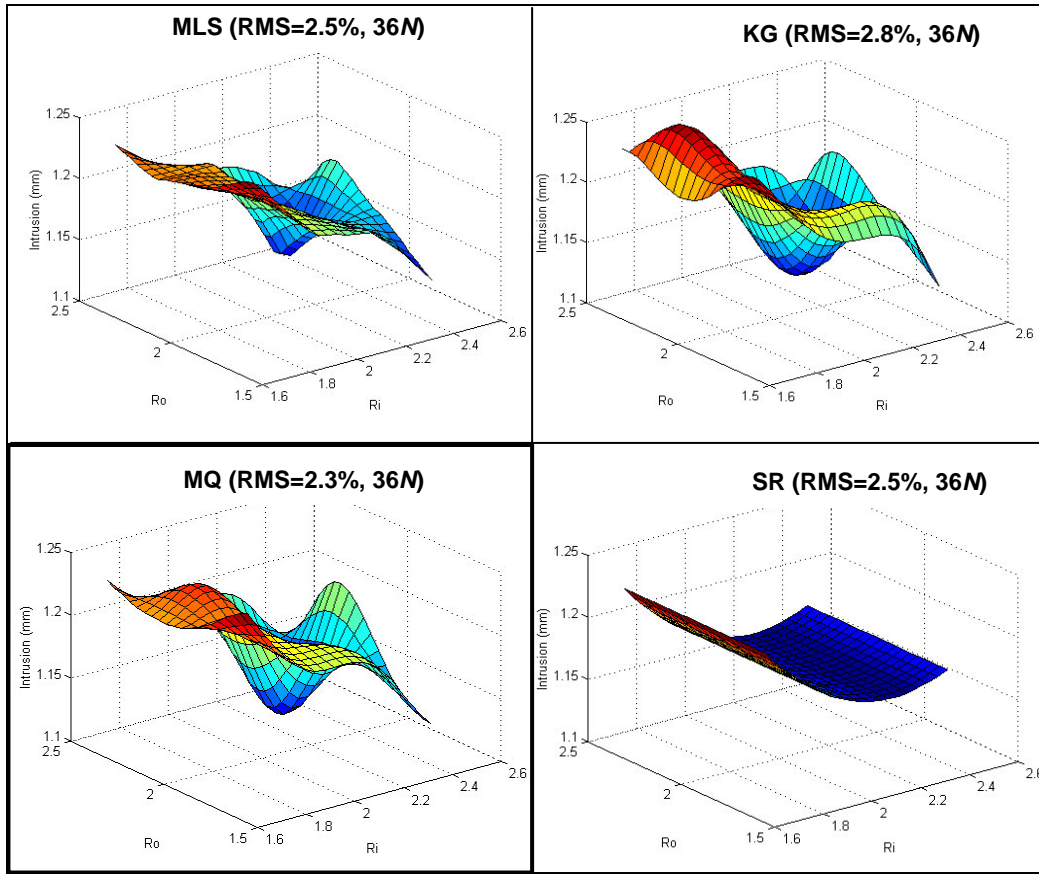


Figure 3.8 Surface Plot Comparison for Normalized HIC Injury Number Using 36N Sample Size in Frontal Impact Problem

Table 3.5 Model Accuracy Comparison Using RSM Error for HIC Injury Number in Frontal Impact Problem

Sample Size	MLS	KG	MQ	SR	AIMS (NN)
3N	3.1	3.2	2.7	2.7	3.0
6N	3.1	3.1	2.7	2.6	2.9
9N	2.9	3.1	2.8	2.4	2.5
18N	2.8	3.1	2.7	2.5	2.6
36N	2.5	2.8	2.3	2.5	2.6

### 3.5 Aluminum Foam-Filled Front Rail Impact Optimization

#### *3.5.1 Introduction*

The front rails are the most important structural member in frontal collision. They absorb about 50% of crash energy during the collision process. The design of front rail has to satisfy both crashworthiness and weight efficiency requirements, and therefore has become a focus of activity in the crashworthiness design of full vehicle structure. The results presented in this section was a collaborative research effort with Impact and Crashworthiness Laboratory of Massachusetts Institute of Technology.

#### *3.5.2 Finite Element Model*

Figure 3.9 shows the front rail finite element model. Two main outer panels are assembled by spot-welding, and the stiffeners are attached inside of the rail. In the front part, crush triggers in the form of corrugated flanges are placed to reduce the peak load, induce progressive folding in the axially collapsing part, and to avoid the global bending collapse. The approximate dimension of the front end section is 100 mm  $\times$  130 mm. The subframe or cradle is attached to the rail by a rigid body constraint representation. A total of 4,825 shell elements are employed to construct the finite element model. The impact velocity of the front rail is 31 mph into a rigid wall. The simulation termination time is taken to be 30 msec, and the added mass of 713.9 kg is attached to the end part of the front rail to compensate for the mass of entire vehicle structure. As this model represents a half of the front rail and subframe, symmetry boundary conditions are applied to the nodes of the cradle on the plane of symmetry.

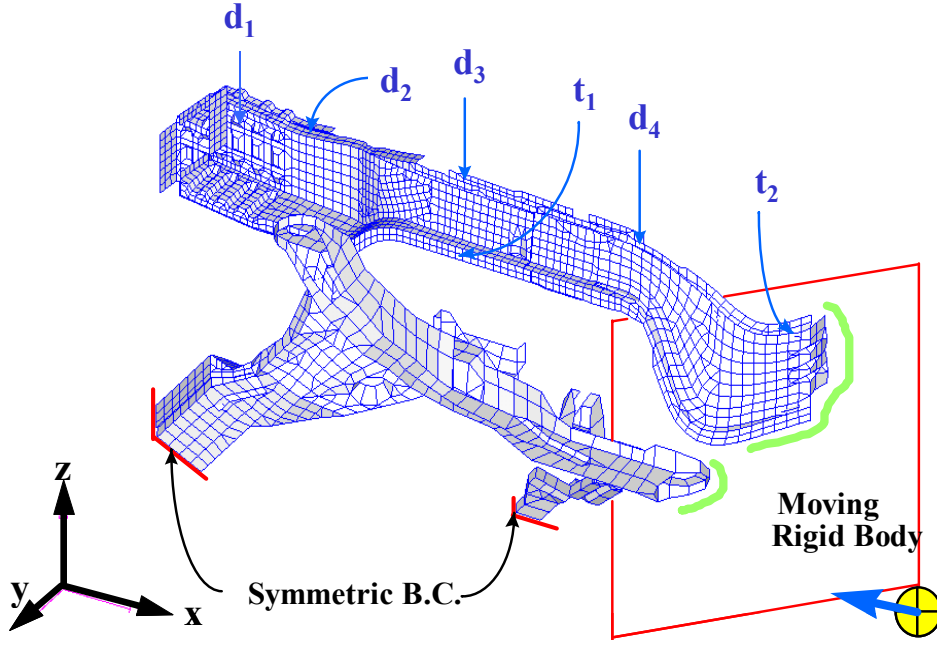


Figure 3.9 Front Rail Finite Element Model

Four parts of the front rail are reinforced individually by using the aluminum foam filler. The aluminum foam model used in this study represent the HYDRO aluminum foam with plastic flow stress of bare foam material  $\sigma_{0,f}=150$  Mpa. The idealized mechanical behavior of the foam under compression is illustrated in Figure 3.10. The mechanical properties of foam material definition are:

$$E = E_s \left( \frac{\rho}{\rho_s} \right)^2 \quad 3.46$$

$$E_{t1} = 0.02E \quad 3.47$$

$$G = E \quad 3.48$$

$$\sigma_f = \sigma_{0,f} \left( \frac{\rho}{\rho_s} \right)^{1.5} \quad 3.49$$

$$\tau_f = 0.5\sigma_{0,f} \left( \frac{\rho}{\rho_s} \right)^{1.5} \quad 3.50$$

$$\varepsilon_c = 1 - 1.4 \frac{\rho}{\rho_s} \quad 3.51$$

where  $E$  is the Young's modulus,  $E_{t1}$  is the first tangent modulus,  $G$  is the shear modulus,  $\sigma_f$  is the foam crushing strength,  $\tau_f$  is the foam shear crushing strength, and  $\varepsilon_c$  is the densification strain.

Note that all the mechanical properties of the foam filler are determined by the foam relative density  $d = \rho_f / \rho_s$  where  $\rho_s$  is the mass density of solid cell wall of the foam and  $\rho_f$  is the foam density. In this study, the relative density of foam is used as the design parameter to determine the foam strength. Namely, there are total six design variables including four foam densities and two gage thickness.

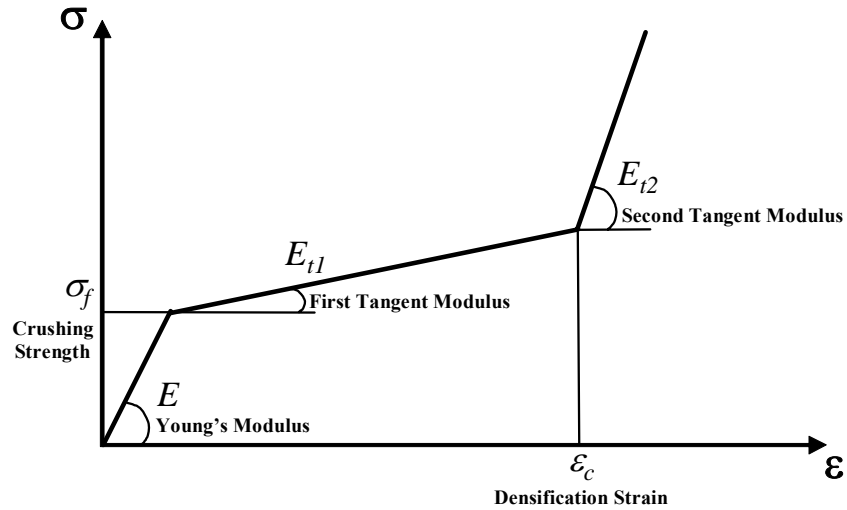


Figure 3.10 Mechanical Properties of Aluminum Foam under Compression



### 3.5.3 Surrogate-Based Optimization Algorithm

In this study, the optimal Latin Hypercube Sampling (LHS) method is selected to explore the uniform design points uniformly on the front rail design space. The sample size is chosen to be 24 or  $4N$  (where  $N$  is the number of design variables). The number of levels of each design variable in LHS is set to be 10 to capture the nonlinearity of the responses. Table 3.6 shows the optimal LHS DOE and finite element response matrices for the foam-filled front rail problem. Among the RSM methods, the quadratic stepwise regression is chosen to construct the surrogate model being used in the numerical optimization process. In this study, the response surface function of the structural weight is constructed using the linear basis function while the quadratic basis function is selected to construct the internal energy and initial average force response functions. The explicit form of the functions in terms of the design variables (gages and foam relative densities) obtained from the stepwise regression is shown in the following:

$$W = 14.22 + 3.133t_1 + 1.654t_2 + 5.352d_1 + 6.077d_2 + 7.110d_3 + 3.201d_4 \quad 3.52$$

$$IE = 6046 + 2615t_1 + 16020d_2 - 1886t_1d_2 + 2956t_1d_3 - 4080t_2d_2 + 7107t_2d_3 + 4587t_2d_4 - 12740d_1d_2 + 26080d_1d_3 - 210.6t_1^2 - 41410d_3^2 \quad 3.53$$

$$IAF = 25.1 + 62.96d_1 + 6.66t_1t_2 \quad 3.54$$

Figure 3.11 illustrates the surrogate-based optimization algorithm. The Sequential Quadratic Programming (SQP) solver is used in the optimization process. After each approximate optimization, a CAE confirmation analysis is conducted to check the accuracy and convergence of the approximate response surface functions.

Three single objective optimization problems are investigated to achieve a more balanced design between the structural weight and internal energy:

1.     Minimize     Weight  
       Subject to      $IE \geq 17,000 \text{ J}$   
                          $IAF \leq 55 \text{ kN}$
2.     Maximize     IE  
       Subject to     Weight  $\leq 26.2 \text{ kg}$   
                          $IAF \leq 55 \text{ kN}$
3.     Minimize     Weight  
       Subject to      $IE \geq 12,110 \text{ J}$   
                          $IAF \leq 40 \text{ kN}$

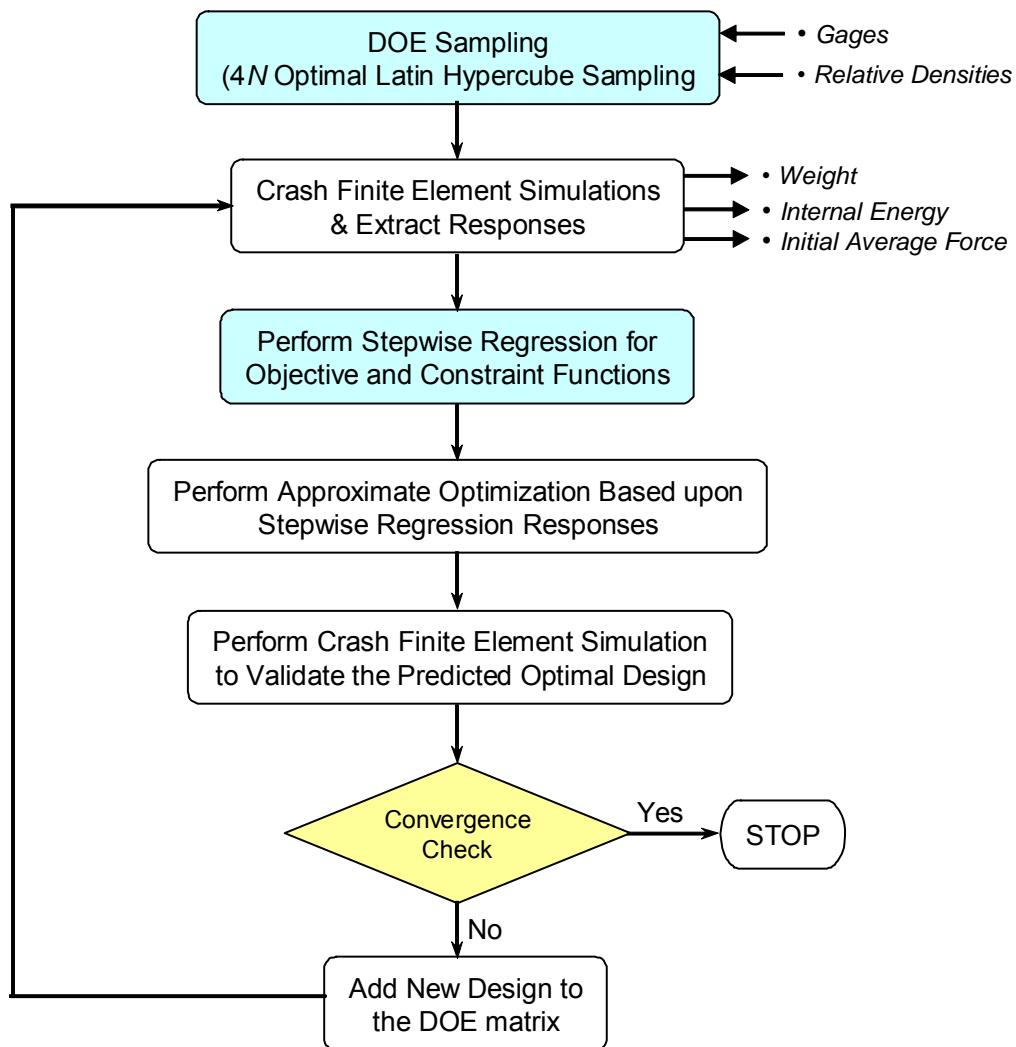


Figure 3.11 Surrogate-Based Optimization Algorithm

Table 3.6 Optimal LHS DOE matrix and Finite Element Response Matrix for Foam-Filled Front Rail Optimization Problem

	$t_1$ (mm)	$t_2$ (mm)	$d_1$	$d_2$	$d_3$	$d_4$	Weight (kg)	IE (J)	IAF (kN)
Baseline	1.9000	1.9000	0.0300	0.1800	0.2000	0.2000	26.65	14,570	47.38
1	1.2111	1.4667	0.1667	0.1389	0.0000	0.0000	22.18	9,338	43.51
2	1.4667	2.7444	0.0000	0.1944	0.0278	0.0830	25.02	11,220	51.28
3	1.2111	2.7444	0.0833	0.0833	0.1667	0.2500	25.50	15,010	61.03
4	1.9778	1.7222	0.0000	0.2500	0.1944	0.1667	26.71	15,390	40.74
5	2.2333	1.9778	0.1944	0.0000	0.1944	0.0000	26.90	14,380	68.05
6	3.0000	1.2111	0.0833	0.0833	0.0556	0.0000	26.98	13,230	65.31
7	1.4667	0.9556	0.1667	0.0000	0.0556	0.1667	22.22	11,120	41.49
8	2.7444	2.4889	0.2500	0.1667	0.0833	0.0278	29.95	14,090	81.27
9	3.0000	1.2111	0.0556	0.1111	0.1111	0.2500	28.21	15,520	61.80
10	2.4889	2.4889	0.0833	0.0278	0.0000	0.1389	27.20	12,980	71.53
11	1.4667	2.2333	0.1667	0.1944	0.0000	0.2500	25.39	12,830	58.88
12	1.7222	2.2333	0.2500	0.2222	0.2222	0.1944	28.16	16,120	65.82
13	3.0000	3.0000	3.0000	0.2222	0.1111	0.1944	31.94	17,040	86.07
14	0.7000	0.7000	0.1111	0.1667	0.1667	0.2222	21.08	11,070	27.78
15	2.2333	3.0000	0.0556	0.1111	0.2222	0.0556	28.91	16,160	76.19
16	0.7000	1.4667	0.2222	0.0556	0.2500	0.1111	22.51	10,570	39.82
17	0.9556	1.7222	1.7222	0.0278	0.1389	0.0278	21.47	9,770	34.93
18	2.7444	2.2333	0.2500	0.0556	0.1389	0.2222	29.88	16,990	79.45
19	1.7222	0.7000	0.0000	0.1667	0.0278	0.1111	22.35	12,460	20.63
20	1.9778	1.4667	0.0278	0.0000	0.2500	0.1667	25.34	13,000	20.96
21	0.7000	1.9778	0.1389	0.2500	0.1667	0.0556	23.30	11,650	44.69
22	2.2333	0.9556	0.1944	0.2500	0.0833	0.1389	26.39	13,880	57.51
23	0.9556	3.0000	0.2222	0.0833	0.0833	0.0833	24.72	12,040	61.52
24	2.4889	0.7000	0.1389	0.1389	0.2500	0.0833	26.81	14,120	57.75

### 3.5.4 Numerical Results

The design history along with validation values and error percentage for each of the design iteration are shown in Tables 3.7 to 3.9. Note that the weight constraint of 26.2 kg in Formulation 1 and internal energy of 12110 J in Formulation 3 are based upon the original empty model with internal sheet metal stiffeners. The numbers highlighted are the optimal design chosen for each of the formulations. For Formulation 1, the energy absorption is increased by 41% (from 12110 to 17097 J) and the structural weight is increased by 7% (from 26.2 to 28.1 kg) compared to the original empty foam-filler model. However, the initial average force constraint is violated and

more iteration is required for the optimization process. For Formulation 2, the optimization problem converges after three design iterations. The optimization results show that the internal energy is increased by about 37% (from 12110 to 16534 J) while the weight remains unchanged compared to the original model. About 15% of structural weight is reduced in the Formulation 3 while the energy absorption is maintained the same as the original baseline model.

Table 3.7 Design History for Single Objective Formulation 1

<b>Design Iteration 1</b>				
	<i>Obj/Constr</i>	<i>Prediction</i>	<i>Validation</i>	<i>Error %</i>
<b>Weight (kg)</b>	Minimize	26.8	26.8	0
<b>IE (J)</b>	$\geq 17000$	17000	16269	4.5
<b>IAF (kN)</b>	$\leq 55$	53.8	52.9	1.7
<b>Design Iteration 2</b>				
	<i>Obj/Constr</i>	<i>Prediction</i>	<i>Validation</i>	<i>Error %</i>
<b>Weight (kg)</b>	Minimize	28.1	<b>28.1</b>	0
<b>IE (J)</b>	$\geq 17000$	17000	<b>17097</b>	-0.6
<b>IAF (kN)</b>	$\leq 55$	55.0	<b>56.4</b>	-2.5
<b>Design Iteration 3</b>				
	<i>Obj/Constr</i>	<i>Prediction</i>	<i>Validation</i>	<i>Error %</i>
<b>Weight (kg)</b>	Minimize	28	28	0
<b>IE (J)</b>	$\geq 17000$	17000	16660	2
<b>IAF (kN)</b>	$\leq 55$	55.0	66.7	-1.2

Table 3.8 Design History for Single Objective Formulation 2

<b>Design Iteration 1</b>				
	<i>Obj/Constr</i>	<i>Prediction</i>	<i>Validation</i>	<i>Error %</i>
<b>Weight (kg)</b>	$\leq 26.2$	26.2	26.2	0
<b>IE (J)</b>	Maximize	16594	15851	4.7
<b>IAF (kN)</b>	$\leq 55$	52.2	49.7	5.0
<b>Design Iteration 2</b>				
	<i>Obj/Constr</i>	<i>Prediction</i>	<i>Validation</i>	<i>Error %</i>
<b>Weight (kg)</b>	$\leq 26.2$	26.2	26.2	0
<b>IE (J)</b>	Maximize	16141	16454	-1.9
<b>IAF (kN)</b>	$\leq 55$	55.0	54.9	0.2
<b>Design Iteration 3</b>				
	<i>Obj/Constr</i>	<i>Prediction</i>	<i>Validation</i>	<i>Error %</i>
<b>Weight (kg)</b>	$\leq 26.2$	26.2	<b>26.2</b>	0
<b>IE (J)</b>	Maximize	16310	<b>16534</b>	-1.4
<b>IAF (kN)</b>	$\leq 55$	55.0	<b>54.7</b>	0.5

Table 3.9 Design History for Single Objective Formulation 3

<b>Design Iteration 1</b>				
	<i>Obj/Constr</i>	<i>Prediction</i>	<i>Validation</i>	<i>Error %</i>
<b>Weight (kg)</b>	Minimize	22.9	22.9	0
<b>IE (J)</b>	$\geq 12110$	12110	11417	6.1
<b>IAF (kN)</b>	$\leq 40$	40.0	40.5	1.2
<b>Design Iteration 2</b>				
	<i>Obj/Constr</i>	<i>Prediction</i>	<i>Validation</i>	<i>Error %</i>
<b>Weight (kg)</b>	Minimize	22.3	<b>22.3</b>	0
<b>IE (J)</b>	$\geq 12100$	12110	<b>12737</b>	-4.9
<b>IAF (kN)</b>	$\leq 40$	40.0	<b>39.3</b>	1.8
<b>Design Iteration 3</b>				
	<i>Obj/Constr</i>	<i>Prediction</i>	<i>Validation</i>	<i>Error %</i>
<b>Weight (kg)</b>	Minimize	22.1	22.1	0
<b>IE (J)</b>	$\geq 12100$	12110	11861	2.1
<b>IAF (kN)</b>	$\leq 40$	40.0	45.0	-11.1

From the results above, it is clearly seen that for the axially collapse part, low strength of foam is preferable, and high strength foam is better for global bending zone. The rigid wall force of the optimal designs as well as the original baseline model is

shown in Figure 3.12. In all optimal designs, the peak force is reduced considerably while the bending resistance is almost doubled.

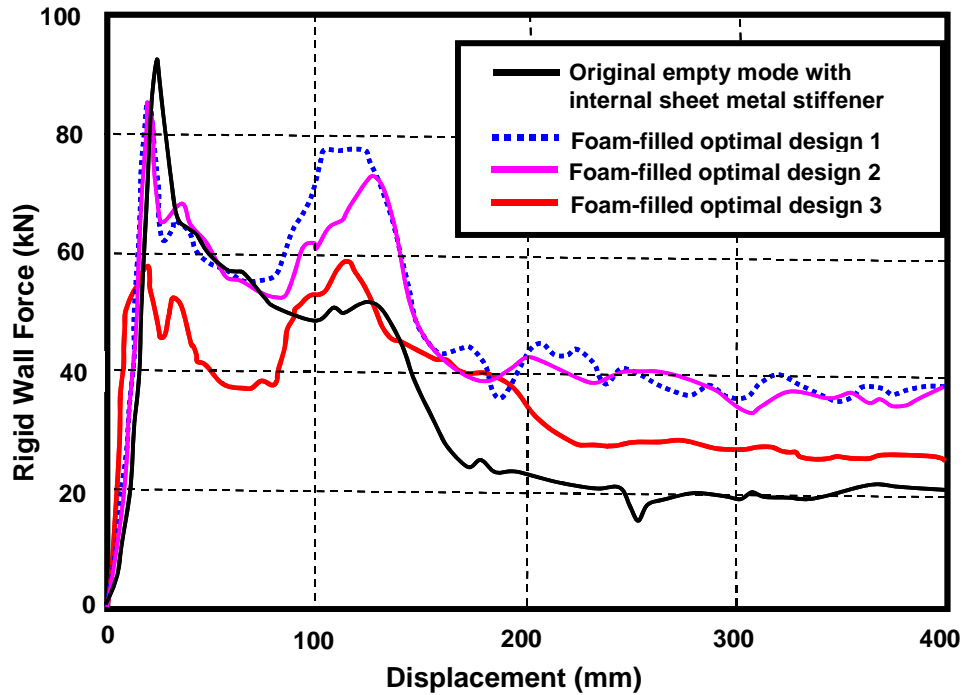


Figure 3.12 Rigid Wall Forces of Optimal Designs and Original Baseline Model for Aluminum Foam-Filled Front Rail

### 3.5.5 Weight Efficiency

The measure used to assess the weight efficiency of the model is Specific Energy Absorption (SEA). Figure 3.13 shows that as much as up to 37% increase of SEA are achieved in the optimal designs of aluminum foam-filled front rail compared to the original non-filled model with internal sheet metal stiffeners. Note that the baseline model value in the bar chart is normalized to 1.0 for ease of comparison. Figure 3.14 illustrates the relation between the structural weight and the absorbed energy. It is clearly seen that as the structural weight increases, the absorbed energy increases. The

lower and upper bounds of the distribution are plotted as in dashed lines. The points of the optimal designs are located on or above the upper bound, which means highest weight efficiency. In addition, the result of the original empty model with stiffeners made of sheet metal is plotted as an empty square, which is located at the lower bound. Therefore, it is shown that the reinforcement of the front rail by using foam-filler gives either reduced weight while maintaining the same level of energy absorption (horizontal arrow) or, increased energy absorption while maintaining the same structural weight (vertical arrow). In either case, considerable improvement in the performance is achieved.

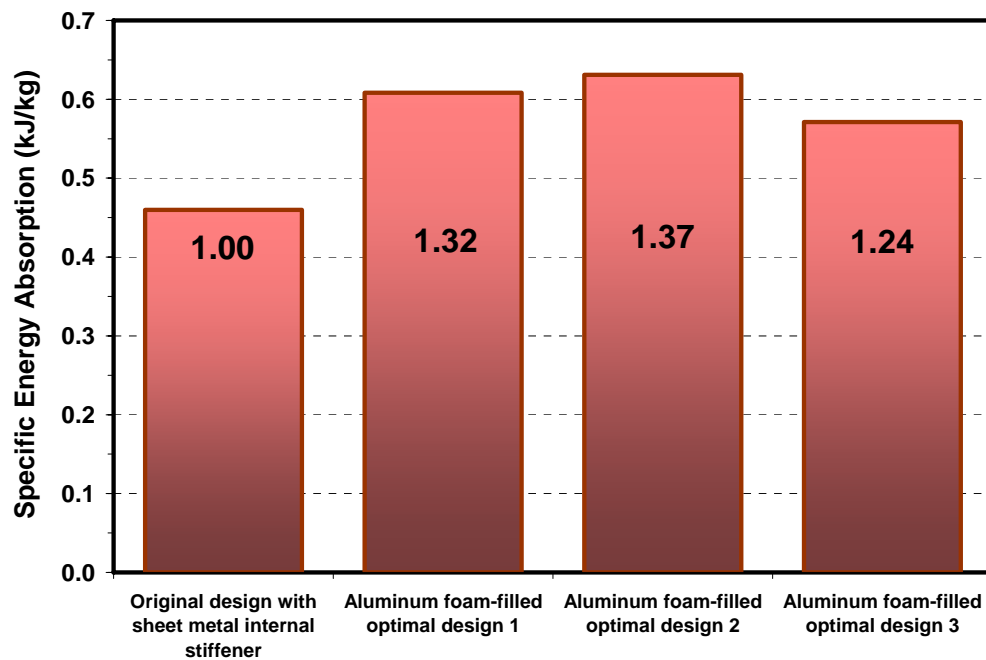


Figure 3.13 Comparison of the Specific Energy Absorption between Original Baseline Design and Foam-Filled Optimal Designs



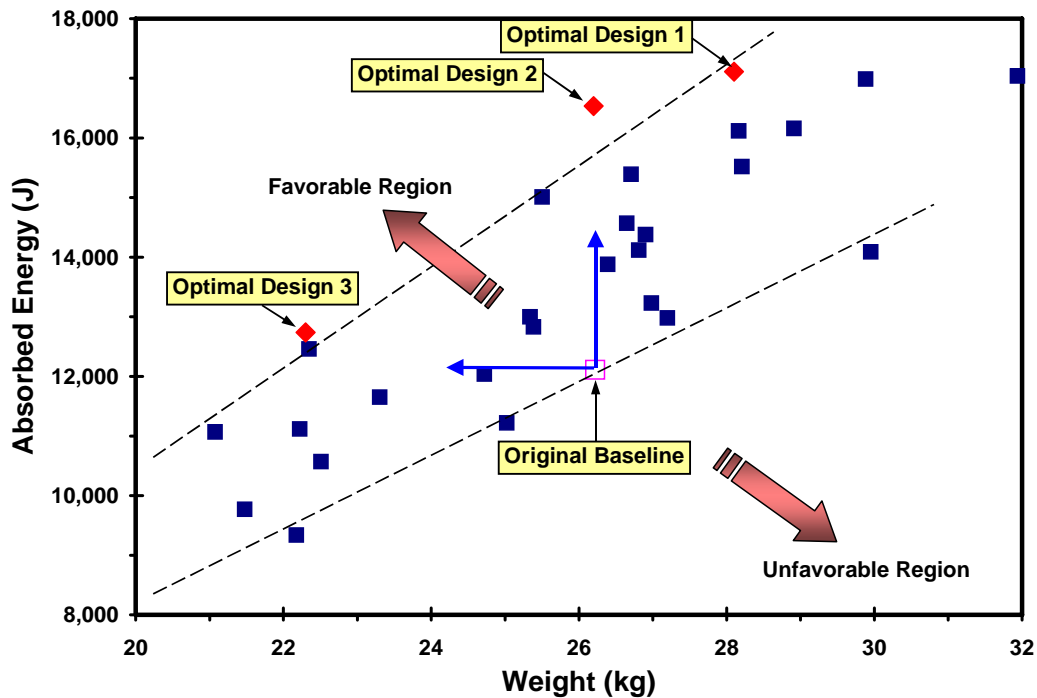


Figure 3.14 Relation Between Structural Weight and Energy Absorption

### 3.6 Full Vehicle Multidisciplinary Design Optimization

#### *3.6.1 Introduction*

Multidisciplinary Design Optimization (MDO) has evolved as a new discipline that provides a body of methods and techniques to assist engineers in moving engineering system design close to optimum. The key concept in several of these MDO methods is a decomposition of the design task into subtasks performed independently in each of the modules, and a system-level or coordination task giving rise to a two-level optimization. In general, decomposition is motivated by the obvious need to distribute work over many people and computers to compress the task calendar time. An application for MDO using the DOE/RSM methodology for exploring the design space and constructing highly nonlinear crash function is given in this section. MDO of a full

vehicle under the consideration of crashworthiness, Noise, Vibration, and Harshness (NVH), durability, and other performance attributes is one of the imperative goals for automotive industry. However, it is often infeasible due to the lack of computational resources, robust simulation capabilities, and efficient optimization methodologies. This research demonstrates that with high performance computing, a conventionally intractable real world full vehicle multidisciplinary optimization problem considering all performance attributes with large number of design variables become feasible.

Vehicle safety design is one of the major attributes in car product development. The vehicle structure must be designed to absorb enough crash energy through structural deformation and attenuate the impact force to a tolerable level when crash events occur. In the real world, all crash modes need to be considered simultaneously for crash analysis and optimization. Figure 3.15 shows the finite element models for full frontal impact, roof crush, 50% frontal offset impact, side impact, and NVH. The nonlinear explicit code RADIOSS and Nastran are used for the crashworthiness and frequency analyses, respectively.

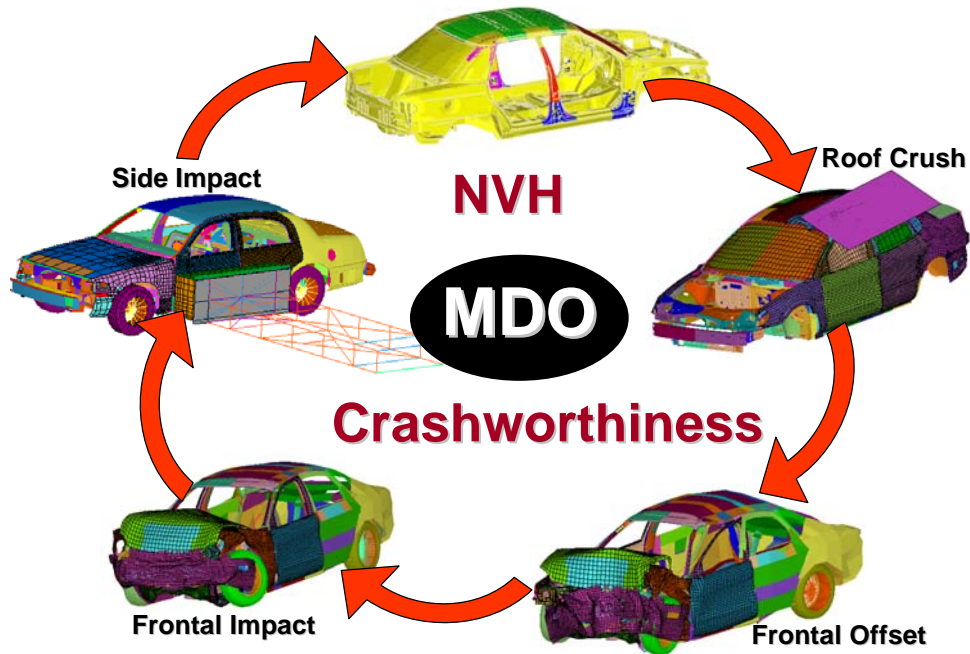


Figure 3.15 NVH and Crashworthiness Finite Element Models for Multidisciplinary Design Optimization

### 3.6.2 MDO Problem Formulation

The MDO problem is to minimize the total vehicle weight subjected to design constraints of NVH and safety crash modes:

Minimize: Weight

Subject to:

NVH Constraints:

$$27.3\text{Hz} \leq f_3 \leq 29.3\text{Hz}$$

$$\text{Static torsion} \leq D_t$$

$$\text{Static bending} \leq D_b$$

where  $f_3 = 3^{\text{rd}}$  frequency

$D_r$ =local displacement=3.4mm

$D_b$ =local displacement=0.9mm

Roof Crush Constraints:

Crush distance (D)  $\leq 5''$

Critical peak load ( $P_{cr}$ )  $\geq 27$ kN

Full Frontal Impact Constraints:

HIC  $\leq 450$

Chest G  $\leq 45$  g

$P_{total} \leq 10\%$  (i.e. 5-star NCAP rating)

where

$P_{total}$ =Total probability of severe injury= $1 - (1 - P_{head})(1 - P_{chest})$

$$P_{head} = \frac{1}{1 + e^{(5.02 - 0.0035 HIC)}}$$

$$P_{chest} = \frac{1}{1 + e^{(5.55 - 0.0693 ChestG)}}$$

50% Frontal Offset Crash Constraints:

Toe board intrusion  $\leq 10''$

Side Impact Constraints:

Viscous Criterion V\*C  $\leq 0.54$

Displacement  $\leq 27.2$  mm

There are 10 global (system) thickness design variables in the MDO problem including windshield, roof panel, roof rail, roof cross members and pillars. The total number of design variables for the NVH model is 19, including 10 for backlite glasses

and sheet metal thickness, 9 for the stiffness of connection between the backlite glass and structures. The thickness design variables contain floor panels, jacking/towing on quarter panel, backlite glass, shotgun and radiator support. There are 5 subsystem thickness design variables for full frontal and 50% frontal offset crash models, namely rails and subframe. As for the roof crush, 3 thickness and 7 material yield stress local design variables are taken into account for consideration. The MDO data flow is illustrated in Figure 3.16.

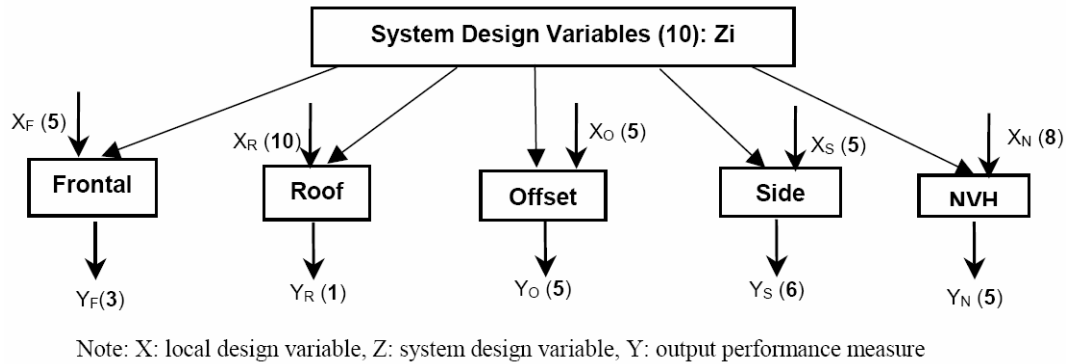


Figure 3.16 Multidisciplinary Design Optimization Data Flow

### 3.6.3 MDO Procedure

This research employs a DOE/RSM method to construct the approximation models for crash performance functions. Among the various methods for DOE and RSM, the optimal Latin Hypercube sampling method is employed to explore the design space uniformly to capture the nonlinear behavior of crash functions, while the stepwise regression method is used to construct the nonlinear response surfaces based on the computer experimental points. The NVH responses are approximated by the conservative Taylor Series Approximation (TSA) as:

$$a_k(x) = f(x_k) + \sum_{i=1}^n g_i(x_k)(x^i - x_k^i)\phi_i(x^i - x_k^i) \quad 3.55$$

where

$$\phi_i(x^i, x_k^i) = \begin{cases} 1 & \text{if } x_k^i g_i(x_k) \geq 0 \\ x_k^i / x^i & \text{otherwise} \end{cases} \quad 3.56$$

where  $a_k(x)$  is the approximate function at step  $k$ ,  $f(x)$  is the exact function,  $g_i$  is a partial derivative of  $f$  with respect to the  $i^{th}$  design variable.

Two optimization strategies are employed to perform the inner loop within the MDO process. The first takes advantage of the design sensitivity analysis capability in MSC.NASTRAN and the second takes advantage of both the sensitivity and the optimization capability. In the first strategy, the NVH sensitivities are extracted from the MSC.NASTRAN output and approximations are constructed using TSA. In addition to the three crash mode responses approximated by the quadratic order of stepwise regression, the MDO problem is solved by an SQP optimizer. As the NVH model is more efficient to run in this case, the NVH design variables are updated and the analysis is repeated in MCS.NASTRAN for three times while keeping the crash approximation models unchanged. After three NVH inner loops, all design variables are updated and reflected on the NVH and crash models. Simulations are then performed to validate the results from the first MDO cycle. The crash approximation models are updated and then continue to perform the next MDO cycle if necessary. The

move limits of the design variables for NVH approximation using the TSA are selected to be 20%.

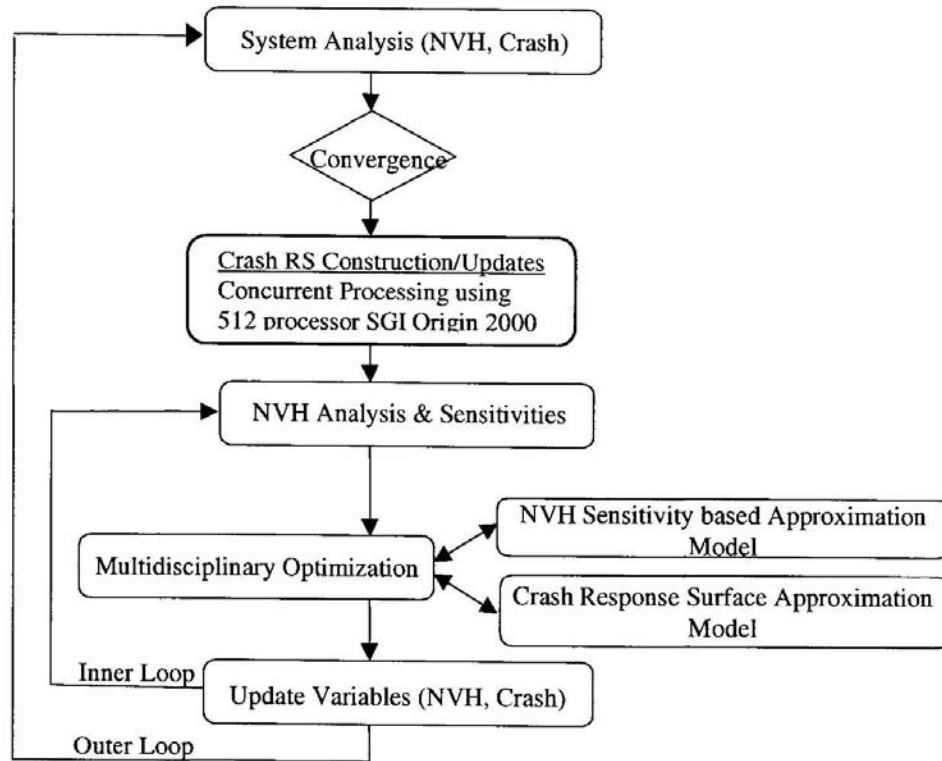


Figure 3.17 Multidisciplinary Design Optimization Flow Chart

The second strategy for the inner loop optimization is to take advantage of the design optimization capabilities in MSC.NASTRAN. Instead of exporting the NVH sensitivities and performing inner optimization loop manually for three iterations, the optimization process for each MDO cycle is completed entirely in the MSC.NASTRAN by imposing the crash performance constraints using the DEQATN and DRESP2 cards for the explicit crash equations provided from the stepwise regression approximations. The advantage of this strategy is that the inner loop can be completed without any hum

intervention. However, the approximate crash functions needs to be provided explicitly. The MDO flow chart is shown in Figure 3.17.

#### *3.6.4 MDO Numerical Results*

The design histories for the two strategies are summarized in Table 3.10. Note that the initial design starts from an infeasible region where the constraints of the third mode frequency, torsion and bending displacements, HIC and toe-board intrusion are all violated. After two MDO cycles, all constraints are satisfied and it is shown that two MDO strategies yield comparable results. The total vehicle weight is reduced by 14.8 kg and 15.6 kg, respectively. The objective and the maximum constraint histories are shown in Figure 3.18. The DOE results for frontal crash ( $P_{total}$  vs. weight) and offset crash (maximum intrusion vs. weight) are shown in Figure 3.19 and 3.20, respectively. It is observed that significant design improvements for both strategies are achieved, after two complete cycles. In frontal crash, the  $P_{total}$  is improved from 10% to 8.0% and 7.5%, respectively. While in the offset crash, the maximum toe-board intrusion is successfully controlled within 10 inches, while reducing vehicle weight. The roof crush performance constraint is insignificant as all designs are feasible before and after the optimization process. All NVH targets are also met, i.e. improving the torsion and bending stiffness by 10% and increasing the third mode frequency by 5%.

In brief, this example has successfully demonstrated the feasibility of using the DOE/RSM methodology for the multidisciplinary design optimization problem. The results showed that the methodology could substantially reduce the design cycle time



and vehicle weight in the development and certification of new vehicle designs while satisfying the functionality requirements.

Table 3.10 Design History for Multidisciplinary Design Optimization

Attribute	Performance	Baseline	Target	Original*		Alternative**	
				Cycle 1	Cycle 2	Cycle 1	Cycle 2
NVH	3 <sup>rd</sup> frequency (Hz)	26.5	$27.8 \leq f_3 \leq 29.3$	29.3	29.3	27.8	27.8
	Torsion disp. 1 (mm)	3.8	$\leq 3.4$	3.4	3.4	3.4	3.4
	Torsion disp. 2 (mm)	-3.8	$\geq -3.4$	-3.4	-3.4	-3.4	-3.4
	Bending disp. (mm)	-0.97	$\geq -0.9$	-0.9	-0.87	-0.9	-0.9
Frontal	HIC	500	$\leq 450$	356	411	411	357
	Chest G	42	$\leq 45$	38	39	42	39
	P <sub>total</sub> (%)	10	$\leq 10$	7.3	8.0	9.2	7.5
Roof	Resistance force (kN)	34.7	$\geq 27$	30.5	31.2	31.4	31.3
Offset	Intrusion 1 (in.)	11.2	$\leq 10$	9.7	9.9	10	9.9
	Intrusion 2 (in.)	10.8	$\leq 10$	9.4	10	9.7	9.8
	Intrusion 3 (in.)	10.9	$\leq 10$	9.4	10	10	9.8
	Intrusion 4 (in.)	10.1	$\leq 10$	8.9	9.4	9.5	9.4
	Intrusion 5 (in.)	10.5	$\leq 10$	9.3	9.8	9.9	9.6
<b>Weight (Kg)</b>		<b>1740.5</b>	<b>Minimize</b>	<b>1726.6</b>	<b>1725.7</b>	<b>1727.2</b>	<b>1724.9</b>

\* 3 iterations for NVH loop

\*\* 5 iterations for NVH loop in NASTRAN

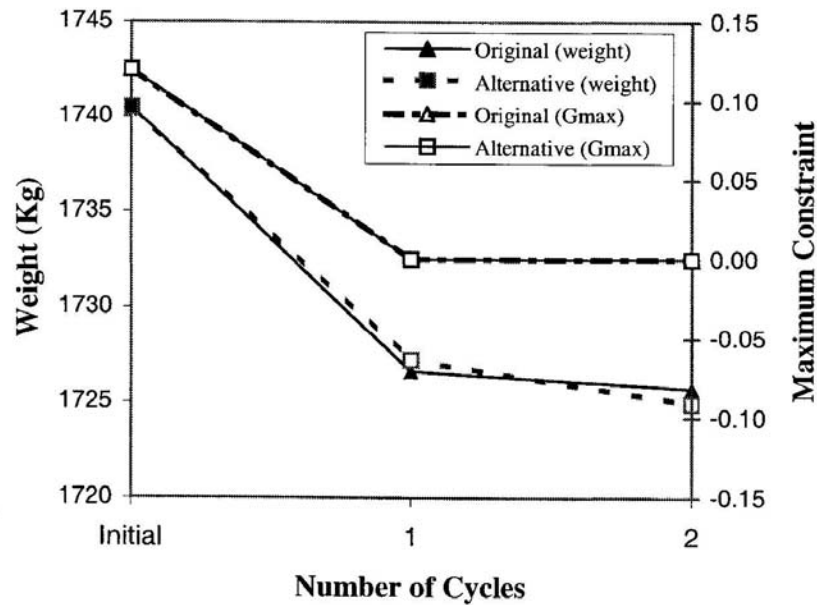


Figure 3.18 Objective and Constraint Design History for Multidisciplinary Design Optimization

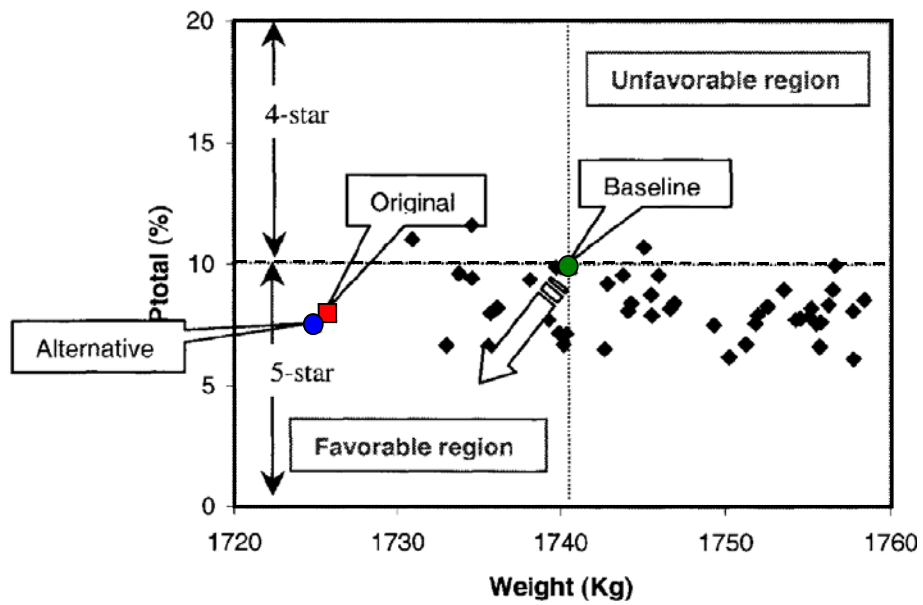


Figure 3.19 DOE Matrix for Frontal Crash ( $P_{total}$  vs. Weight)

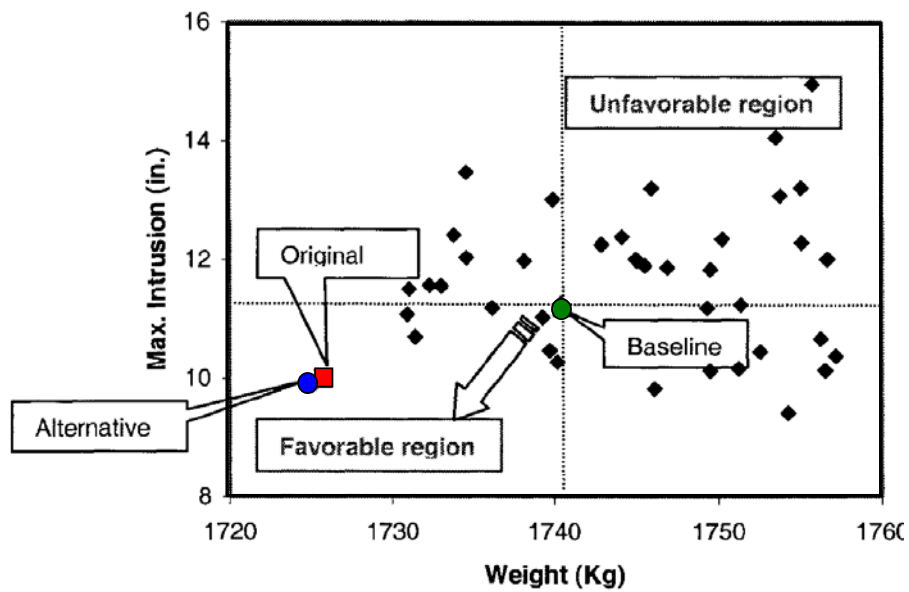


Figure 3.20 DOE Matrix for Offset Crash (Maximum Intrusion vs. Weight)

### 3.7 Conclusions

The use of surrogate models or metamodeling has lead to new areas of research in simulation –based design optimization. The Surrogate model based optimization method offers advantages over traditional gradient-based direct optimization techniques, especially when dealing with the noisy responses and/or high computational cost characteristics of computer simulations.

The space filling DOE methods (LHS, UD, Halton Sequence, Sobol Sequence, Faure Sequence) and metamodeling techniques (polynomial regression, stepwise regression, kriging, moving least square, radial basis function, adaptive and interactive modeling system, multivariate adaptive regression splines) are reviewed in this Chapter. A comparative study for a full vehicle frontal impact is presented using five metamodeling techniques. It is shown that the MQ function outperforms other metamodeling techniques for HIC and toe-board intrusion crash functions. A vehicle front rail optimization problem is given to improve the structural energy absorption efficiency by using the DOE/RSM based optimization method. Finally, the DOE/RSM method is demonstrated on a Multidisciplinary Design Optimization problem for a full vehicle model considering the NVH and crashworthiness design requirements.

## CHAPTER 4

### SEQUENTIAL REGULARIZED MULTIQUADRIC AND OUTPUT SPACE MAPPING

#### 4.1 Introduction

In recent years, response surface methodology (RSM) has become a popular tool for design optimization of large-scale problems required extensive computational time. In addition, RSM provides an overall perspective of system response within the design space and simplifies the process of integrating different mathematical models. Traditional RSM (Myers and Montgomery, 1995) [64] is a global approach that uses polynomials to approximate the objective and constraint responses for optimization process. The coefficients of the polynomial models are computed using the least square regression method. The computed response surface model is the “best fit” polynomial function from the available data.

In general, the fitted function does not interpolate the available data. In 1971, Hardy proposed the use of multiquadratic (MQ) function for interpolation [37]. Multiquadric function was originally used to approximate geographical surfaces and gravitational and magnetic anomalies. Recently, MQ response surface has been used for design optimization applications. Essentially MQ response surface models are multidimensional interpolation functions. One basis function is chosen for each data

point (hence MQ is a special case of approximations that use radial basis functions). Thus MQ models are very flexible; they can be built with limited available data.

Hardy's work was largely unknown to mathematicians until the publication of Franke's review paper (Franke, 1982) [30]. Franke reviewed many methods and concluded that, "*in terms of fitting ability and visual smoothness the most impressive in the tests is the Multiquadric method, due to Hardy*". More recent review papers by McDonald *et al.* [59] and Jin *et al.* [40] have indicated that MQ can also be used as a basis for constructing multivariate response surface models. However, despite MQ's excellent performance, it contains a parameter, often referred to as the shift (or smooth or shape parameter), whose choice can greatly affect the accuracy and performance of the approximation. By adjusting the shift parameter, the accuracy of the approximation can be considerably improved. It has been found by Kansa [44] that by increasing the shift parameter, the root mean square (RMS) error of the fit dropped to a minimum and then grew rapidly thereafter. Thus there exists an optimal shift parameter that will yield minimum RMS for the fitted function. Methods for computing the optimal shift parameter have been reported by Wang [88, 89], so as to take the most advantage of the excellent performance of the MQ approximation.

In search for better basis functions for approximation, many mathematicians have proposed the use of radial basis function for multivariate interpolation of scattered data [15]. Radial basis function approximation schemes have also been linked to neural network by Girosi *et al* [33]. In that work, Tikhonov's regularization theory [86] is combined with RBF to produce more robust approximation than RBF alone. It is noted

that regularization network has also been related to support vector machines (SVM) in a recent paper by Evgeniou *et al* [25]. A recent study shows that the performance of SVM regression is similar to the best-tuned Artificial Neural Network (ANN).

#### 4.2 Regularized Multiquadric

Radial basis functions (RBF) have extensively been used for interpolation regression due to their universal approximation properties and simple parameter estimation. In 1988, Broomhead and Lowe [14] introduced the RBF networks into the neural network literature. This is because in applications where one has to deal with many thousands of noisy data points, an approximate solution to the data is more desirable than an interpolate one. Broomhead and Lowe proposed to reduce the number of basis functions in order to reduce the computational complexity. The RBF network has widely been used in many machine learning applications such as the regularized radial basis function network (RRBFN) and support vector machines (SVM). Given the following data base  $(\mathbf{x}_i, \mathbf{y}_i), i=1$  to  $N$ , the approximation of the RBF takes form:

$$y(\mathbf{x}) = \sum_{i=1}^N C_i \phi_i(\mathbf{x}, \mathbf{x}_i) \quad 4.1$$

where  $\mathbf{x}_i$  is the  $i^{th}$  input vector,  $N$  is number of training data,  $\mathbf{x}$  is the coordinates of evaluation points. Any radial symmetric radial basis function (RBF) can be chosen as a basis in Equation 4.1. In this research, we propose to use the Multiquadric (MQ) radial basis function:

$$\phi_i = \sqrt{\mathbf{r}_i^2 + h} \quad 4.2$$

Note that in the foregoing equation,  $r^2 = \|\mathbf{x} - \mathbf{x}_i\|^2$ , and  $h$  is known as the shift or smooth parameter. The value of shift parameter  $h$ , controls the curvature of the multiquadric approximate functions, is generally chosen as smaller than the average spacing of the sampling points. The estimation of the value of the shift parameter is crucial, several researchers [1, 78] have proposed to use the bootstrapping techniques, which are normally used in statistics for accuracy estimation, and are related to Monte Carlo methods, to estimate the shift parameter in a quasi-optimal way. The basic idea of the approach is to resample a relatively small set of data to increase its statistical significance. In this case, the cross-validation or so-called ‘leave-one-out’ technique can be employed to obtain the associated characteristic interpolation error between the true function and MQ approximate function. Namely, compute the cross-validation root mean square (CVRMS) error to assess model accuracy by removing each sample point used to fit the model one at a time from the data set, rebuilding the model without the sample point, and computing the difference between the predicted value and actual value at the sample point:

$$CVRMS = \sqrt{\frac{\sum_{i=1}^N (y_i - \hat{y}_i)^2}{N}}$$

where  $N$  is the number of sample points,  $y_i$  is the point currently not in the data set, and  $\hat{y}_i$  is the predicted value.

The unknown interpolation coefficients  $C_i$  can be determined by minimizing the  $L_2$  norm

$$J = \left[ \mathbf{f}_i - \sum_{j=1}^N \mathbf{C}_j \phi(\mathbf{x}_i - \mathbf{x}_j) \right]^2 \quad 4.3$$

or in matrix form as:

$$\mathbf{A}\mathbf{C} = \mathbf{f} \quad 4.4$$

where

$$\mathbf{A} = \|\mathbf{x}_i - \mathbf{x}_j\| \quad 4.5$$

$$\mathbf{C}^T = \{C_1, C_2, \dots, C_N\} \quad 4.6$$

$$\mathbf{f}^T = \{f_1, f_2, \dots, f_N\} \quad 4.7$$

Note that the matrix  $\mathbf{A}$  is always invertible, provided that the data are not redundant. However, in the situation where the matrix  $\mathbf{A}$  is singular, the regularization theory in the RRBFN can be used to resolve the ill-posed problem. The basic idea of regularization, in the multi-dimensional hyper-surface reconstruction problem, is to stabilize a solution by means of some auxiliary nonnegative functional using prior information of the solution as system information. In RRBFN, the weights  $C_i$  are trained by solving the following constrained minimization problem. Namely:

Find  $c$  to minimize

$$f = \frac{1}{2} \boldsymbol{\varepsilon}^T \boldsymbol{\varepsilon} + \frac{1}{2} \mathbf{r} \mathbf{C}^T \mathbf{C} \quad 4.8$$

Subject to the constraint

$$\boldsymbol{\varepsilon} = \mathbf{A}\mathbf{C} - \mathbf{Y} \quad 4.9$$



where  $\boldsymbol{\varepsilon}$  is the error vector and  $\mathbf{Y}$  is the known data. The elements of matrix  $\mathbf{A}$  take the form  $A_{ji} = \phi(x_j, x_i)$ . The solution of this problem can be obtained by Lagrange Multiplier method. That is:

$$\mathbf{C} = (\mathbf{A}^T \mathbf{A} + r \mathbf{I})^{-1} \mathbf{A}^T \mathbf{Y} \quad 4.10$$

where  $r$  is the so-called regularization parameter. A direct mathematical derivation of Equation 4.10 is provided in Appendix A. Note that the foregoing approach leads to interpolation when  $r$  approaches to zero.

In modern machine learning terminology, the first term of Equation 4.8 is known as the empirical error (or standard error) and the second term is known as the structural error. The empirical error controls the closeness (minimum of mean square error) of the trained data while the structural error controls the smoothness of the functions. Thus, in RRBFN, the network is trained to balance between the empirical error and structural risk. Note that for given  $h, r$ , the training is the solution of a system of equations. It should be noted that the approach is essentially the regression by least square using Tikhonov's regularization theory. Regularization theory provides a mathematical framework, which allows estimating of the optimal weights and smoothing of the function encoded in the radial basis function network to be controlled via the regularization term (or structural error). It has been found through numerical experiments that even with a very small regularization parameter  $r$ , the proposed approach produces a much smoother (i.e. smaller coefficients  $c$ ) function than a strict interpolation approach with no adverse effect on the accuracy.

For the MQ function, it is well known in the literature that the parameter  $h$  has a large effect on the performance of the RBF approximation. An efficient method to optimize the smooth parameter  $h$  for MQ interpolation model has been developed by Wang [88, 89].

#### 4.3 Proposed Algorithms for Crashworthiness Optimization

Two effective simulation-based optimization algorithms that can be used to solve for design optimization of large-scale, computationally expensive systems are developed and studied in this dissertation. The solution approach for crashworthiness design optimization is described in the following.

##### *4.3.1 Sequential Regularized Multiquadric (SRMQ)*

In this proposed method, the initial response surface model is constructed using the Regularized Multiquadric (RMQ) approximation based upon simulation results at a set of the sampling points that has the uniform-space filling property. In the implementation of this dissertation, we select the quasi Monte-Carlo Sampling (QMC) using the Halton Sequence. Note that other space-filling methods such as LHS, Sobol Sequence, Faure Sequence etc. can also be applied to determine the uniform distributed sampling points. The regression analysis is then performed on the objective and constraint responses to generate the RMQ models. The nonlinear optimization process is performed based on the approximate functions using a Sequential Quadratic Programming (SQP) algorithm to obtain a predicted optimal design satisfied the constraint requirements. The crash finite element analysis (e.g. LS-DYNA) is evaluated at the predicted design to validate the response attributes (such as structural weight,

internal energy etc.). The convergence tolerance is checked for each of the design iterations. The DOE matrix is augmented by design points obtained in the optimization process. The process is repeated sequentially until the solution converges. Figure 4.1 shows the flow chart of the SRMQ optimization algorithm.

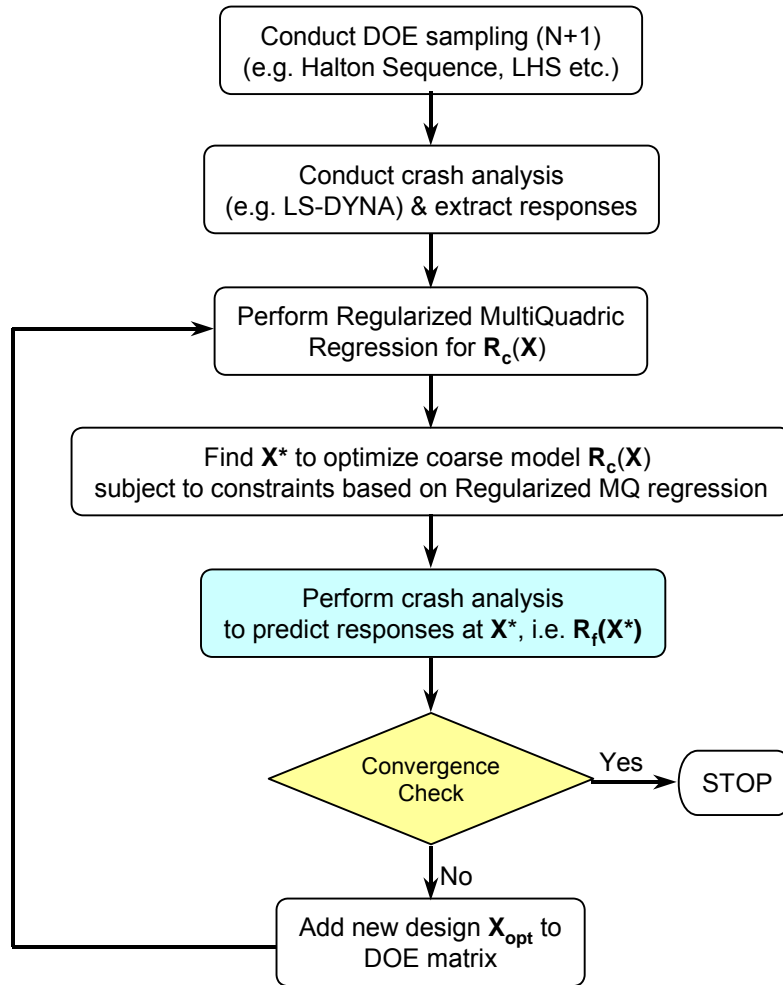


Figure 4.1 Flow Chart for SRMQ Optimization Algorithm

#### 4.3.2 Sequential Regularized Multiquadric with Output Space Mapping

The Sequential Regularized Multiquadric with Output Space Mapping (SRMQ/OSM) algorithm contains two procedures that are repeated iteratively to solve for the design problem. The first procedure is exactly same as the one described in the foregoing SRMQ algorithm. After performing the SRMQ, an Output Space Mapping (OSM) is performed to fine-tune the approximate RMQ functions. The basic concept of OSM is based on the residual misalignment when approaching to the optimal design. The OSM aims at establishing a mapping  $\mathbf{O}$  between the output mapped surrogate response  $\mathbf{R}_o$  and the RMQ model  $\mathbf{R}_c$ . The mapping can be expressed in the following form as:

$$\mathbf{R}_o = \mathbf{R}_c(\mathbf{X}) + \Delta\epsilon \quad 4.11$$

where

$$\Delta\epsilon = \mathbf{R}_f(\mathbf{X}^*) - \mathbf{R}_c(\mathbf{X}^*) \quad 4.12$$

$\Delta\epsilon$  is the residual between the RMQ and finite element validation responses at the predicted optimal design  $\mathbf{X}^*$  obtained in the SRMQ procedure. The optimization process is then performed again on the ‘calibrated’ approximate functions, namely:

$$\mathbf{X}_{opt} = \arg\left\{\min_{\mathbf{X}_{opt}} \mathbf{O}(\mathbf{R}_c(\mathbf{X}))\right\} \quad 4.13$$

The convergence tolerance is checked in each of the iterations. The DOE matrix is augmented by the designs obtained in both steps. The process is repeated sequentially until the solution converges. Figure 4.2 shows the flow chart of the proposed SRMQ/OSM optimization algorithm.

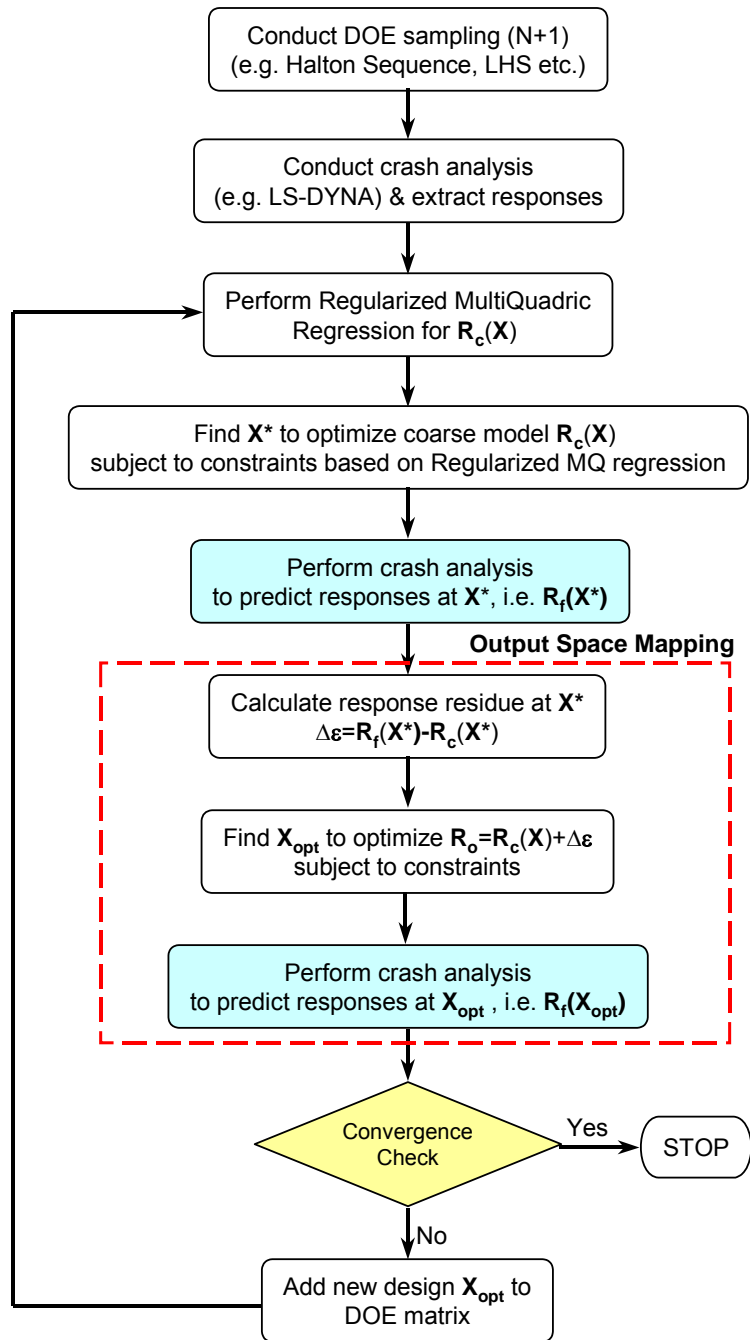


Figure 4.2 Flow Chart for SRMQ/OSM Optimization Algorithm

## 4.4 Numerical Examples

### *4.4.1 One Dimensional Function*

Without loss of generality, an unconstrained optimization problem is presented in this section using the proposed SRMQ and SRMQ/OSM methods to find the optimal solution of an one-dimensional nonlinear function. The optimization problem is:

Find  $x$  to:

Minimize:  $y = -2 - (x \sin x)^2$

Side constraints:  $0 \leq x \leq 6$

The optimal design found by the direct gradient-based optimization method is  $x^* = 4.9132$ , and the corresponding function value is  $y_{\min} = -25.179$ . The values are used as the exact solution to compared with the proposed methods. Figure 4.3 shows the design history of the SRMQ/OSM method. The sequential optimization process starts with a linear function by selecting two ( $N+1$ ,  $N$ =number of design variables=1) DOE sampling points at  $x = 0.5, 5.5$  (as shown in Figure 4.3 (a) and are represented by green square dot). For higher dimensional problems, the DOE sampling points can be generated by any “space-filling” DOE methods as discussed in Chapter 2. The regularized Multiquadric regression is used to generate an approximate function based upon these two sampling points initially. The Sequential Quadratic Programming (SQP) is used to find a predicted optimal design on the approximate function. The 1<sup>st</sup> iteration design is found to be at  $x^{(1)} = 6$  (upper bound), as shown in Figure 4.3(a). Note that the design is located on the boundary since the process starts with a linear

function. A validation evaluation,  $y^{(i)}$ , is then performed at this predicted optimal design and the convergence tolerance is subsequently checked. In the OSM process, a correction factor based upon the residual misalignment is evaluated at the predicted design  $x^{(i)}$  and is added to the approximate function to find the next predicted design in the Output Space Mapping (OSM) process. The predicted design  $(x^{(i)}, y^{(i)})$  is then added to the DOE and response matrices to update the approximate function. The process is repeated iteratively. Note that the predicted design found by the OSM method for this one-dimensional unconstrained example is same as the one found by the Sequential Regularized Multiquadric (SRMQ). Figures 4.3(b) to Figure 4.3(f) show the design history for iterations 2 to 6 respectively. It is observed that the predicted design quickly converges to the optimal design after 4 design iterations. Note that the RMQ approximate function is evolving from a linear function into a nonlinear function as the sequential optimization process proceeds by including the predicted optimal design.

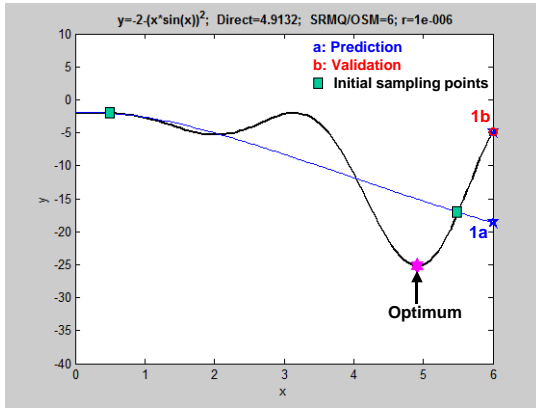
The original function contains two local minima. In order to test if the proposed SRMQ/OSM method is able to find the global optimum, we purposely select the initial DOE sampling points at  $x = 2, 4$  so that the optimization process starts from the lower bound in the second case study. Note that the predicted optimal design at the 1<sup>st</sup> iteration is at  $x^{(1)} = 0$ , which is separated by a local minimum (around  $x=2$ ) as shown in Figure 4.4(a). In the 2<sup>nd</sup> iteration, the predicted design found by the proposed method is able to “leap over” the local minimum and quickly converges to the global optimum after 4 design iterations. Note that the SQP algorithm to solve for the optimization

process is a local optimizer. Figure 4.4(e) shows the design history after seven design iterations.

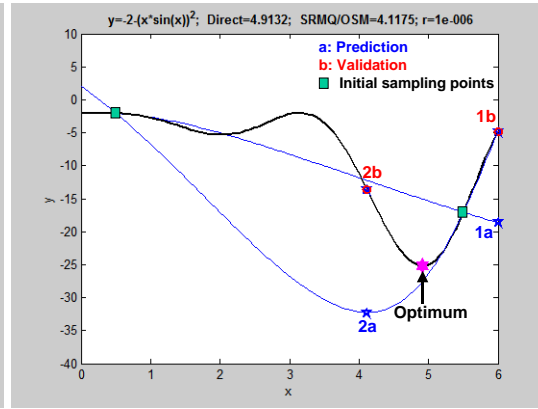
Based on the numerical study of the two cases, it is shown that the proposed SRMQ/OSM method indeed is able to find the global optimum using a fairly small number of function evaluations. It is noted that the solution obtained by SRMQ/OSM and SRMQ is the same for this unconstrained problem since the objective function is simply sifted by a constant calculated from the misaligned residue in each of the design iterations. The effect of OSM can be shown for the constrained optimization problems. Figure 4.5 shows the correction factor (or residual error) for these two cases. In both cases, the correction factor is reduced rapidly after four design iterations, indicated the solution also converges quickly accordingly.

Our numerical experiment also indicates that the SRMQ/OSM solution will be ‘stranded’ on the lower bound or upper bound of the design domain if all the initial  $N+1$  sampling points are located at the boundary (i.e.  $x = 0, 6$  for this example). This is because the initial RMQ function has zero a correction factor on the design domain boundary. In this situation, shifting the sampling points away from the boundary or adding additional initial sampling points will resolve the issue.

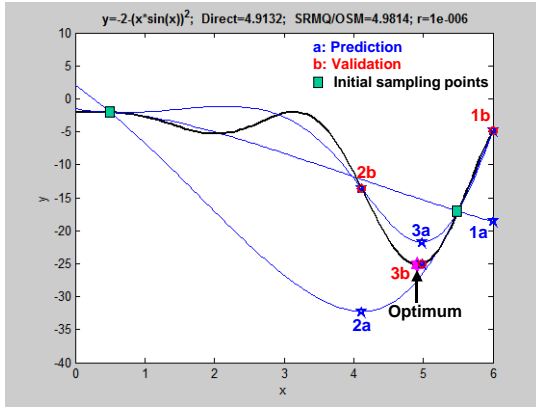




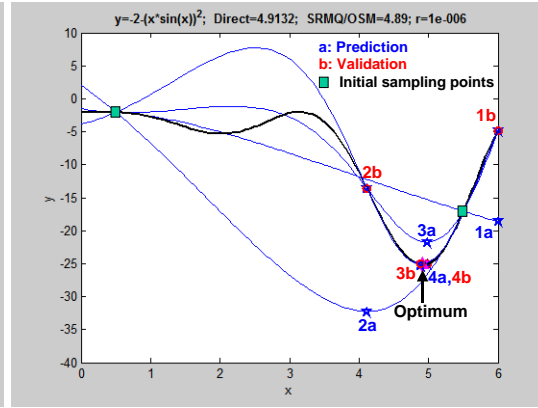
(a)



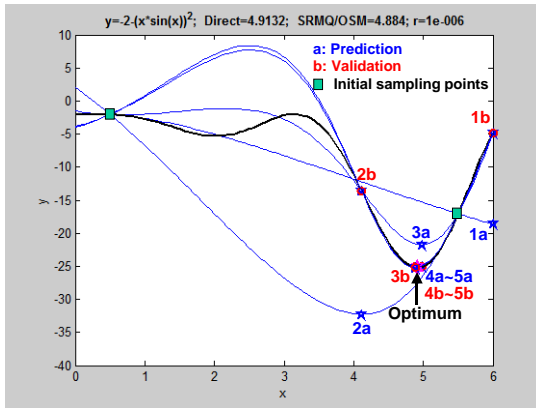
(b)



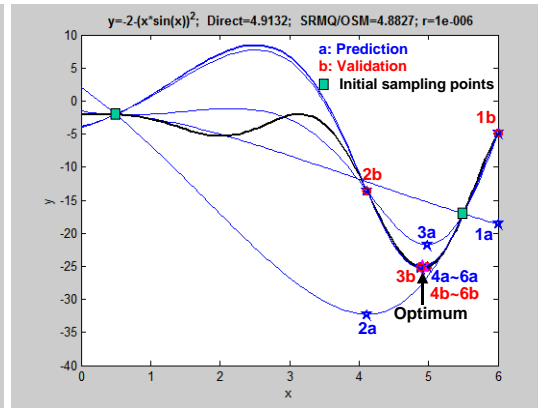
(c)



(d)

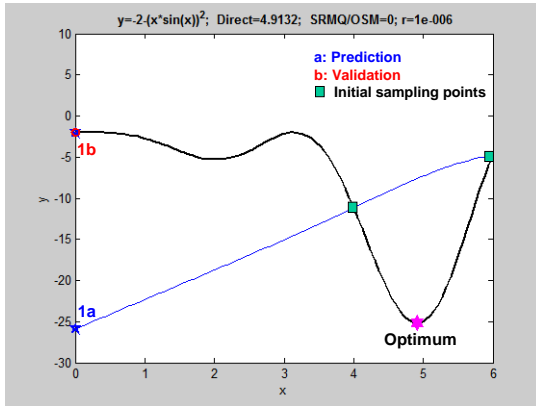


(e)

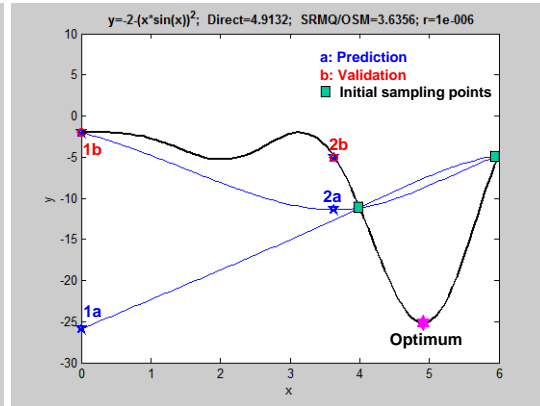


(f)

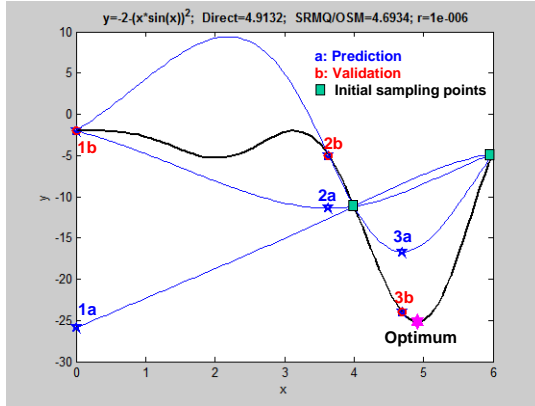
Figure 4.3 One Dimensional Problem Using SRMQ/OSM Optimization Algorithm (Sampling Points:  $x = 0.5, 1.5$ ): (a) 1<sup>st</sup> Iteration, (b) 2<sup>nd</sup> Iteration, (c) 3<sup>rd</sup> Iteration, (d) 4<sup>th</sup> Iteration, (e) 5<sup>th</sup> Iteration, (f) 6<sup>th</sup> Iteration



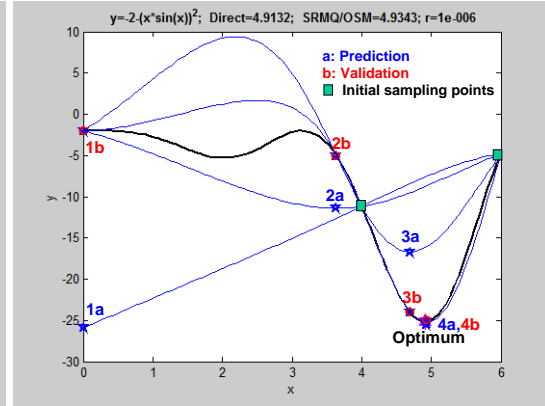
(a)



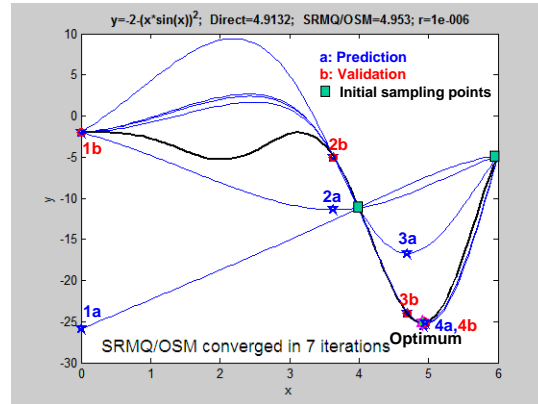
(b)



(c)



(d)



(e)

Figure 4.4 One Dimensional Problem Using SRMQ/OSM Optimization Algorithm (Sampling Points:  $x = 4, 6$ ): (a) 1<sup>st</sup> Iteration, (b) 2<sup>nd</sup> Iteration, (c) 3<sup>rd</sup> Iteration, (d) 4<sup>th</sup> Iteration, (e) 7<sup>th</sup> Iteration

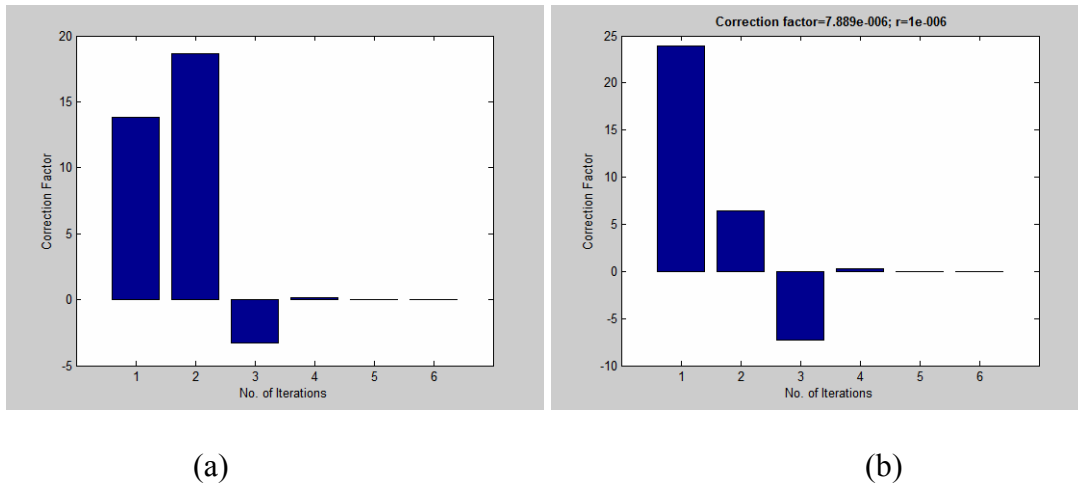


Figure 4.5 Correction Factor for One Dimensional Problem Using SRMQ/OSM Optimization Algorithm: (a)  $x = 0.5, 1.5$ , (b)  $x = 4, 6$

Table 4.1 Parametric Study for Prediction Error using Different Regularization Parameter  $r$

$r$	$\log(r)$	$X_{\text{opt}}$	$Y$	Abs. Error %
1.0E-06	-6.0	4.9529	-25.139	0.158
5.0E-06	-5.3	4.9497	-25.146	0.133
1.0E-05	-5.0	4.9425	-25.157	0.086
5.0E-05	-4.3	4.9065	-25.178	0.004
1.0E-04	-4.0	4.8944	-25.170	0.035
1.0E-03	-3.0	4.8823	-25.155	0.095
<b>Exact:</b>		<b>4.9132</b>	<b>-25.179</b>	N/A

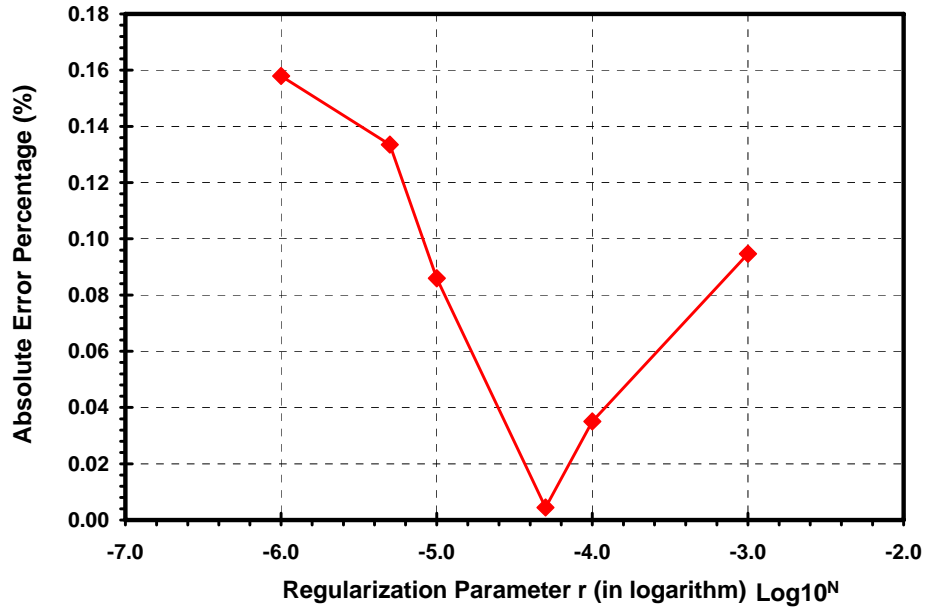


Figure 4.6 Logarithm Regularized Parameter vs. Absolute Error Percentage

It is shown in Equation 4.8 that the structural error contains a regularization parameter  $r$ . This value needs to be selected properly since it controls the smoothness of the multiquadric radial basis function to be used in the optimization process. To better understand the numerical behavior, we conduct a parametric study by selecting a set of regularization parameters and studying the error between the exact and predicted values. Table 4.1 and Figure 4.6 show the predicted error percentage with different regularization parameters  $r$ . Note that the x-axis of the regularization parameter in Figure 4.6 is in logarithm scale. It is shown that the absolute error percentage tends to reduce and then increase thereafter as  $r$  is decreasing. It is obvious that an optimal regularization parameter exists which controls the smoothness and accuracy of the predicted function. Note that as  $r$  is approaching to zero, the regularized term becomes very small and the approach leads to interpolation. In the situation where too many

close sampling points are selected in the optimization process, the interpolation becomes ill conditional and the numerical problem starts to emerge. A more systematic way of finding the optimal  $r$  is to perform the cross-validation by dividing the data into  $k$  subsets of approximately equal size. The regularized Multiquadric surrogate model is constructed  $k$  times, each time leaving out one of the subsets from training, and using the omitted subset to compute the error measure of interest, such as the mean square error. In most cases, a small positive (but not to be zero)  $r$  is preferable.

#### 4.4.2 Two Dimensional Function

The proposed SRMQ/OSM method is employed to solve a two-dimension problem of the nonlinear peak function as shown in Figure 4.7. The unconstrained optimization problem is:

Find  $(x, y)$  to:

$$\text{Minimize:} \quad z(x, y) = 3(1-x)^2 e^{-(x^2+(y+1)^2)} - 10\left(\frac{x}{5} - x^3 - y^5\right) e^{-(x^2+y^2)} - \frac{1}{3} e^{-((x+1)^2+y^2)}$$

$$\text{Side constraints:} \quad -3 \leq x \leq 3 \text{ and } -3 \leq y \leq 3$$

It is evidenced from the surface plot of Figure 4.7 that peak function contains two local minima. In order to investigate if the proposed method is able to find the global optimal design, the initial design is selected at a point that is close to the local minima (not the optimal design). The initial DOE sample data is selected to be linear as  $N+1$  ( $N=2$ ). Figures 4.8 and 4.9 show the contour plot of the design history for  $r=1 \times 10^{-3}$  and  $r=1 \times 10^{-6}$  respectively. Since the SRMQ starts with linear regression, the design for the first few design iterations (2 to 4) falls on the design domain boundary. For  $r=1 \times 10^{-3}$  as shown in Figure 4.7, the final design seems to be stranded at  $(0.9434, -1.9941)$ , whereas the exact optimal solution is  $(0.2283, -1.6255)$ . As  $r$  is reduced to  $1 \times 10^{-6}$ , a better solution to the optimal design is found at  $(0.3218, -1.6562)$ , as shown in Figure 4.9. When the sample data is increased to 4 (a better starting RMQ function), the solution tends to converge much faster (8 iterations as compared to 10 iterations for sample data of 3), as shown in Figure 4.10. The final solution  $(0.2281, -1.6677)$  falls even closer to the optimum. For all the 3 cases, the proposed

SRMQ/OSM method is able to “leap over” the local minima and tends to converge to the global optimal design.

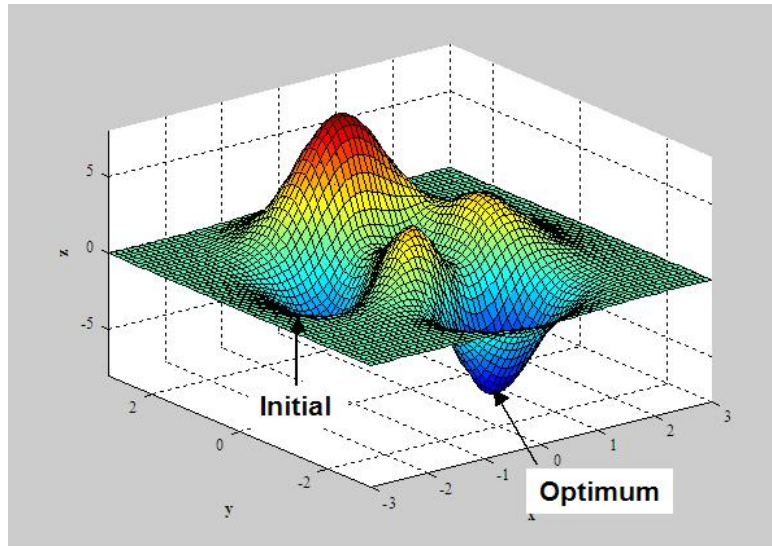


Figure 4.7 Surface Plot of the Two Dimensional Peak Function

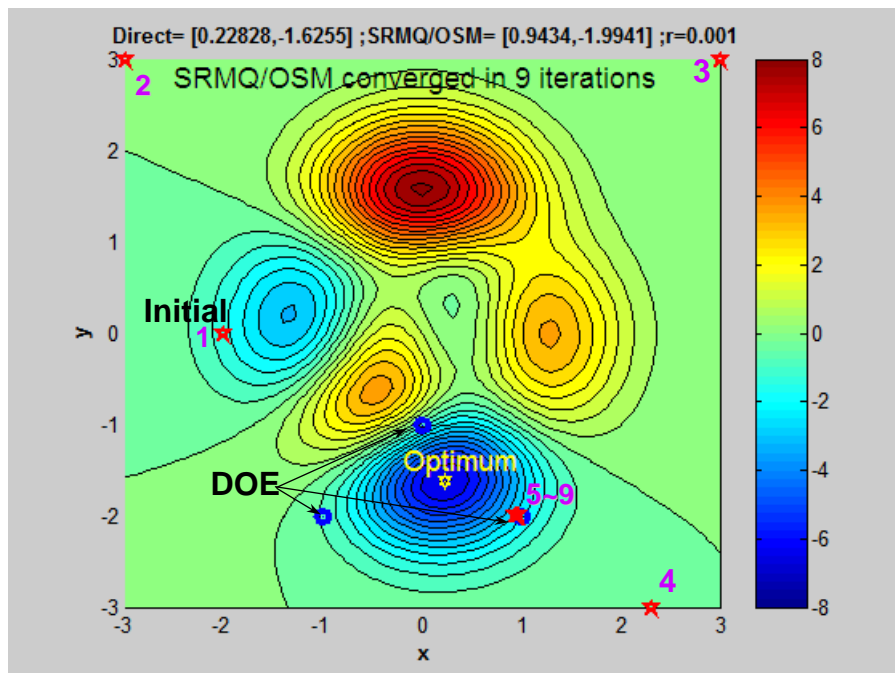


Figure 4.8 The Peak Function Using SRMQ/OSM (3 Sampling Points,  $r=1 \times 10^{-3}$ )

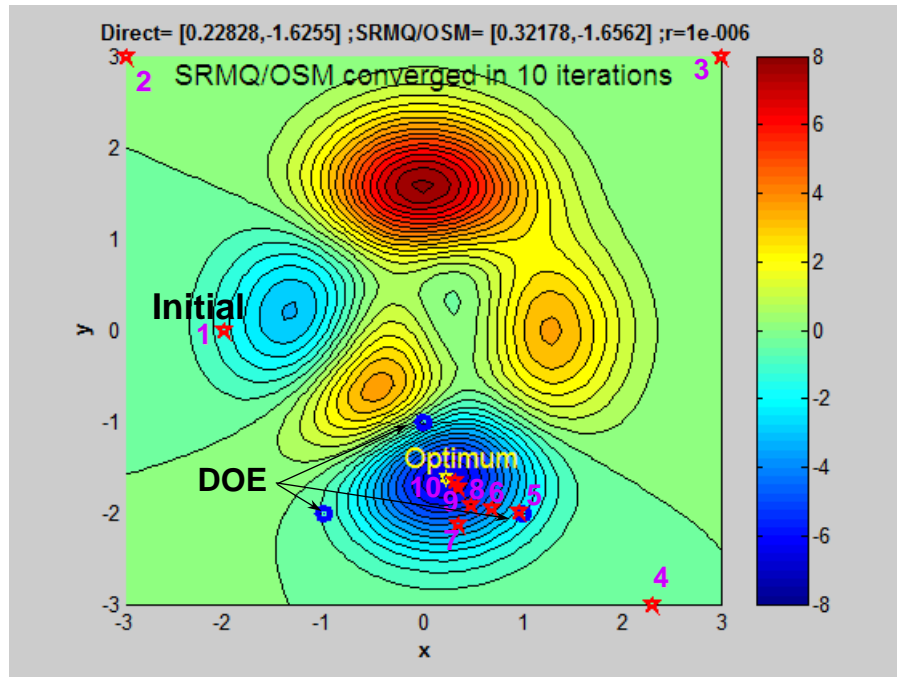


Figure 4.9 The Peak Function Using SRMQ/OSM (3 Sampling Points,  $r=1 \times 10^{-6}$ )

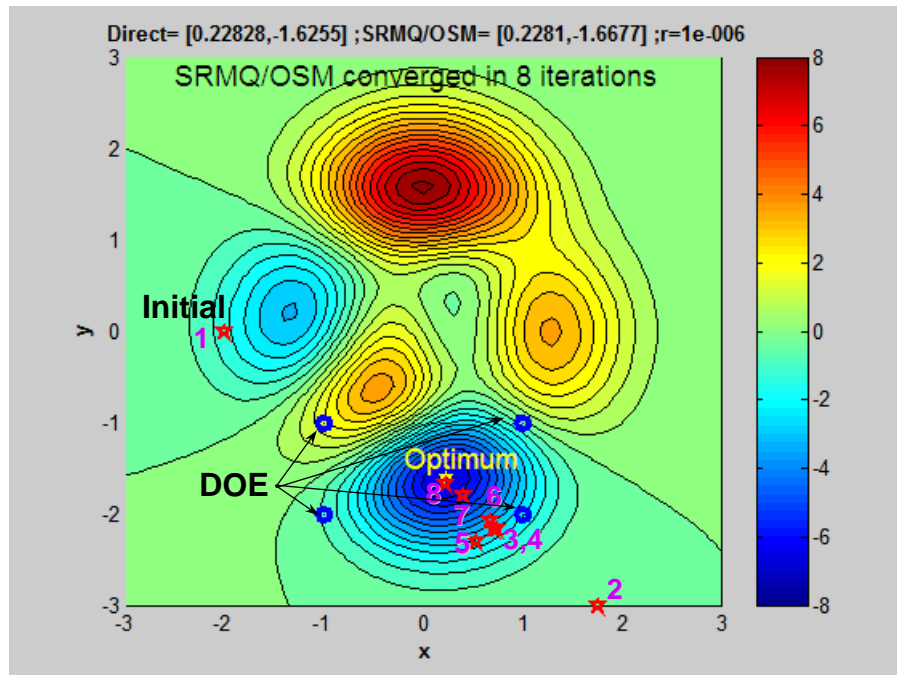


Figure 4.10 The Peak Function Using SRMQ/OSM (4 Sampling Points,  $r=1 \times 10^{-6}$ )



## 4.5 Rectangular Tube Crush Optimization Problem

### *4.5.1 Finite Element Model*

A rectangular tube crush model is developed using the explicit nonlinear finite element code, LS-DYNA, to demonstrate the Crashworthiness optimization using the proposed SRMQ and SRMQ/OSM algorithms as well as to compare with the gradient-based direct optimization technique. LS-DYNA is a general purposed nonlinear explicit finite element commercial code developed by the Livermore Software Technology Corporation (LSTC). Figure 4.11 shows the LS-DYNA model of the rectangular tube. The width, height and length of the tube are 110 mm, 90 mm and 460 mm, respectively. A 800 Kg rigid body moving at 20 mph is attached to each node of the rear end of the tube. The rectangular tube, along with lumped-mass rigid body, impacts onto a rigid wall barrier with an initial impact velocity. The master-slave contact algorithm is defined between the rectangular tube (serves as the slave part) and the wall (serves as master part). The self-contact algorithm is defined for each of the 4 parts of the rectangular tube to prevent the node from penetrating or intersecting each other after impact. The finite element model contains 3,197 shell elements and 3,261 nodes. The crush trigger or crush initiator modeling is included in the FE model to initiate the buckling load to avoid high initial peak load. The critical time step according to the critical element size for this model is 0.52  $\mu$ sec. The simulation time is selected to be 20 msec. The computational time is 5 minutes and 30 seconds running on an IBM Intellistation with 2.8 GHz speed using 1 CPU.

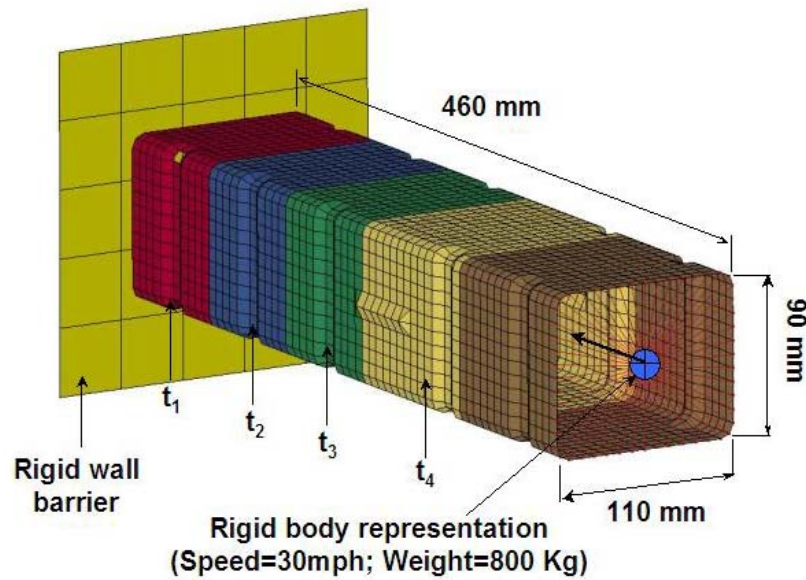


Figure 4.11 LS-DYNA Finite Element Model of the Rectangular Tube Crush Problem

#### 4.5.2 Problem Definition

The energy-absorbing mechanism of this rectangular tube is mainly the axial collapse mode. The main thrust of the design problem is to improve the impact performance by increasing the internal energy while reducing or maintaining the initial crush peak force and structural weight. Four thickness design variables are selected as shown in Figure 5. The optimization problem is formulated as:

Find the thickness design variable  $x_i$  ( $i=1\sim4$ ) to

Maximize: IE

Subject to:  $g_1: W \leq 3.1 \text{ kg}$

$g_2: IE_{2\text{ms}} \leq 850 \text{ J}$

$g_3: IE_3 \leq IE_4$

Side constraints:  $0.7 \leq x_i \leq 3.0$

where

IE: Total internal energy of design variable components

W: Structural weight

IE<sub>2ms</sub>: Internal energy in the first 2 msec

IE<sub>3</sub>: Internal energy of design variable component 3

IE<sub>4</sub>: Internal energy of design variable component 4

Note that we impose 15% structural weight penalty on constraint  $g_1$ . Constraint  $g_2$  is imposed to control the initial peak force within the peak value of the baseline model. Constraint  $g_3$  is used to manage the energy distribution so that the progressive collapse mode will not initiated at the rear end of the rectangular tube.

#### *4.5.3 Numerical Results*

To study the effectiveness and robustness of the proposed methods, five methods are employed to solve the optimization design problem as shown previously. The methods are Sequential regularized Multiquadric with output space mapping (SRMQ/OSM), SRMQ, Implicit Space Mapping (ISM), Direct optimization, Hybrid method (coupling of SRMQ/OSM and direct optimization methods).

While the mathematical formulation of the ISM method will be discussed further in Chapter 6, it is presented herein to compare with other methods. Figure 4.12 shows the design history for all the five methods. All the methods achieve feasible design with no constraint violations. It is observed that the SRMQ/OSM outperforms other methods in terms of the objective function (internal energy). The SRMQ/OSM solution tends to oscillate. The SRMQ method also oscillates at the early stage but tends to behave much smoother as the solution starts to converge. As discussed earlier, the crash functions are very noisy and since the analytical sensitivity analysis for explicit finite element analysis is still not available, finite difference method is used to compute the sensitivity in the direct optimization method. In this work, the step size of the finite difference is chosen to be 5%. It is shown in Figure 4.12 that the direct method tends to converge after 11 design iterations but the design is not as good as the SRMQ/OSM and SRMQ. Among the methods, the ISM approach seems to perform poorly mainly due to the inaccurate sensitivity computed by the finite difference method. In the last approach, we employ the hybrid method by switching the SRMQ/OSM method to the direct gradient-based optimization method starting from the SRMQ/OSM optimal design found in 18 design iterations. It is shown by the design history that the direct gradient-based method is not able to find a better solution than the SRMQ/OSM.

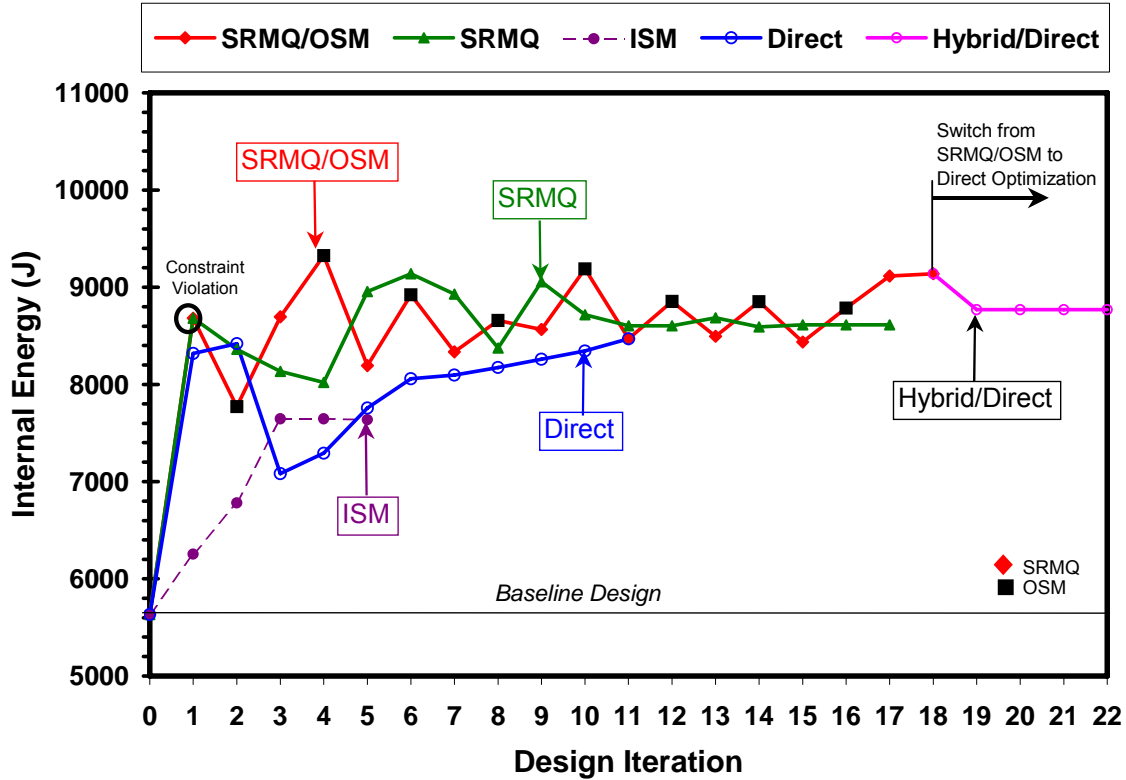


Figure 4.12 Design History Comparisons for Objective Function Using SRMQ, SRMQ/OSM, ISM, Direct and Hybrid Optimization Methods

The constraint design history and design variable history are shown in Figures 4.13 to 4.15 and Figures 4.16 to 4.17, respectively. Note that the constraint  $g_2$  ( $IE_{2ms}$ ) is violated at the 1<sup>st</sup> design iteration for all methods but is corrected afterwards. No constraint is violated at the final design for all methods. The constraint  $g_3$  of the SRMQ/OSM (Figure 4.13(a)) tends to oscillate more than the SRMQ and direct gradient-based methods.

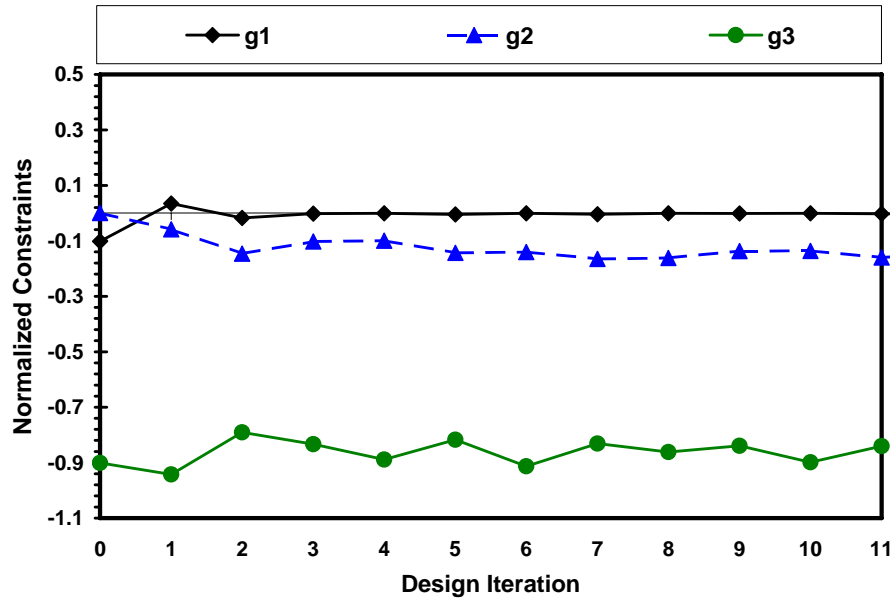


Figure 4.13 Design Constraint History Using SRMQ/OSM Optimization Method

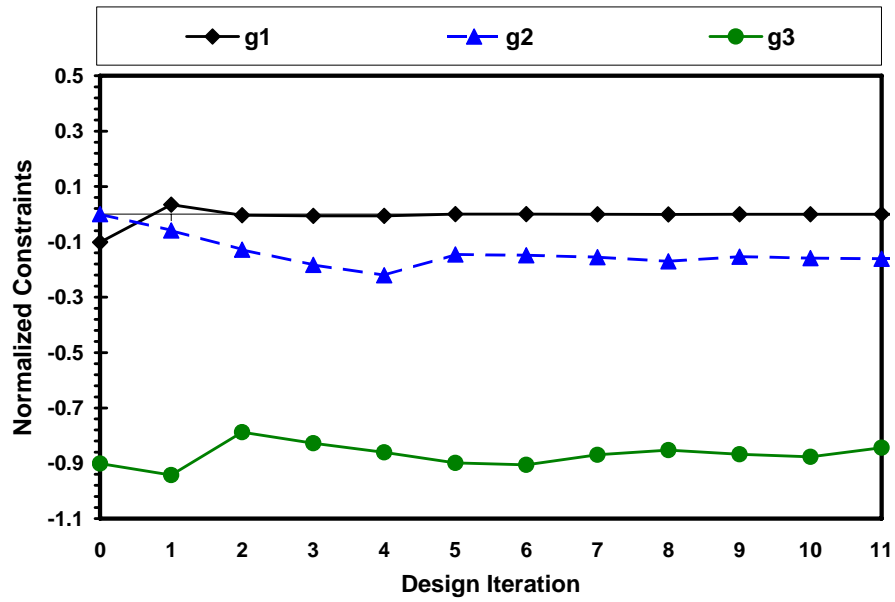


Figure 4.14 Design Constraint History Using SRMQ Optimization Method

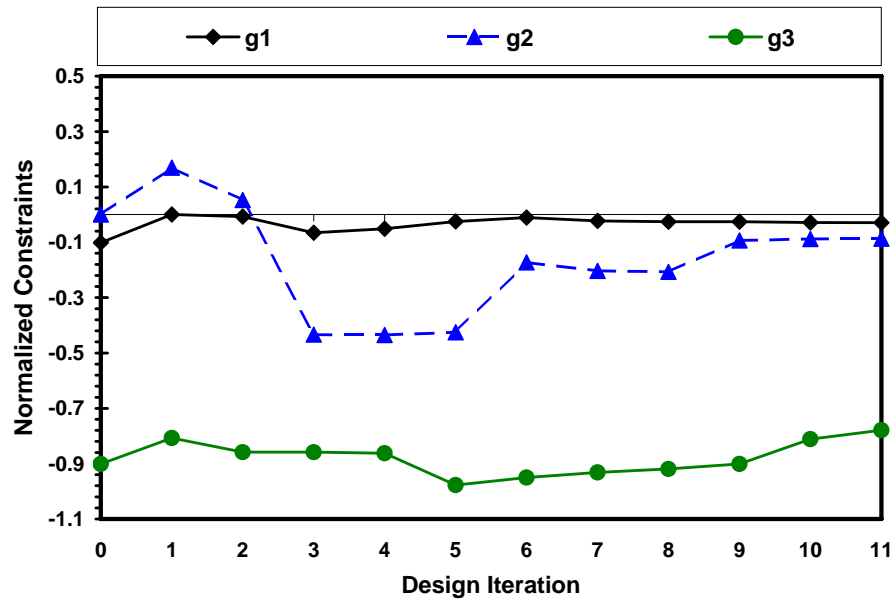


Figure 4.15 Design Constraint History Using Direct Optimization Method

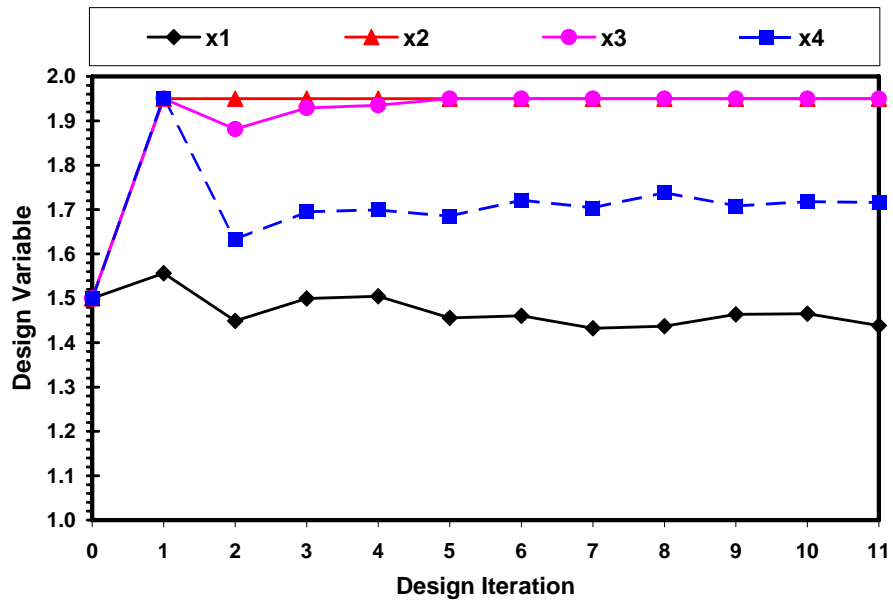


Figure 4.16 Design Variable History Using SRMQ/OSM Optimization Method

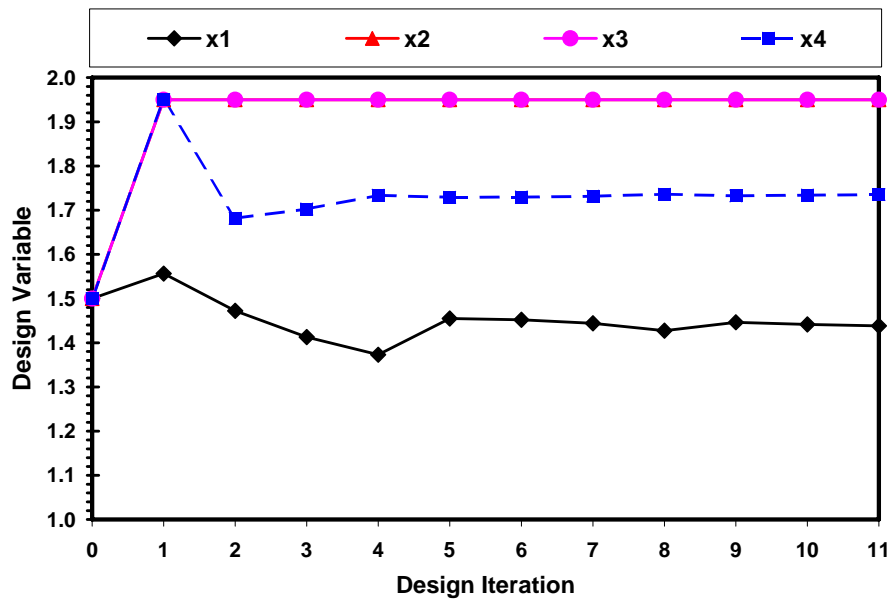


Figure 4.17 Design Variable History Using SRMQ Optimization Method



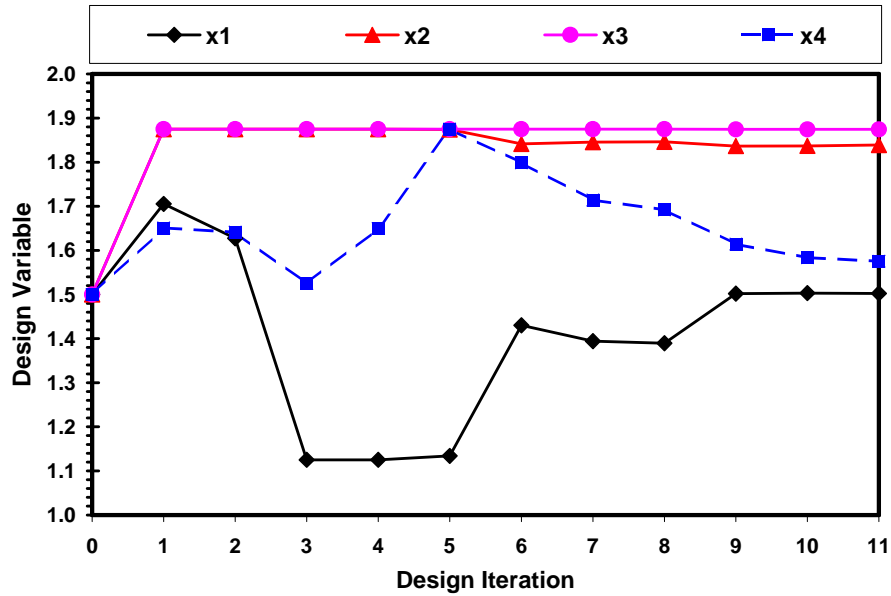


Figure 4.18 Design Variable History Using Direct Optimization Method

Figure 4.19 shows the time history for the rigid wall for all the five methods, respectively. The initial peak force is successfully controlled to be the same or less than the baseline model by imposing a constraint in the optimization process. The time history for the internal energy is shown in Figure 4.20. The SRMQ/OSM outperforms other methods with the internal energy increased by 62.3% (9,140 J) as compared to the baseline (5,633 J). The SRMQ and direct method come in second place and third place with internal energy at 8,614 J (+52.9%) and 8,343 J (+48.1%), respectively. The ISM method performs poorly with internal energy at 7,636 J (35.6%).

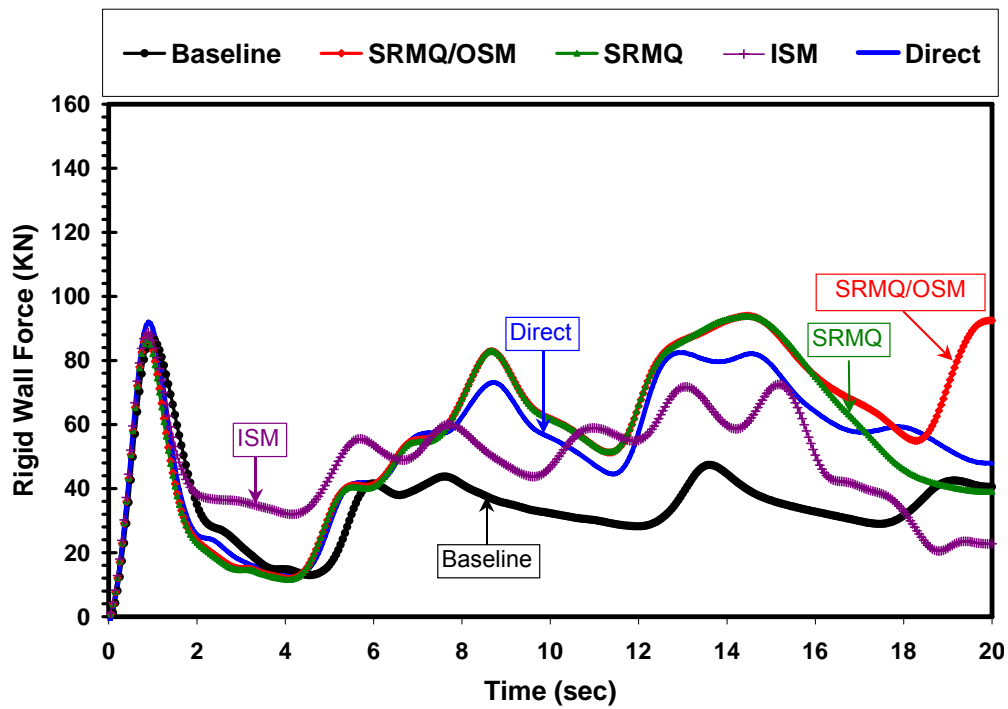


Figure 4.19 Rigid Wall Force Comparisons Using SRMQ, SRMQ/OSM, ISM, Direct and Hybrid Optimization Methods

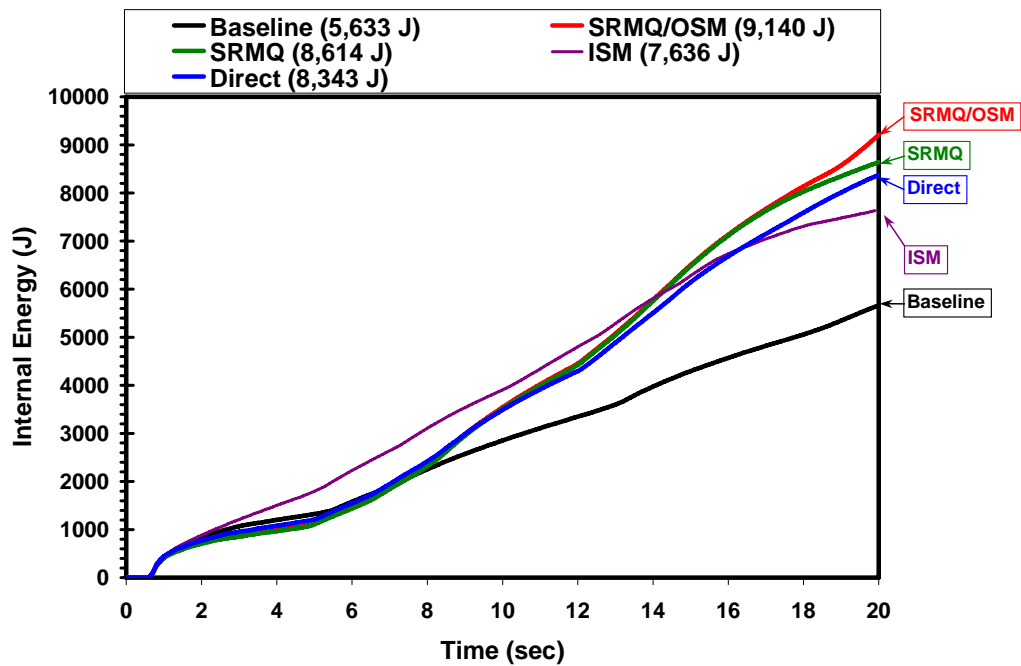


Figure 4.20 Internal Energy Comparisons Using SRMQ, SRMQ/OSM, ISM, Direct and Hybrid Optimization Methods

It is worthwhile to note that the total number of finite element analysis required for the direct gradient-based method is 76 (including finite difference and line search computations). While the SRMQ and SRMQ/OSM require 22 (5+17) and 23 (5+18) analyses, respectively. Note that the SRMQ/OSM starts with a linear RMQ function that requires 5 ( $N+1$ ,  $N$ =number of design variables=4) finite element analyses. Therefore, the SRMQ and SRMQ/OSM methods reduce the total computational cost by about 70% for this rectangular tube crush problem. Note that the computational cost reduction would be more obvious for problems with large number of design variables.

## CHAPTER 5

### LARGE-SCALE SYSTEM OPTIMIZATION USING SRMQ/OSM ALGORITHM

This section presents the applications of the developed SRMQ and SRMQ/OSM algorithms for two large-scale system optimization problems. The first problem is an aerospace industry application: helicopter skid landing gear hard landing optimization. The second problem is an automotive industry application: full vehicle frontal impact optimization.

#### 5.1 Helicopter Skid Landing Gear Hard Landing Optimization

##### *5.1.1 Design Considerations*

When designing helicopter skid landing gear, the principal design criteria considered included the gear's energy absorption capability; its ability to provide adequate ground clearance for both under-fuselage maintenance and access to the aircraft's structure and stores during static ("on-the-deck") and dynamic landing conditions; its capability to accommodate ground handling of the aircraft; and its ability to facilitate loading of the aircraft into cargo aircraft for air transport. Primary design considerations include the redesigned gear's impact on the aircraft's backup structure; its impact on reliability, maintainability, operational suitability, and field durability; and, of course, its impact on aircraft cost, weight, and performance.

#### 5.1.1.1 Crashworthiness Considerations

The design landing condition, which applies to the aircraft's basic structural design gross weight, requires rotor lift to equal the aircraft's weight during the landing condition. For aircraft with skid gear, this design condition stipulates that only the energy-absorbing crossbeams can yield during this landing impact condition. All other landing gear and airframe structure must remain unyielded, thereby allowing the skid gear to be the only piece of "sacrificial structure" requiring replacement after a landing at 12 ft/s or less. Careful design of the skid gear's structural properties is required to optimize energy absorption within the available stroke distance without introducing excessively large loads into the aircraft's backup structure, which would result in increased structural weight.

Other primary landing conditions include the capability for the aircraft to perform a run-on or sliding landing while simultaneously impacting the ground at 12 ft/s, as might occur during autorotation landings. Another is the capability for the aircraft to perform a landing with a side loading force imposed on the skids, which could occur when performing a vertical landing with rolled attitude. An additional new design landing condition imposed upon the aircraft is the requirement to perform a 12-ft/s landing where one of the gear's skid tubes is restricted from deflecting, as might be the case when the aircraft lands in unimproved landing sites where obstructions such as rocks, fallen trees, stumps, or uneven ground could effectively constrain lateral deflection of one skid tube. The significance of this design condition is that it does not

allow the crossbeams on the restricted side of the aircraft to freely deflect and absorb the energy of the landing impact, as they would do when they are unrestrained.

#### 5.1.1.2 Ground Resonance Frequency Considerations

Traditionally, the skid gear crossbeams are generally hollow with circular, symmetric cross sections. These symmetric-section crossbeams are designed to optimize the attenuation of the vertical energy from hard landings as well as to provide adequate fatigue life. In addition, the skid gear must be designed to avoid ground resonance, which requires careful tailoring of its stiffness. The design of the crossbeam's cross section has a dominant impact on the gear's energy absorption, as well as on the overall stiffness of the skid gear. With circular cross sections, therefore, the two design criteria – energy absorption and stiffness – are coupled.

To avoid ground resonance instability, the helicopter must maintain positive damping throughout the entire rotor speed range. Some helicopters employ skid-gear dampers for avoidance of ground resonance, which effectively decouples the frequency placement requirement from the hard landing energy absorption requirement. However, such devices are generally heavy and costly, and they require maintenance.

A skid gear with a circular cross section that provided a stiff natural frequency placement with acceptable ground resonance and vertical energy-absorption characteristics would be heavier than required to meet the  $F/A$  stiffness requirements for ground resonance. Therefore, a crossbeam with a noncircular cross section is introduced to optimize the various design requirements with minimum weight. Decoupling the directional stiffnesses of the crossbeams allows the ground resonance frequency

placements to be optimized, while retaining the vertical-stiffness properties essential for optimizing the required vertical energy attenuation and fatigue life. Accurate modeling of these rectangular crossbeams is required to properly analyze attachment-fitting loads during dynamic landings.

#### *5.1.2 Finite Element Model*

The proposed SRMQ and SRMQ/OSM methods are employed to optimize a genetic helicopter landing gear subjected to the level landing impact requirements. The LS-DYNA finite element model is shown in Figure 5.1. To accurately simulate the structural response, the tapered, hollow box-section crossbeam of the skid landing gear was divided into beam elements approximately 1 inch (2.5 cm) in length. While the aspect ratio of the elements fell outside of the accepted guidelines for classic beam theory, this level of fidelity was required to accurately capture the tapering and curved geometry of the crossbeam. Dimensional properties of the elements were assigned based on data extracted from the CAD geometry and modified using Equations 5.1 and 5.2. The crossbeams were modeled as Hughes-Liu nonlinear beam elements with full cross section integration. The Hughes-Liu beam element, which is based on a degenerated brick element formulation, is appropriate for dealing with finite strains in many practical applications. This type of element was selected for its robustness and computational efficiency. In LS-DYNA, hollow cross section properties are calculated using eight integration points, based on the inner and outer dimensions provided in the input. A total of 204 beam elements were utilized to model the forward and aft

crossbeams. Orientation for the elements was provided by a series of massless nodes located in the primary axis of the cross section plane for each section.

$$t_w = \frac{1}{2} \left\{ w - \left[ \frac{(dw^3 - 12I_2)^3}{wd^3 - 12I_1} \right]^{1/8} \right\} \quad 5.1$$

$$t_f = \frac{1}{2} \left\{ d - \left[ \frac{(wd^3 - 12I_1)^3}{dw^3 - 12I_2} \right]^{1/8} \right\} \quad 5.2$$

The skid tubes were modeled using a Belytschko-Schwer resultant beam formulation with constant crosssectional properties. A total of 80 beam elements was utilized to model behavior of the circular cross section of the left and right skid tubes. Stiff beam elements were employed at the attachment fittings, connected between the fuselage and crossbeams, to provide an analytical entity for recovering the vertical load applied on the attachment fittings during impact. Spotweld elements were employed to represent the saddles as a rigid link between the crossbeams and skid tubes. A piecewise linear representation of the elastic-plastic response of 7075-T26 aluminum alloy was applied to both the crossbeams and skid tubes in the finite element model to accurately represent the material behavior of the structure.

In the finite-element model, the helicopter fuselage was represented by a rigid body whose center of gravity (cg) location, effective drop weight, and mass moments of inertia were defined at a single node location. The fuselage was connected to the attachment fittings of the crossbeams through a set of four rigid links. The steel impact surface was modeled as a rigid panel of 144 shell elements with constraints imposed on



the translational and rotational directions. Dynamic and static frictional coefficients were used to model the sliding contact of the lower surface of the skid tubes and the impact surface. The friction coefficient in LS-DYNA® is calculated using Equation 5.3:

$$\mu_c = f_d + (f_s - f_d)e^{-\beta|V_{rel}|} \quad 5.3$$

where  $f_d$  is the dynamic coefficient of friction,  $f_s$  is the static coefficient of friction,  $\beta$  is the exponential coefficient of decay, and  $V_{rel}$  is the relative velocity of the surface in contact.

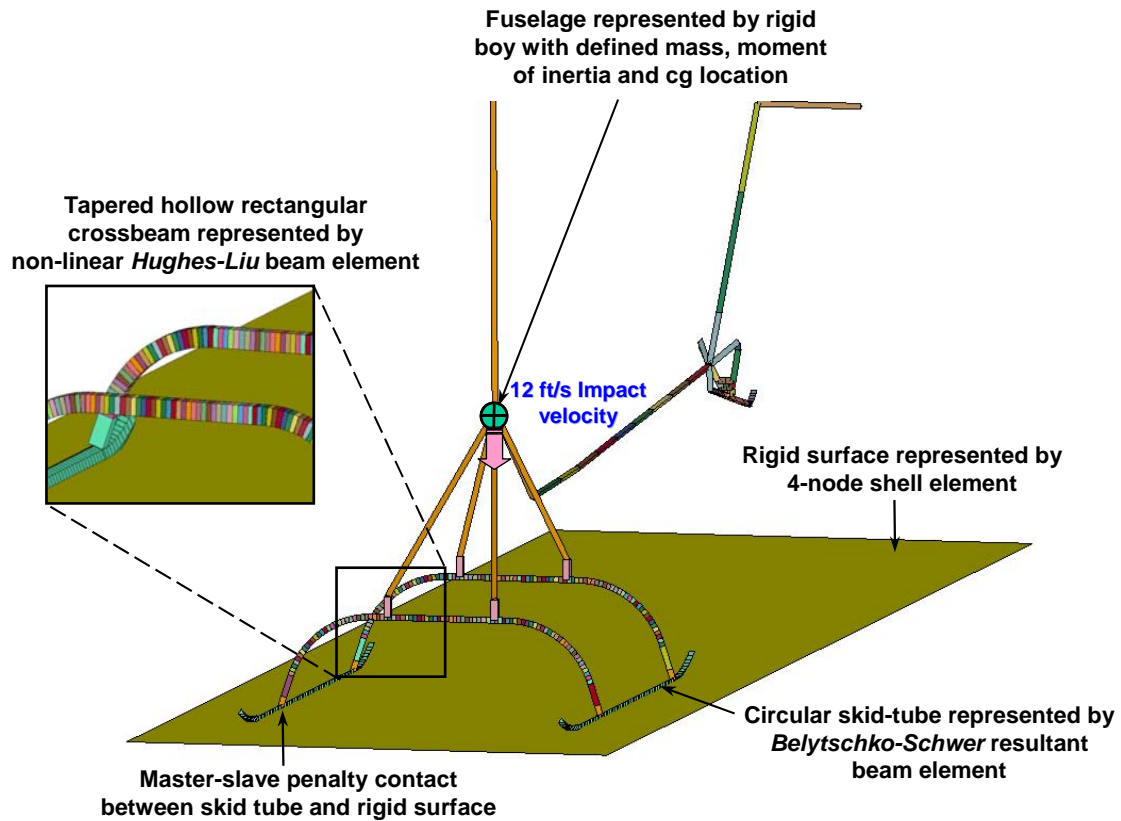


Figure 5.1 Helicopter Skid Landing Gear LS-DYNA Finite Element Model

### 5.1.3 Problem Definition

The design problem is to size the tapered hollow rectangular cross section of the crossbeams, as shown in Figure 5.2, to maximize design objective function and to meet the specified crashworthiness requirements. For simplicity, the actual crossbeam hardware, which contains rounded corners, is modeled using a pure (without rounded corners) hollow rectangular nonlinear beam element. The flange thickness and web thickness of the beam element are calibrated carefully at the expense of cross section area to match the area moment of inertias are matched. To ensure the manufacturability of the optimum design, the scale factor of the cross-sectional geometry is chosen as the design variables to scale the flange thickness and web thickness of the baseline model. The design components are focused on the crossbeams since they are the main contributor to absorb most of the strain energy through the plastic bending deformation during the standard hard landing scenarios (e.g. level landing, run-on landing, roll attitude level landing, and level landing with sideward obstruction). As shown in Figure 5.2, each side of the fwd and aft crossbeams is divided into two sections where each section contains 20 nonlinear beam elements. Due to the symmetry of the crossbeams, there are total 4 sections to be included in the design domain. With each element contains four design variables ( $d$ ,  $w$ ,  $t_f$ ,  $t_w$ ), the total number of design variables in this skid landing gear optimization problem is 16.

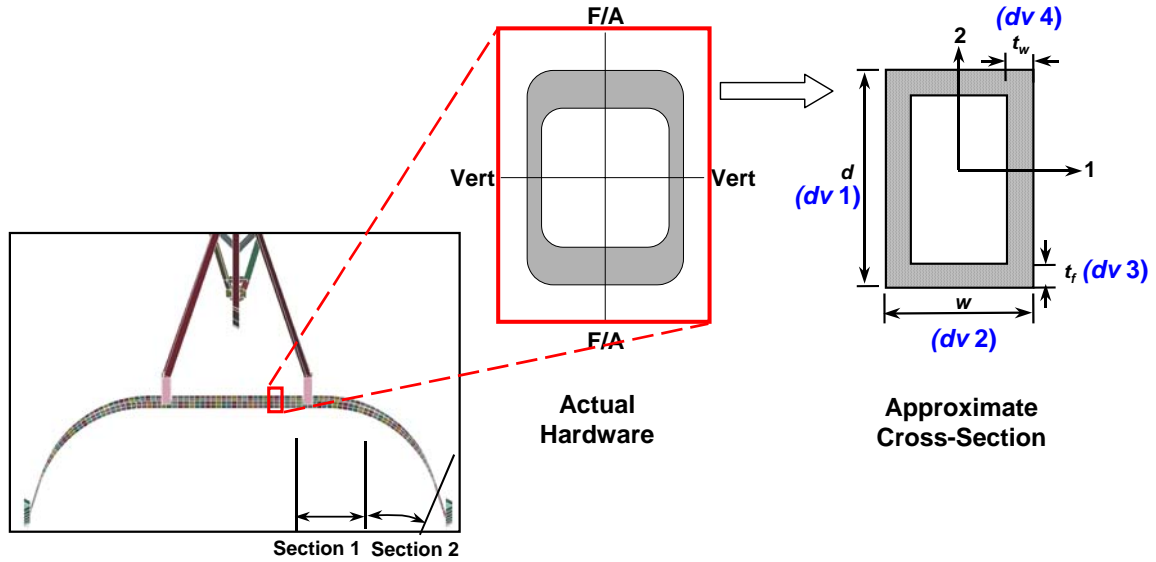


Figure 5.2 Design Variables for Hollow Rectangular Cross-Section Crosstube

The optimization problem is to increase the structural energy absorption efficiency while satisfying the attachment-fitting peak force and peak deformation requirements. Since the internal energy and structural weight are usually coupled, the Specific Internal Energy (SIE) is used as the objective function in the design optimization formulation. The SIE is defined as the ratio of the internal energy over structural weight. The optimization problem is formulated as:

Find  $d_i, w_i, t_{wi}, t_{fi}$  ( $i=1\sim 4$ ) to

Maximize: SIE

Subject to:  $f_{fwd} \leq f_{fwd}^0$

$$f_{aft} \leq f_{aft}^0$$

$$d_{fwd} \leq d_{fwd}^0$$

$$d_{aft} \leq d_{aft}^0$$

where:

$f_{fwd}$ ,  $f_{aft}$  : Fwd and aft crossbeam peak force

$d_{fwd}$ ,  $d_{aft}$  : Fwd and aft crossbeam peak deformation

$f_{fwd}^0$ ,  $f_{aft}^0$  : Fwd and aft crossbeam peak force of baseline model

$d_{fwd}^0$ ,  $d_{aft}^0$  : Fwd and aft crossbeam peak deformation of baseline model

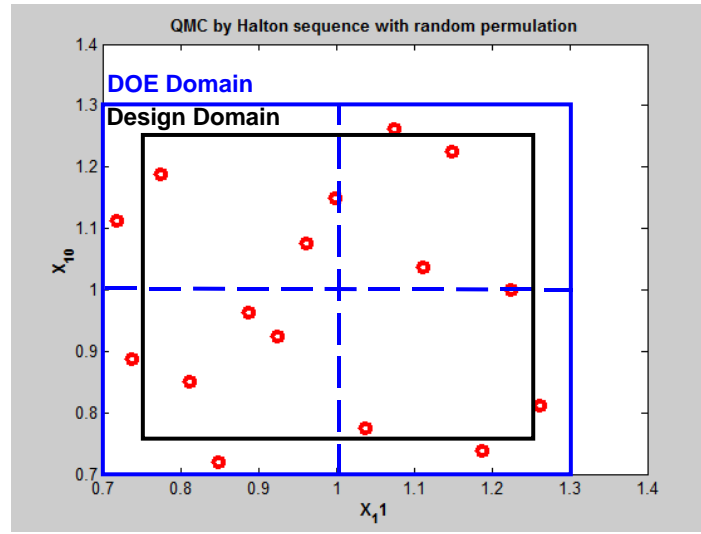


Figure 5.3 Design Domain and DOE Design Sampling for Design Variables 10 and 11 Generated by Halton Sequence

The SRMQ/OSM starts with  $N+1$  Halton Sequence sample runs, where  $N=16$  is the total number of design variables. Namely a total of 17 LS-DYNA simulations are performed initially according to the DOE design points constructed by the Halton sequence. To ensure the sampling points cover the boundary domain, we use  $\pm 30\%$  of the nominal design in selecting the uniformly distributed sampling points using the Halton Sequence DOE method. In the SRMQ/OSM optimization process, we reduce

the design domain to be  $\pm 25\%$ . Figure 5.3 depicts the schematic of the DOE domain and design domain for variables 10 and 11.

#### *5.1.4 Numerical Results*

Two methods of the proposed sequential optimization methods are studied for the helicopter skid landing gear crashworthiness optimization problem. They are SRMQ and SRMQ/OSM. As discussed in Chapter 4, the SRMQ method employs the RMQ function sequentially in the optimization process while the SRMQ/OSM method incorporates the OSM technique to fine tune the RMQ functions. Figure 5.4 shows the design history of the objective function, SIE, using both SRMQ and SRMQ/OSM methods. Note that all the values in this study are normalized for proprietary protection. Although the numbers shown herein do not represent any physical meaning, they do not lose the insight in showing the effectiveness of the proposed optimization method. After 4 design iterations, the SIE of using SRMQ/OSM and SRMQ is increased by 13.1% and 12.3%, respectively, as compared to the baseline design. The improvement of the SIE is mainly contributed by the structural weight reduction, which is reduced by 15.8 lb and 14.3 lb respectively. Note that in the SRMQ/OSM method (as shown in dash line), iterations 1 and 3 represent the design obtained by the SRMQ while iterations 2 and 4 represent the design obtained by the OSM method. Iteration 0 represents the initial baseline design of the skid landing gear model. Both methods in Figure 5.4 use the same number of finite element analyses. While higher SIE represents better energy absorption efficiency, the design obtained by the SRMQ/OSM method is slightly better than the one obtained by the pure SRMQ method.

Figure 5.5 shows the design history of the normalized constraint functions for fwd and aft forces and deformations. The design starts with a feasible design. The aft deformation constraint is violated in the 1<sup>st</sup> iteration. After four iterations, both methods converge to a feasible design with no constraint violation. Note that the aft deformation is an active constraint function.

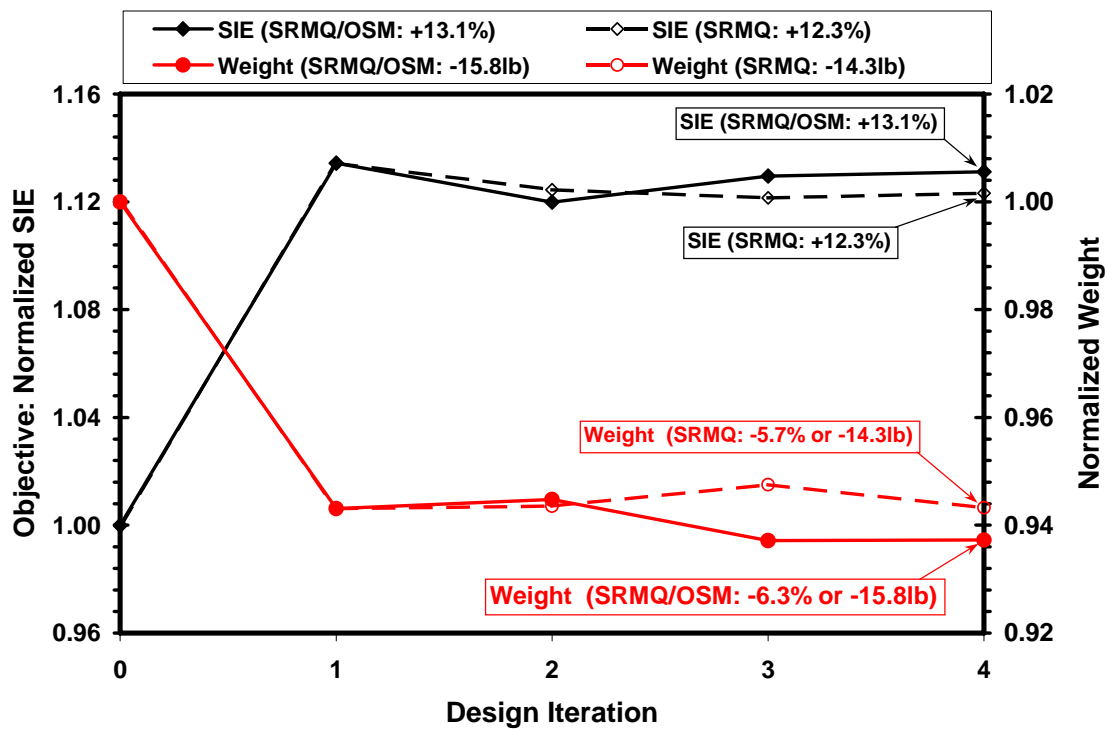


Figure 5.4 Objective Function Design History for Helicopter Skid Landing Gear Optimization Problem

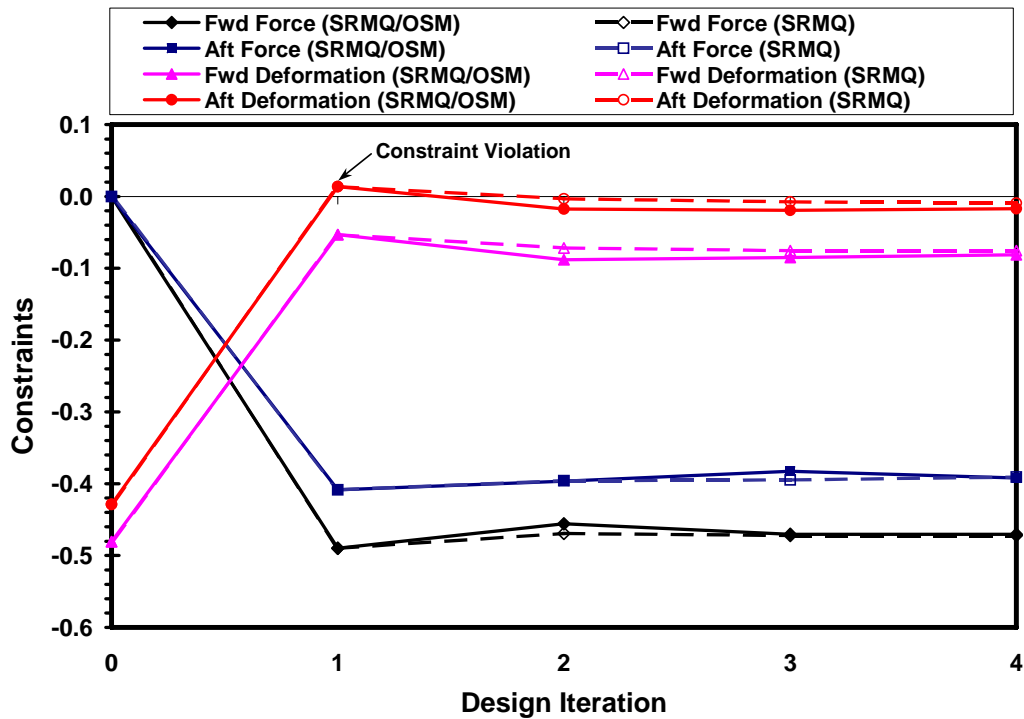


Figure 5.5 Constraint Function Design History for Helicopter Skid Landing Gear Optimization Problem

Figure 5.6 shows the normalized fuselage CG acceleration of the initial baseline and optimum designs. The optimum designs obtained by both methods (both are similar) exhibit better impact performance in terms of energy absorption, peak acceleration, onset rate, and pulse duration. Namely, the normalized peak acceleration is reduced from 1.0 (initial design) to 0.6 (optimum design). The pulse duration is increased from 230 msec to 380 msec approximately. The onset rate of the optimum design is decreased. The energy absorption, even though it is not very obvious from the figure, is increased by about 6%.

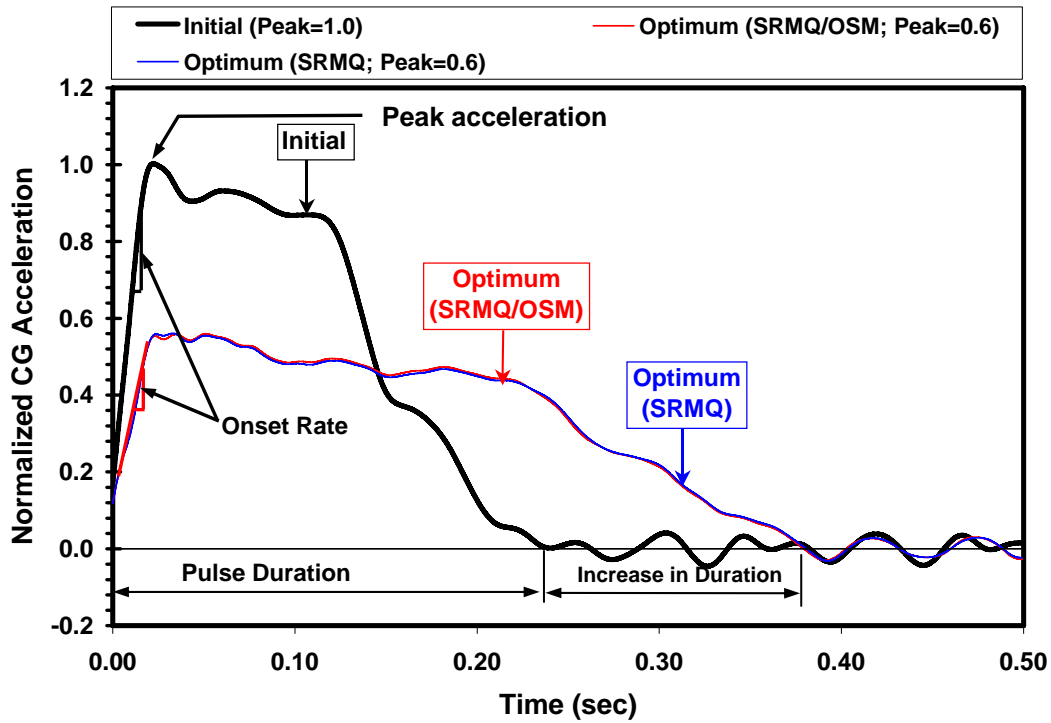
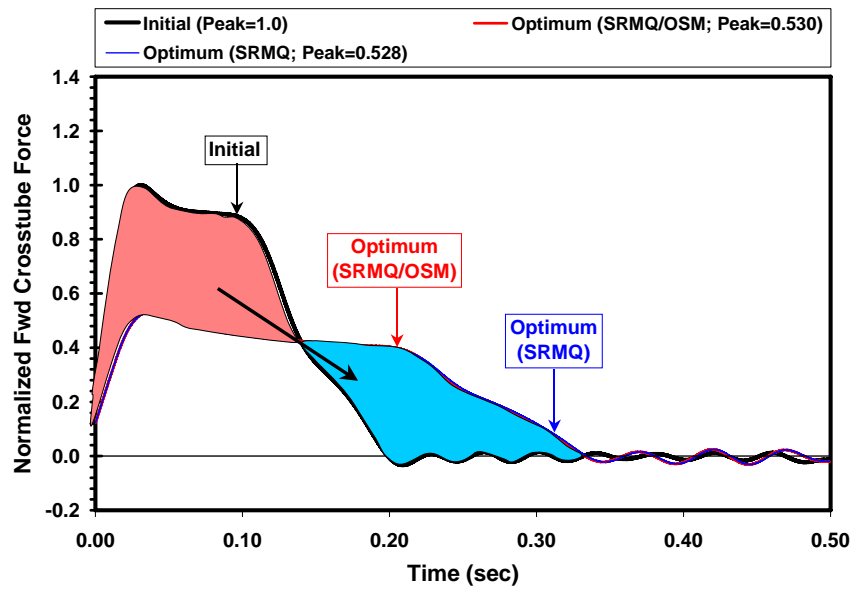


Figure 5.6 Normalized Fuselage CG Acceleration (Initial vs. Optimum)

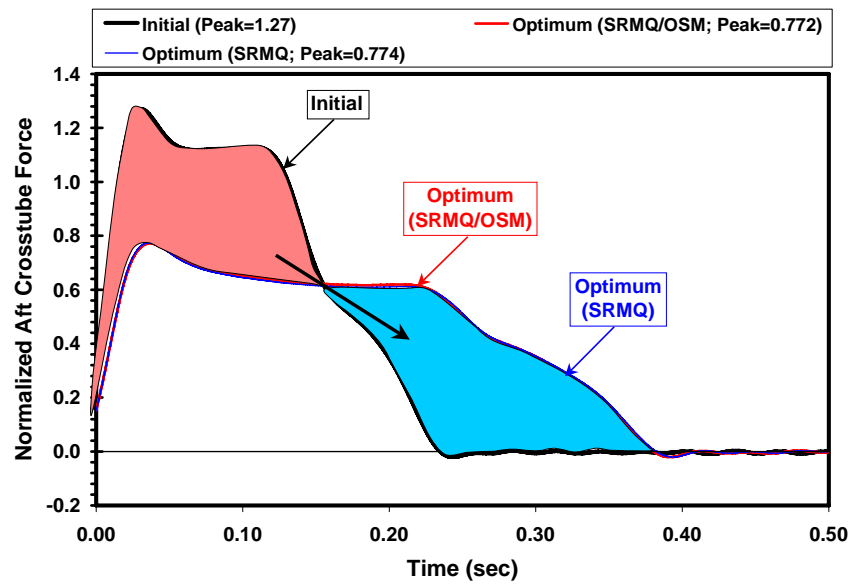
The normalized attachment fitting force of the fwd and aft crossbeams is shown in Figures 5.7 (a) and 5.7 (b), respectively. The attachment fitting force is similar to the fuselage cg acceleration, evidenced by the fact that force is proportional to the acceleration. The normalized fwd peak force is reduced from 1.0 to 0.528 and 0.530 using SRMQ and SRMQ/OSM, respectively. The normalized aft peak force is reduced from 1.27 to 0.774 and 0.772 using SRMQ and SRMQ/OSM, respectively. Figures 5.8 (a) and 5.8 (b) show the normalized crossbeam deformation of the initial baseline model and optimum design for fwd crossbeam and aft crossbeam, respectively. Both fwd and aft crossbeam deformations are increased. This implies that the structural stiffness of the optimum skid landing gear design is softer as compared to the initial baseline



model. Therefore more energy is allowed to dissipate through the plastic deformation of the crossbeams when the hard landing events take place. The fuselage rebounds at approximately at 120 msec and 220 msec for the initial design and the optimum design, respectively.

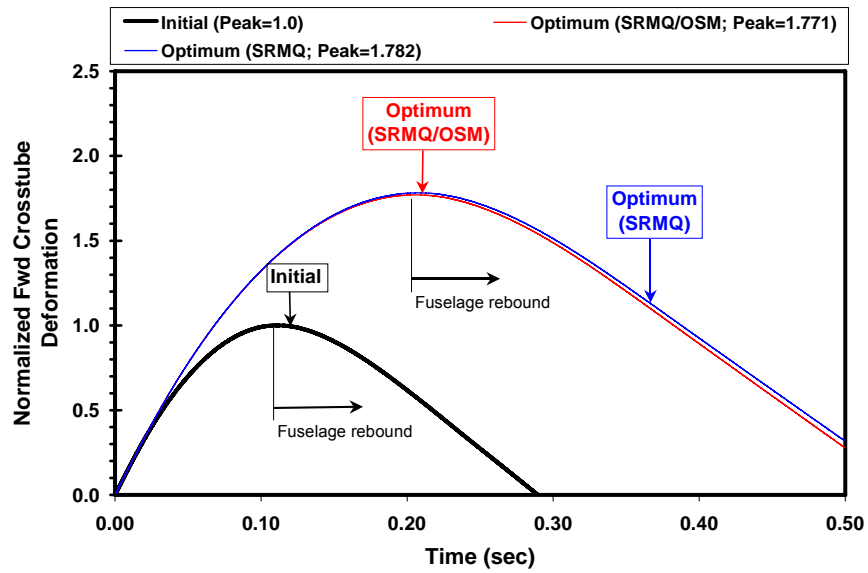


(a)

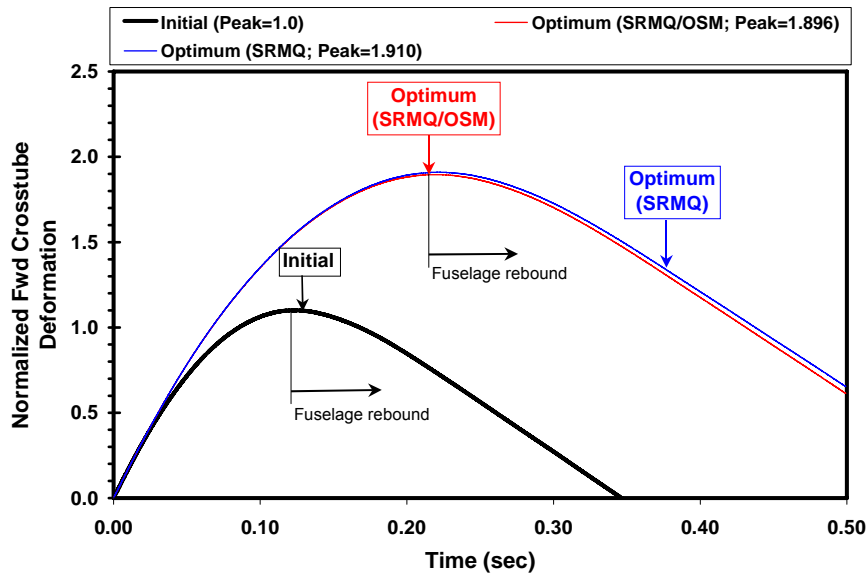


(b)

Figure 5.7 Normalized Crossbeam Attachment Fitting Force (Initial vs. Optimum): (a) Fwd Crossbeam, (b) Aft Crossbeam



(a)



(b)

Figure 5.8 Normalized Crossbeam Deformation (Initial vs. Optimum):  
(a) Fwd Crossbeam, (b) Aft Crossbeam

Figure 5.9 compares the normalized strain energy dissipated by the crossbeams for designs obtained by the SRMQ and SRMQ/OSM methods as compared to the

baseline model. The impact performance of the optimum design is improved, evidenced by the increase in energy absorption. The impact animations of the initial design and optimum design for simulation time at 0 msec, 100 msec, 200 msec and 300 msec are shown statically in Figures 5.10 (a) and 5.10 (b), respectively. Since the optimum design is structurally softer than the initial design, the fuselage does not rebound as early as it does in the initial design. Depending on the design requirements, the maximum allowable deformation can be constrained in the optimization formulation. Namely, a trade-off curve between the energy absorption and structural weight can be obtained by performing a set of optimization problems with different constraint values.

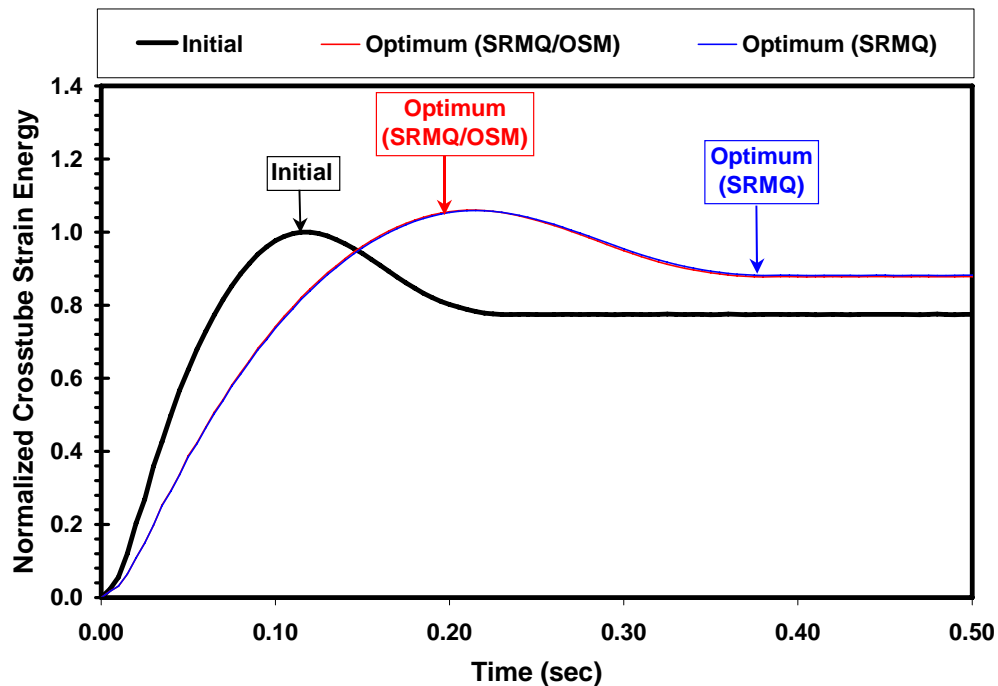


Figure 5.9 Normalized Crossbeam Strain Energy (Initial vs. Optimum)

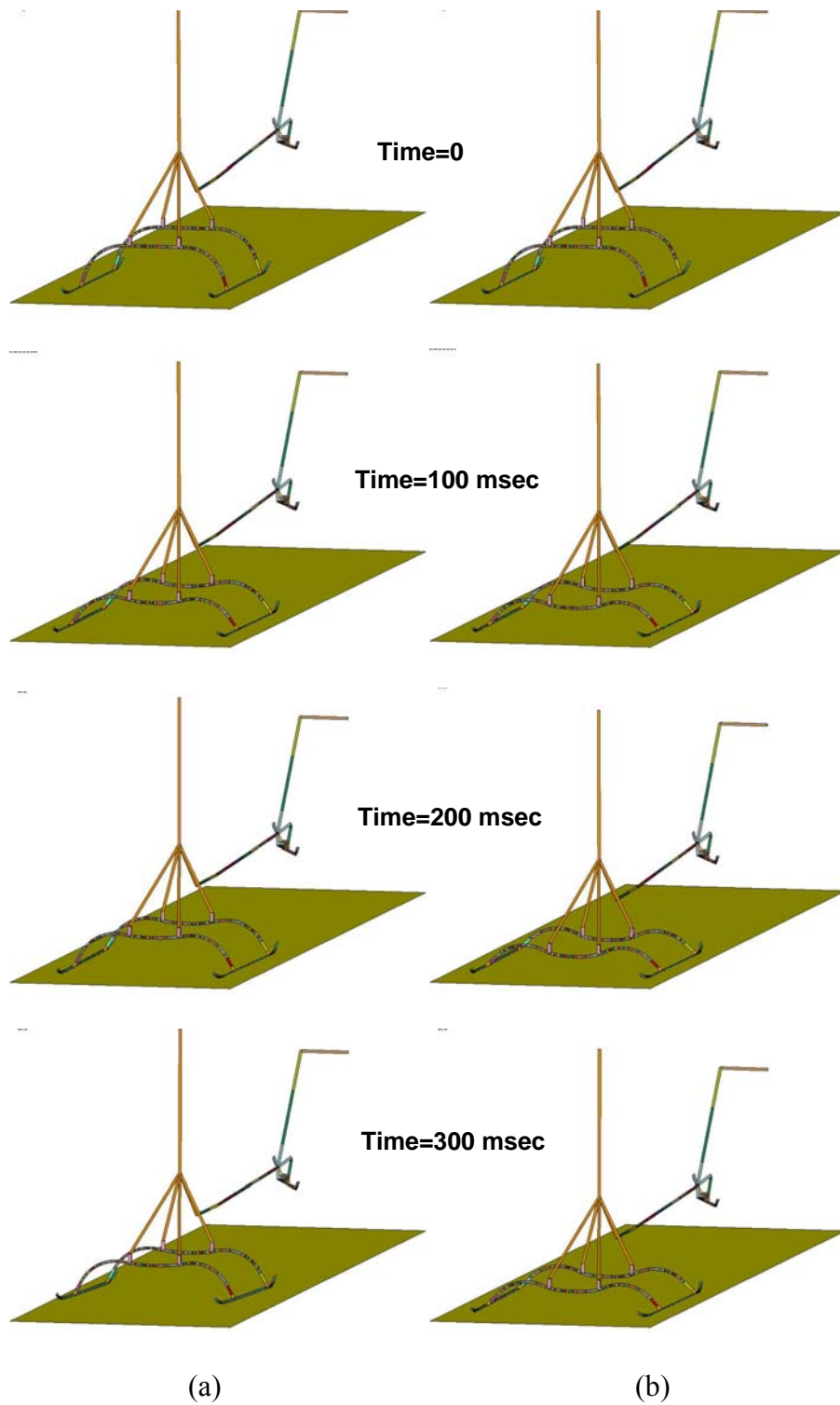


Figure 5.10 Structural Impact Sequence of Helicopter Skid Landing Gear (Initial vs. Optimum): (a) Initial, (b) Optimum

The optimal design obtained using the SRMQ and SRMQ/OSM methods is shown in Table 5.1. The optimum design obtained by both methods is slight different and is highlighted in the table. The response design history matrix using the SRMQ and SRMQ/OSM methods is illustrated in Tables 5.2 and 5.3, respectively. The SIE obtained by the SRMQ method is improved by 12.3% while the one obtained by the SRMQ/OSM method is improved by 13.1%. Both designs are feasible and there is no constraint violation as indicated in the tables.

Table 5.1 Design Variable Design History for Helicopter Skid Landing Gear Optimization Problem

Design Variable	Initial	Final (SRMQ)	Final (SRMQ/OSM)
1	1.000	0.800	0.800
2	1.000	0.800	0.800
3	1.000	<b>0.846</b>	<b>0.858</b>
4	1.000	0.800	0.806
5	1.000	0.800	0.800
6	1.000	<b>0.925</b>	<b>0.906</b>
7	1.000	<b>0.937</b>	<b>0.922</b>
8	1.000	0.800	0.800
9	1.000	0.800	0.800
10	1.000	0.800	0.800
11	1.000	<b>1.059</b>	<b>1.083</b>
12	1.000	<b>0.921</b>	<b>0.929</b>
13	1.000	<b>1.007</b>	<b>1.021</b>
14	1.000	<b>0.831</b>	<b>0.816</b>
15	1.000	<b>1.045</b>	<b>1.042</b>
16	1.000	<b>0.987</b>	<b>0.983</b>

Table 5.2 Response Design History Using SRMQ Optimization Algorithm

Iteration No.	Weight	Energy	Fwd Force	Aft Force	Fwd Disp	Aft Disp	SIE
Baseline	1.000	1.000	0.000	0.000	-0.481	-0.429	1.000
1	0.943	1.070	-0.490	-0.408	-0.053	0.014	1.134
2	0.944	1.061	-0.469	-0.396	-0.072	-0.003	1.124
3	0.948	1.063	-0.472	-0.395	-0.076	-0.007	1.122
4	0.943	1.059	-0.472	-0.391	-0.076	-0.009	1.123
(Obj & Constr)	N/A	N/A	$\leq 1.0$	$\leq 1.27$	$\leq 1.0$	$\leq 1.0$	Maximize

Table 5.3 Response Design History Using SRMQ/OSM Optimization Algorithm

Iteration No.	Weight	Energy	Fwd Force	Aft Force	Fwd Disp	Aft Disp	SIE
Baseline	1.000	1.000	0.000	0.000	-0.481	-0.429	1.000
1	0.943	1.070	-0.490	-0.408	-0.053	0.014	1.134
2	0.945	1.058	-0.456	-0.396	-0.088	-0.018	1.120
3	0.937	1.059	-0.470	-0.383	-0.085	-0.019	1.130
4	0.937	1.060	-0.470	-0.392	-0.081	-0.017	1.131
(Obj & Constr)	N/A	N/A	$\leq 1.0$	$\leq 1.27$	$\leq 1.0$	$\leq 1.0$	Maximize

### 5.1.5 Concluding Remarks

In this section, we have successfully demonstrated the feasibility of using the SRMQ and SRMQ/OSM methods to improve the energy absorption efficiency for a genetic helicopter skid landing gear in reserve-energy of 12 ft/s level landing events. Both methods converged to a feasible design with no constraint violation. The optimal design obtained by the SRMQ/OSM method is shown to be slightly better than the one obtained by the SRMQ method. The proposed SRMQ/OSM method achieved an improved design that reduced the original vehicle structural weight by 15.8 lb and increased the SIE by 13.1%. While the SRMQ reduced the original vehicle structural weight by 14.3 lb and increased the SIE by 12.3%. For the demonstrated helicopter skid landing gear crashworthiness optimization problem, the proposed method used 21

$(N+1+4)$  finite element evaluations, compared to the traditional method DOE/RSM optimization method that would require about 52  $(3N+1+3)$  to 68  $(4N+1+3)$  evaluations. Therefore, the total number of finite element simulations was significantly reduced and the total computational time was reduced by 60~70%. The proposed method has the potential to handle large number of design variables and is more efficient to tackle with large-scale engineering problems.



## 5.2 Full Vehicle Frontal Impact Optimization

The second problem in this Chapter is to optimize a large-scale full vehicle frontal impact problem using the proposed SRMQ/OSM method. Figure 5.11 shows the LS-DYNA finite element model of the 1994 model C2500 pick-up truck, which was originally developed by the FHWA/NHTSA National Crash Analysis Center (NCAC) of the George Washington University [...].

### *5.2.1 Finite Element Model*

The finite element model has been correlated with the test data, shown in Figure 5.12. The model consists of about 58,000 elements and 66,000 nodes. The vehicle crashes into a rigid 90°-barrier wall with an impact speed of 35 mph. The total computational time takes about 6 hours running on an IBM Intellistation (2.8 GHz speed) using single CPU.

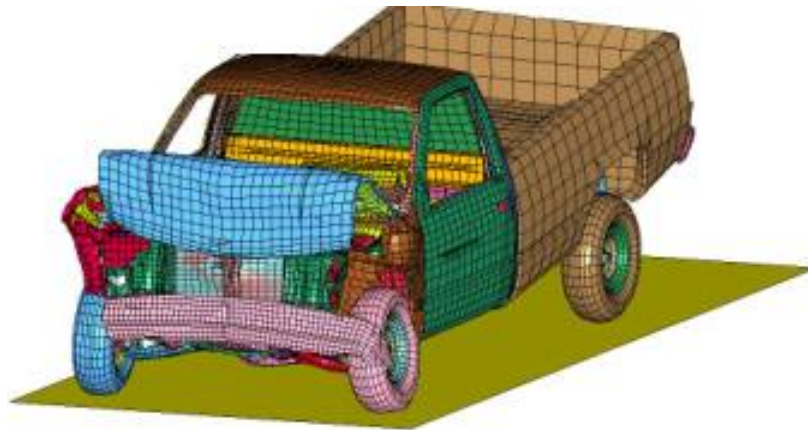


Figure 5.11 C2500 Pick-Up LS-DYNA Frontal Impact Finite Element Model

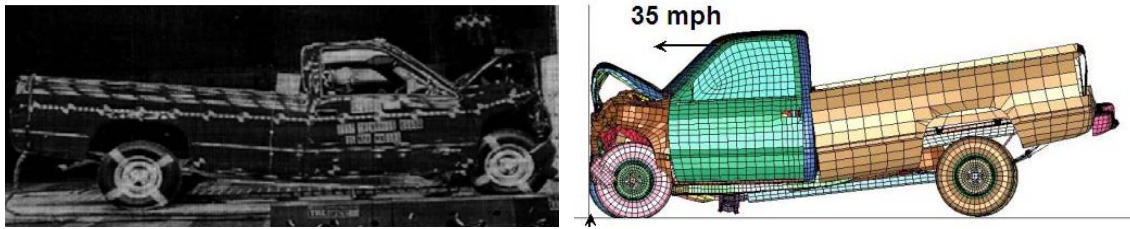


Figure 5.12 C2500 Pick-Up 35 mph Frontal Impact Test Correlation

### 5.2.2 Problem Definition

Ten important design variables, which are significant to the energy absorption attributes, are selected in this frontal impact optimization problem. The design variables include seven sheet metal gauge thickness and three plastic strength scale factors, as shown in Figure 5.13. The components for thickness design variables are: inner front rail, outer front rail, inner fender, outer fender, engine cradle, wheelhouse, and bumper. Among these components, the material plastic strength of the front rail, fender and engine cradle is allowed to alter using a scale factor. Namely, by changing the material property, the structures can either be stiffer or softer depending on the energy absorption management of each component necessary to meet the crashworthiness requirements as defined in the optimization formulation.

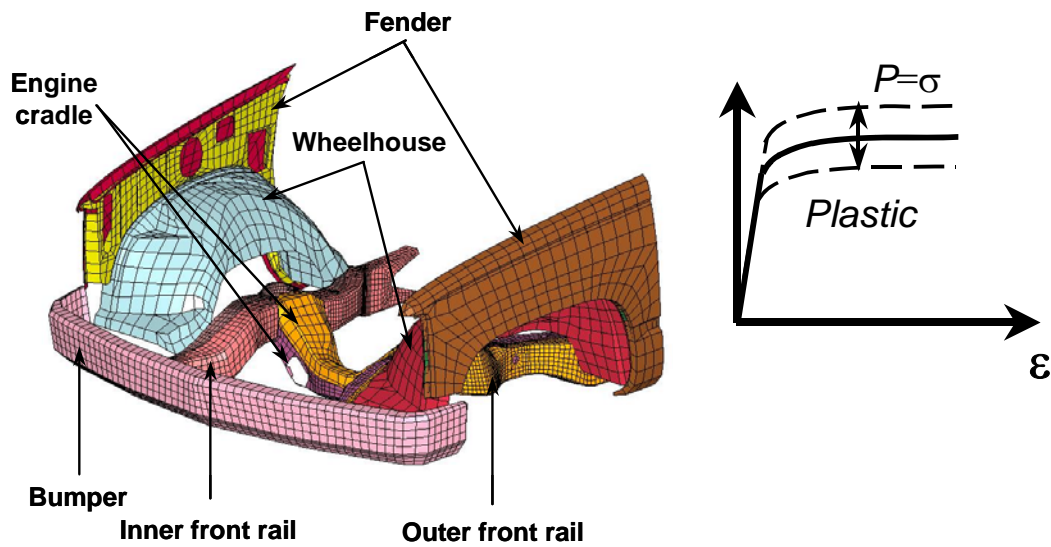


Figure 5.13 Thickness and Material Design Variables for Full Vehicle Frontal Impact Optimization Problem

The optimization problem is to improve the energy absorption efficiency by increasing the structural energy absorption while maintaining the structural weight and peak acceleration (or impact force). The optimization problem is formulated as:

Find the design variables  $x_i$  ( $i=1\sim10$ ) to

Maximize: SIE

Subject to:  $g_1: W \leq W^0$

$g_2: \text{EAR} \leq \text{EAR}^0$

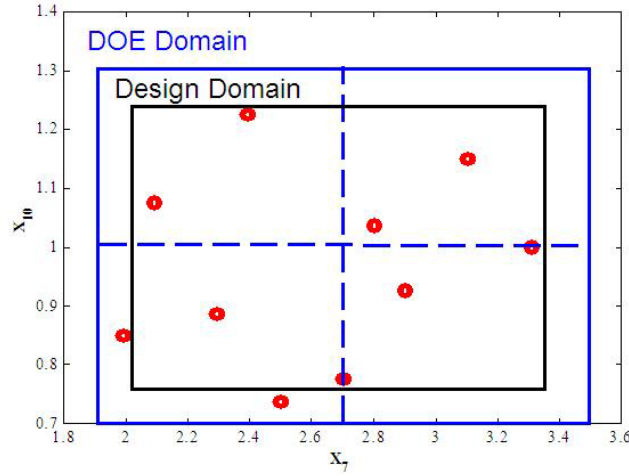


Figure 5.14 Full Vehicle Frontal Impact Design Domain and DOE Sampling for Design Variables 7 and 10 Generated by Halton Sequence

To reduce or maintain the peak rigid wall force (or acceleration), the energy absorption rate between 40 msec and 50 msec is constrained in the optimization formulation. The SRMQ/OSM starts with  $N+1$  Halton Sequence sample runs, namely 11 LS-DYNA finite element simulations are initially. To ensure the sampling points cover the boundary domain, we use  $\pm 30\%$  of the nominal design in selecting the uniformly distributed sampling points using the Halton Sequence DOE method. In the SRMQ/OSM optimization process, we reduce the design domain to  $\pm 25\%$ . Figure 5.14 depicts the DOE domain and design domain for variables 7 and 10.

### 5.2.3 Numerical Results

The design history of the objective function, SIE, is shown in Figure 5.15. Note that iterations 1, 3, 5, 7 are the design obtained by the SRMQ method while iterations 2, 4, 6, 8 are the design obtained by the OSM method to fine-tune the SRMQ objective and constraint functions. Design iteration 0 represents the initial baseline model. After

8 design iterations, the SIE is increased by 10% as compared to the baseline design. The improvement of the SIE is mainly contributed by the structural weight reduction, which is reduced by 11.8 Kg. The design history of the normalized constraint functions (i.e. structural weight and energy absorption rate) is shown in Figure 5.16. The design starts with a feasible design. After 8 design iterations, a feasible design with no constraint violation is achieved.

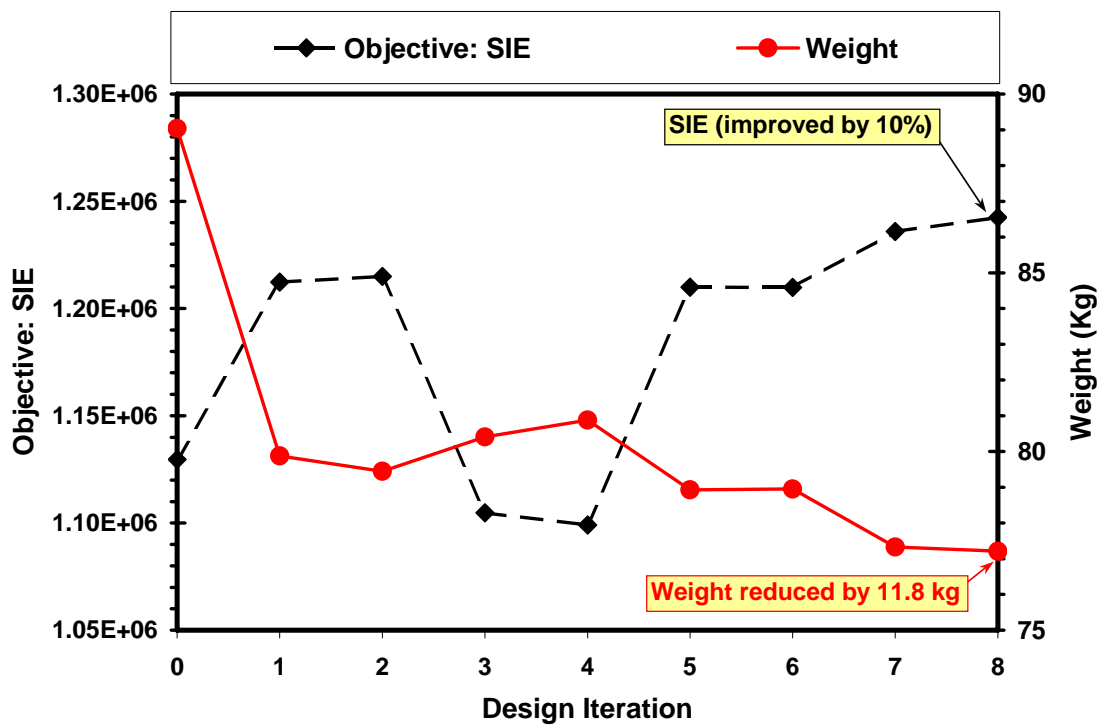


Figure 5.15 Objective Function Design History for Full Vehicle Frontal Impact Using SRMQ/OSM Optimization Algorithm

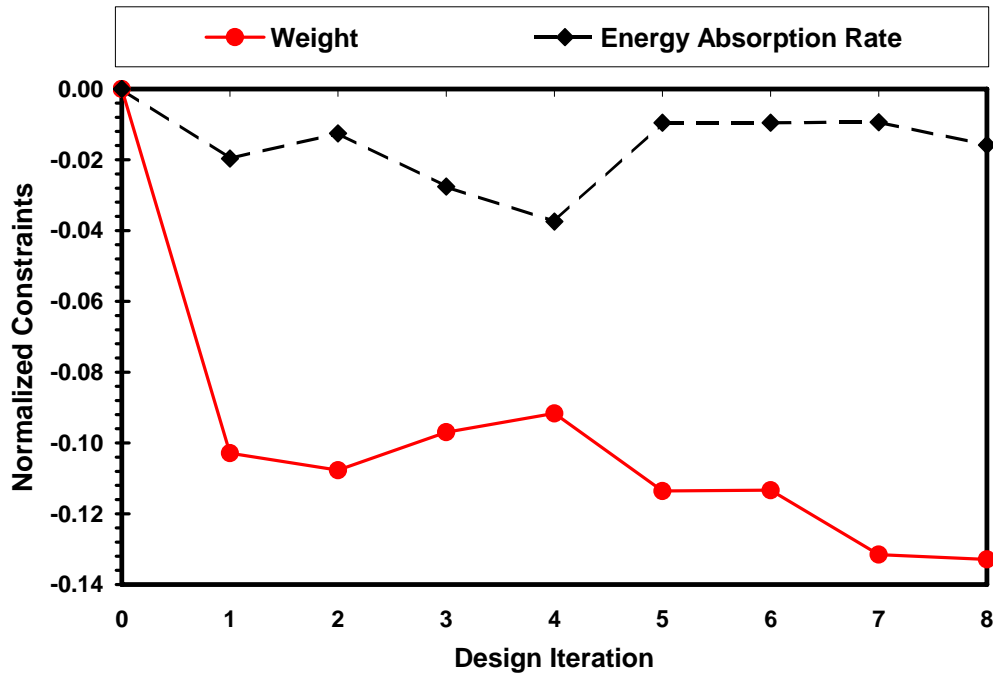


Figure 5.16 Constraint Function Design History for Full Vehicle Frontal Impact Using SRMQ/OSM Optimization Algorithm

Figure 5.17 shows the SIE comparison (baseline vs. optimum) in time domain history after 8 design iterations. The total rigid wall force of the baseline and optimum is shown in Figure 5.18. Note that the peak force is reduced from 1,023 KN to 940KN by imposing the energy absorption rate constraint between 40 msec and 50 msec, as shown in Figure 5.17, where the peak force occurs. Comparing the rigid wall force of the baseline and optimal designs in Figure 5.18, it implies that the optimal design absorbs about the same internal energy but the structural weight is reduced by 11.8 Kg as shown in Figure 5.17.

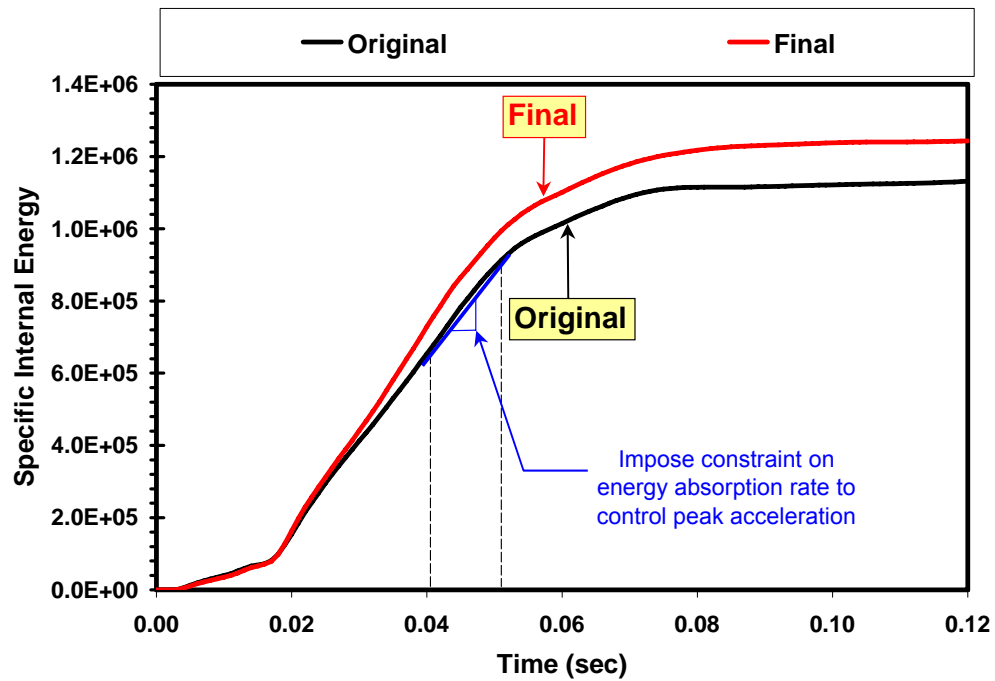


Figure 5.17 Original and Final Specific Internal Energy Comparison for Full Vehicle Frontal Impact Using SRMQ/OSM Optimization Algorithm

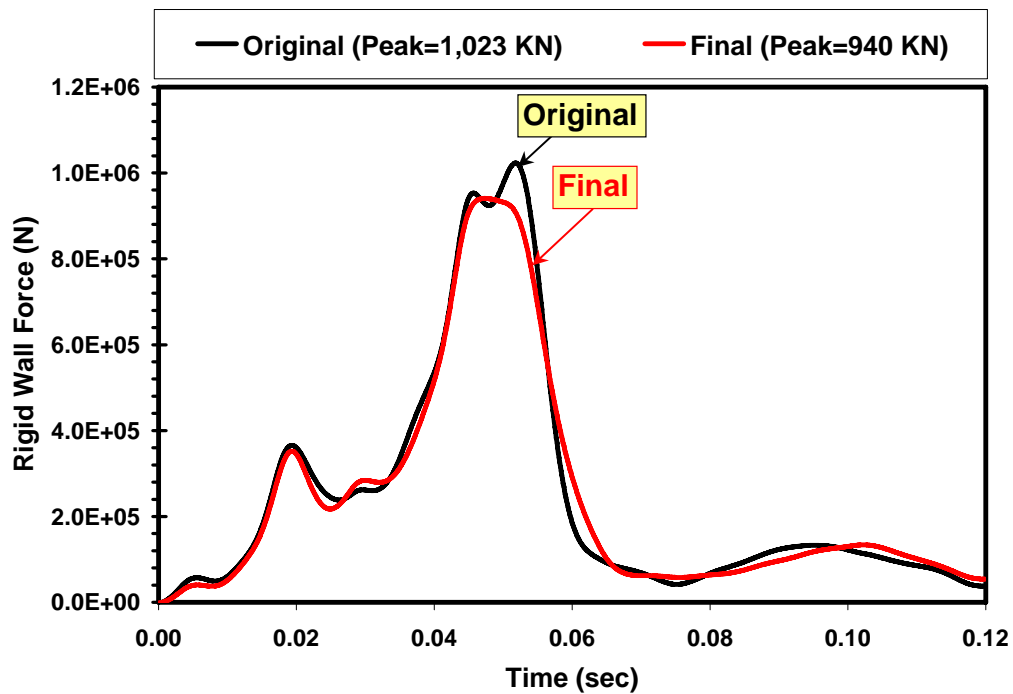


Figure 5.18 Original and Final Rigid Wall Force Comparison for Full Vehicle Frontal Impact Using SRMQ/OSM Optimization Algorithm

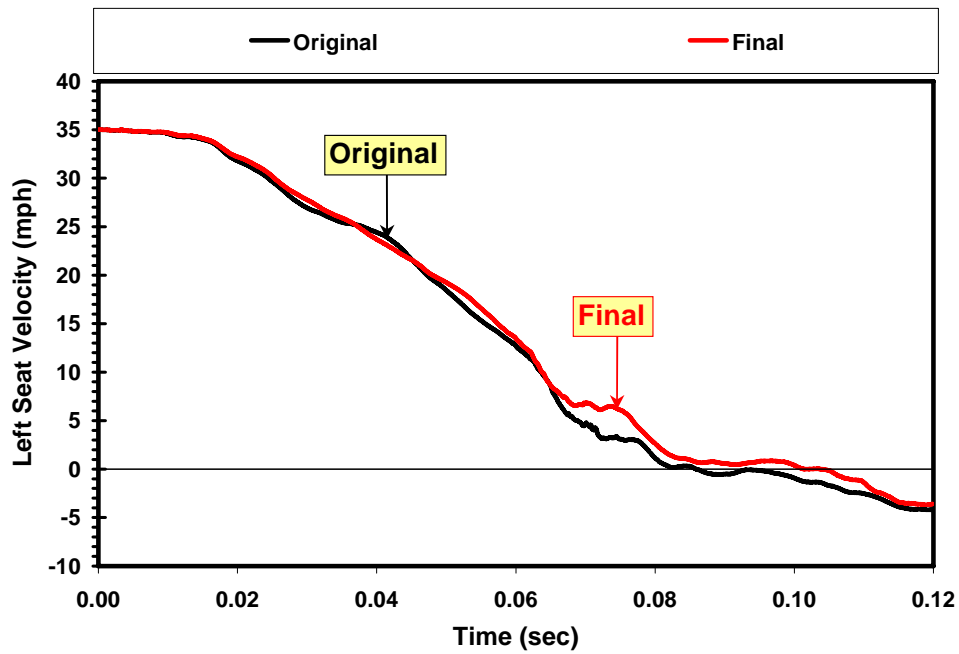


Figure 5.19 Left Seat Velocity (Original vs. Final) Comparison for Full Vehicle Frontal Impact Using SRMQ/OSM Optimization Algorithm

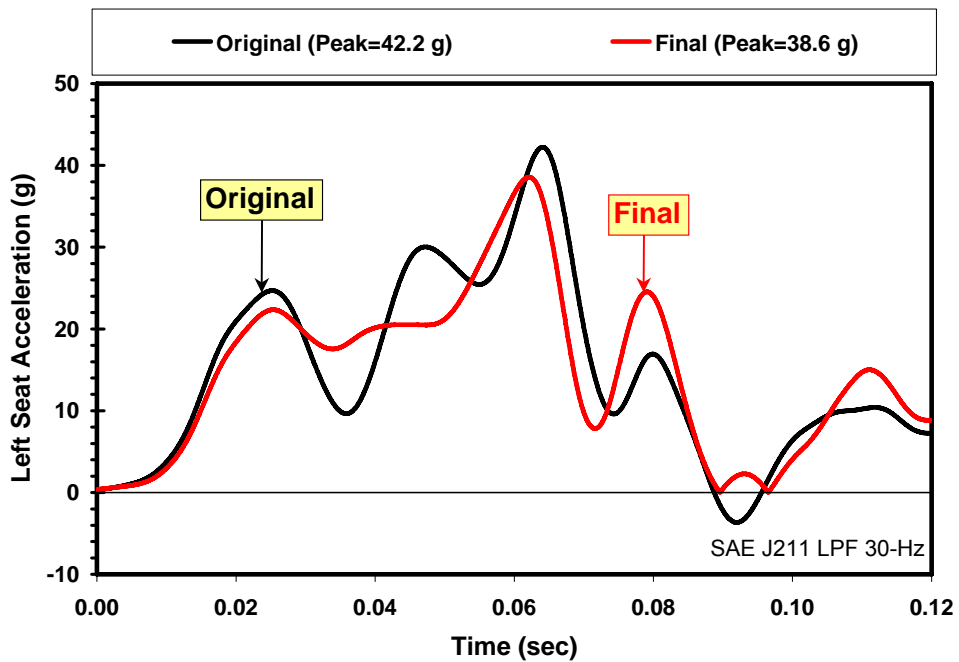


Figure 5.20 Left Seat Acceleration (Original vs. Final) Comparison for Full Vehicle Frontal Impact Using SRMQ/OSM Optimization Algorithm



Figures 5.19 and 5.20 shows the velocity and acceleration comparison at the occupant left seat between the two designs, respectively. The DOE matrix for the design variables and design history are shown in Tables 5.4 and 5.5, respectively.

Table 5.4 DOE Matrix and Design Variable History for Full Vehicle Frontal Impact Using SRMQ/OSM Optimization Algorithm

DOE No.	Design Variables									
	$x1$	$x2$	$x3$	$x4$	$x5$	$x6$	$x7$	$x8$	$x9$	$x10$
1	3.1000	3.1000	0.7530	0.8040	3.6000	0.6960	2.7000	1.0000	1.0000	1.0000
2	3.3325	2.4025	0.6683	0.7437	3.3300	0.6177	2.0925	0.8500	0.9250	1.0000
3	3.5650	2.2863	0.5836	0.8040	4.4100	0.6438	3.3075	1.0375	1.0375	1.0375
4	3.1000	3.1000	0.6965	0.9246	3.0600	0.8004	2.4975	0.8875	1.0000	1.2250
5	2.6350	2.7513	0.5553	0.6834	2.6550	0.5394	2.9025	1.0750	1.2250	0.7375
6	2.8675	3.7975	0.6401	0.6231	4.1400	0.7221	2.3963	0.9250	1.1500	0.8875
7	2.4025	2.6350	0.8095	0.8643	3.7350	0.5916	2.2950	0.7375	0.7750	0.7750
8	3.7975	3.5650	0.7812	0.5930	3.1950	0.7482	3.1050	0.7750	0.8500	1.1500
9	2.7513	3.2163	0.7530	0.8342	3.8700	0.8526	2.7000	1.1500	0.7375	1.0750
10	3.2163	2.8675	0.9224	0.7136	2.7900	0.6960	1.9913	1.2250	1.0750	0.8500
11	2.2863	3.3325	0.8660	0.9849	3.6000	0.5133	2.8013	1.0000	0.8875	0.9250
Iter. No.	Design History									
	$x1$	$x2$	$x3$	$x4$	$x5$	$x6$	$x7$	$x8$	$x9$	$x10$
1	3.4190	2.5135	0.6101	0.7522	3.3620	0.5645	2.025 (L)	1.0869	1.0430	1.0740
2	3.3939	2.5171	0.6300	0.7423	3.3517	0.5588	2.025 (L)	1.0654	1.0367	1.0438
3	3.4684	2.6140	0.5647	0.7755	3.4787	0.522 (L)	2.025 (L)	1.2500 (U)	1.8870	1.1760
4	3.5045	2.6213	0.5647	0.7898	3.4934	0.522 (L)	2.025 (L)	1.2500	1.2097	1.2216
5	3.4008	2.4932	0.5901	0.6624	3.2532	0.5415	2.025 (L)	1.0477	0.8645	0.8611
6	3.4017	2.4927	0.5895	0.6623	3.2528	0.5418	2.025 (L)	1.0478	0.8637	0.8610
7	3.4148	2.5393	0.5647 (L)	0.6248	3.2437	0.522 (L)	2.029 (L)	1.0949	0.7997	0.7773
8	3.4109	2.5310	0.5647 (L)	0.6221	3.2437	0.522 (L)	2.025 (L)	1.0955	0.7915	0.7708
Lower Bound	2.3250	2.3250	0.5647	0.6030	2.7000	0.5220	2.0250	0.7500	0.7500	0.7500
Upper Bound	3.8750	3.8750	0.9412	1.0050	4.5000	0.8700	3.3750	1.2500	1.2500	1.2500

Table 5.5 Response Matrix and Design History for Full Vehicle Frontal Impact Using SRMQ/OSM Optimization Algorithm

DOE No.		Weight (Kg)	Energy (N-mm)	Energy Rate	SIE	Improvement %
1	1	89.04	1.0058E+08	6.0600E+07	1129650	N/A
	2	79.61	9.1640E+07	5.9610E+07	1151117	1.9
	3	92.03	9.7532E+07	5.9430E+07	1059784	-6.2
	4	87.56	9.7803E+07	6.0310E+07	1116983	-1.1
	5	<i>Simulation is discarded due to large mass scaling</i>				
	6	89.56	1.0015E+08	6.1260E+07	1118189	-1.0
	7	79.58	8.4102E+07	6.3720E+07	1056828	-6.4
	8	96.12	1.0144E+08	6.2280E+07	1055347	-6.6
	9	90.37	1.0172E+08	6.2270E+07	1125628	-0.4
	10	81.54	9.1661E+07	5.9750E+07	1124123	-0.5
	11	86.31	9.6685E+07	5.9390E+07	1120202	-0.8
Evaluation No.		Design History				
1	SRMQ prediction	81.21	9.4120E+07	5.9470E+07	1159042	2.6
	Validation	79.88	9.6840E+07	5.9410E+07	1212318	7.3
2	OSM prediction	80.58	9.3380E+07	5.8240E+07	1158848	2.6
	Validation	79.45	9.6530E+07	5.9840E+07	1214978	7.6
3	SRMQ prediction	82.16	1.0028E+08	5.8930E+07	1220545	8.0
	Validation	80.41	8.8830E+07	5.8610E+07	1104713	-2.2
4	OSM prediction	82.93	1.0058E+08	5.8650E+07	1212801	7.4
	Validation	80.88	8.8890E+07	5.8330E+07	1099036	-2.7
5	SRMQ prediction	80.23	9.7360E+07	6.1100E+07	1213511	7.4
	Validation	78.93	9.5500E+07	6.0020E+07	1209933	7.1
6	OSM prediction	80.25	9.7380E+07	6.1100E+07	1213473	7.4
	Validation	78.95	9.5520E+07	6.0020E+07	1209880	7.1
7	SRMQ prediction	79.09	9.4770E+07	6.0150E+07	1198316	6.1
	Validation	77.33	9.5570E+07	6.0030E+07	1235872	9.4
8	OSM prediction	79.11	9.4610E+07	6.0200E+07	1195937	5.9
	Validation	77.21	9.5930E+07	5.9640E+07	1242456	10.0
Objective or Constraint		≤ 89.04	N/A	≤ 6.06×10 <sup>7</sup>	Maximize	N/A

#### *5.2.4 Concluding Remarks*

We have successfully demonstrated the feasibility of using the SRMQ/OSM to improve the 35 mph frontal impact energy absorption efficiency of the C2500 pick-up truck. The SRMQ/OSM solution converged to a feasible design with no constraint violation. The proposed method achieved an improved design that reduced the original vehicle structural weight by 11.8 Kg and increased SIE by 10%. For the demonstrated C2500 pick-up frontal impact optimization problem, the method used 19 ( $N+1+8$ ) finite element evaluations, compared to the traditional DOE/RSM optimization method that would require about 34 ( $3N+1+3$ ) to 44 ( $4N+1+3$ ) evaluations. Therefore, the total number of finite element simulations was significantly reduced and the total computational time was reduced by 44~55%. The proposed method has the potential to handle large number of design variables and is therefore more efficient to tackle with large-scale engineering problems.

## CHAPTER 6

### IMPLICIT SPACE MAPPING CRASHWORTHINESS OPTIMIZATION

#### 6.1 Introduction

An efficient design optimization methodology for solving large-scale Crashworthiness problems using the Implicit Space Mapping (ISM) methodology is proposed in this section of the dissertation. The Space Mapping (SM) was originally developed by John Bandler [7, 8, 9, 10] as an efficient approach for optimizing microwave devices and systems to avoid computationally expensive engineering system simulations. Two models are required in the SM based optimization method: a high-fidelity (fine) model and a low-fidelity (coarse) model. The fine model is typically computational intensive but more accurate while the coarse model is computational efficient but provides less reliable analytical predictions. The SM approach takes advantage of these two models by using the ‘physics-based’ efficient coarse model to perform the design optimization while using the accurate fine model for design response validation. The coarse model is calibrated through the parameter extraction process in order to match with the fine model responses. The process repeats until the optimization solution converges.

Conceptually, SM is very similar to RSM. But there are two major differences. In RSM, we approximate the responses using various mathematical functions, while the

surrogates used in SM are physics-based models. Essentially any simplified model can be used as a surrogate model. For RSM, many high-fidelity function evaluations are required to construct a surrogate sufficiently accurate for design optimization purposes. In SM, only one high-fidelity function evaluation (or finite element analysis) is required each of the design iteration in the optimization process. This makes SM much more efficient than the traditional RSM approach.

While most of SM applications have been on the electromagnetic and circuit optimization, there are several papers reported the use of SM techniques for the crashworthiness design optimization. Redhe *et al.* [71] investigated the feasibility of using the space mapping technique in combination with the response surface methodology for a thin-walled beam impact optimization problem and a vehicle impact optimization problem. In their implementation, they employed LS-OPT, a commercial optimization code by Livermore Software Technology Corporation using successive approximation optimization method, to approximate the mapping between the coarse model and fine model sequentially by constructing the response surface using linear approximations around the current set of parameters. Essentially the coarse model determines the search direction while the fine model determines the design point for the next iteration. They found that the optimization algorithm using space mapping, in general, works reasonably well and reduces the computational time significantly. However, the algorithm appears to be less stable and might not converge when the initial mapping between the coarse model and fine model is very poor.

## 6.2 Review of Space Mapping Optimization Algorithms

### *6.2.1 Space Mapping Optimization Basic Concepts*

Space mapping establishes a mathematical link (mapping)  $\mathbf{P}$  between two spaces:

$$\mathbf{x}_c = \mathbf{P}(\mathbf{x}_f) \quad 6.1$$

such that

$$\mathbf{R}_c(\mathbf{P}(\mathbf{x}_f)) \approx \mathbf{R}_f(\mathbf{x}_f) \quad 6.2$$

where  $\mathbf{x}_c \in \mathfrak{R}^{n \times 1}$  and  $\mathbf{x}_f \in \mathfrak{R}^{n \times 1}$  denote the design parameters of the coarse model and fine model, respectively. The corresponding response vectors are denoted by  $\mathbf{R}_c \in \mathfrak{R}^{m \times 1}$  and  $\mathbf{R}_f \in \mathfrak{R}^{m \times 1}$  respectively. The mapping  $\mathbf{P}$  is valid over a region of interest.

The general design optimization problem can be formulated as:

$$\mathbf{x}^* = \arg \left\{ \min_{\mathbf{x}} U(\mathbf{R}(\mathbf{x})) \right\} \quad 6.3$$

where  $\mathbf{x}^*$  is the design parameters,  $U$  is the scalar objective function, and  $\mathbf{R} \in \mathfrak{R}^{m \times 1}$  is the vector of the model responses. For complex engineering systems, direct optimization by solving Equation 6.3 may be prohibitive. The thrust of SM is to avoid direct optimization and declare

$$\bar{\mathbf{x}}_f = \mathbf{P}^{-1}(\mathbf{x}_c^*) \quad 6.4$$

where  $\bar{\mathbf{x}}_f$  is a good estimate of  $\mathbf{x}_f^*$ ,  $\mathbf{x}_c^*$  is the optimal design based on the coarse model.

The Jacobian of  $\mathbf{P}$  is given by:

$$\mathbf{J}_P = \mathbf{J}_P(\mathbf{x}_f) = \left( \frac{\partial \mathbf{P}^T}{\partial \mathbf{x}_f} \right) = \left( \frac{\partial (\mathbf{x}_c^T)^T}{\partial \mathbf{x}_f} \right) \quad 6.5$$

An approximation to the mapping Jacobian is designated by the matrix  $\mathbf{B} \in \mathbb{R}^{n \times n}$  and can be derived as:

$$\mathbf{B} = \left( \mathbf{J}_c^T \mathbf{J}_c \right)^{-1} \mathbf{J}_c^T \mathbf{J}_f \quad 6.6$$

The mapping can then be established through the foregoing equation provided that  $\mathbf{J}_c$  is full rank and  $m \geq n$ .

### 6.2.2 Original Space Mapping Optimization Algorithm

In this approach, an initial approximation of the mapping  $\mathbf{P}^{(0)}$  is obtained by performing fine model analyses at a pre-selected set of at least  $m_0 \geq n+1$  base points. One base point may be taken as the optimal coarse model solution,  $\mathbf{x}_f^{(1)} = \mathbf{x}_c^*$  and the remaining  $m_0 - 1$  base points are chosen by perturbation. A corresponding set of coarse model points is then constructed through the Parameter Extraction (PE) process:

$$\mathbf{x}_c^{(j)} = \arg \left\{ \min_{\mathbf{x}_c} \left\| \mathbf{R}_f(\mathbf{x}_f^{(j)}) - \mathbf{R}_c(\mathbf{x}_c) \right\| \right\} \quad 6.7$$

for which

$$\varepsilon = \min_{\mathbf{x}_c} \left\| \mathbf{R}_f(\mathbf{x}_f^{(j)}) - \mathbf{R}_c(\mathbf{x}_c) \right\| \quad 6.8$$

is the PE error.

The additional  $m_0 - 1$  points apart from  $\mathbf{x}_f^{(1)}$  are required to establish full-rank conditions leading to the first mapping approximation  $\mathbf{P}^{(0)}$ . Bandler *et al.* assumed a linear mapping between the two spaces, i.e.

$$\mathbf{x}_c = \mathbf{P}^{(j)} \mathbf{x}_f = \mathbf{B}^{(j)} \mathbf{x}_f + \mathbf{c}^{(j)} \quad 6.9$$

where  $\mathbf{B}^{(j)} \in \Re^{n \times n}$  and  $\mathbf{c}^{(j)} \in \Re^{n \times 1}$ .

At the  $j^{\text{th}}$  iteration, the sets of points in the two spaces may be expanded to contain  $m_j$  points, which are used to establish the updated mapping  $\mathbf{P}^{(j)}$ . Since the analytical form of  $P$  is not available, SM uses the current approximation  $\mathbf{P}^{(j)}$  to estimate  $\mathbf{x}_f^*$  at the  $j^{\text{th}}$  iteration as:

$$\bar{\mathbf{x}}_f \approx \mathbf{x}_f^{(m_j+1)} = \left(\mathbf{P}^{(j)}\right)^{-1} \left(\mathbf{x}_c^*\right) \quad 6.10$$

The process continues iteratively until  $\mathbf{R}_f \left(\mathbf{x}_f^{(m_j+1)}\right)$  is close enough to  $\mathbf{R}_c \left(\mathbf{x}_c^*\right)$ . If so,  $\mathbf{P}^{(j)}$  is assumed close enough to the desired  $\mathbf{P}$ . If not, the set of base points in the fine space is augmented by  $\mathbf{x}_f^{(m_j+1)}$  and  $\mathbf{x}_c^{(m_j+1)}$ . Upon termination, the space-mapped design is set as in Equation 6.10.

This algorithm is simple but has pitfalls:

1. It requires  $m_0$  up-front high-cost fine model analyses.
2. A linear mapping may not be valid for significantly misaligned models.

Nonuniqueness in the PE process may lead to an erroneous mapping estimation and algorithm breakdown.



### 6.2.3 Aggressive Space Mapping (ASM) Optimization Algorithm

The aggressive space mapping (ASM) incorporates a quasi-Newton iteration using the classical Broyden formula. A rapidly improved design is anticipated following each fine model simulation, while the majority of the computational effort is carried out in the coarse model space. The ASM technique iteratively solves the following nonlinear system:

$$f(\mathbf{x}_f) = \mathbf{P}(\mathbf{x}_f - \mathbf{x}_c^*) = 0 \quad 6.11$$

The quasi-Newton step in the fine space is given by:

$$\mathbf{B}^{(j)} \mathbf{h}^{(j)} = -\mathbf{f}^{(j)} \quad 6.12$$

where  $\mathbf{B}^{(j)}$ , the approximation of the mapping Jacobian  $\mathbf{J}_p$ , is updated using Broyden's rank one update. Solving the foregoing equation for  $\mathbf{h}^{(j)}$  provides the next iterate  $\mathbf{x}_f^{(j+1)}$ :

$$\mathbf{x}_f^{(j+1)} = \mathbf{x}_f^{(j)} + \mathbf{h}^{(j)} \quad 6.13$$

The algorithm terminates if  $\|\mathbf{f}^{(j)}\|$  becomes sufficiently small. The output of the algorithm is an approximation to  $\mathbf{x}_f = \mathbf{P}^{-1}(\mathbf{x}_c^*)$  and the mapping matrix  $\mathbf{B}$ . The matrix  $\mathbf{B}$  can be obtained in several ways. In the Broyden-like updates, an initial approximation to  $\mathbf{B}$  can be taken as  $\mathbf{B}^{(0)} = \mathbf{I}$ , the identity matrix. When  $\mathbf{h}^{(j)}$  is the quasi-Newton step, the  $\mathbf{B}^{(j)}$  can be updated using Broyden's rank one formula and further simplified as:

$$\mathbf{B}^{(j+1)} = \mathbf{B}^{(j)} + \frac{\mathbf{f}^{(j+1)}}{\mathbf{h}^{(j)T} \mathbf{h}^{(j)}} \mathbf{h}^{(j)T} \quad 6.14$$

#### 6.2.4 Thrust Region Aggressive Space Mapping (TRASAM) Optimization Algorithm

The idea of trust-region methods is to adjust the length of the step taken at each of the iteration based on how well an approximate linear or quadratic model predicts the objective function. The approximate model is trusted to represent the objective function only within a region of specific radius around the current iteration. The local model minimum inside the trust region is found by solving a trust-region subproblem. If the model minimum achieves sufficient actual reduction in the objective function, the trust-region size is increased. If insufficient reduction is achieved, the trust region is reduced. Otherwise the trust region is kept unchanged.

The Trust-Region ASM algorithm integrates a trust-region with the ASM technique. Instead of using a quasi-Newton step in the ASM, a trust-region subproblem is solved within a certain trust region to minimize  $\|\mathbf{f}^{(j+1)}\|_2^2$ . The linearized objective function is thus given by:

$$\mathbf{L}^{(j)}(\mathbf{x}^{(j)}, \mathbf{h}^{(j)}) = \mathbf{f}^{(j)} + \mathbf{B}^{(j)}\mathbf{h}^{(j)} \quad 6.15$$

The next step is obtained by solving the following trust-region subproblem:

$$\mathbf{h}^{(j)} = \arg \left\{ \min_{\mathbf{h}} \|\mathbf{f}^{(j)} + \mathbf{B}^{(j)}\mathbf{h}\|_2^2 \right\} \quad 6.16$$

Subject to:

$$\|\mathbf{h}\|_2 \leq \delta^{(j)} \quad 6.17$$

Therefore, the step taken is constrained by a suitable trust region  $\delta^{(j)}$ . Solving the foregoing equations is equivalent to solving:

$$(\mathbf{B}^{(j)T}\mathbf{B}^{(j)} + \lambda\mathbf{I})\mathbf{h}^{(j)} = -\mathbf{B}^{(j)T}\mathbf{f}^{(j)} \quad 6.18$$

### 6.3 Rectangular Tube Crush Optimization Using Implicit Space Mapping

The implicit space mapping (ISM) based optimization algorithm is presented and applied to solve for a rectangular tube crush optimization problem in this section. Two models are required in the ISM optimization algorithm: coarse model and fine model. ISM takes advantage of the efficiency of the coarse model and accuracy of the fine model. The optimization process is conducted in the “cheap-to-run” optimization space based on the coarse model while the validation process is performed on the validation space using the fine model. A space mapping is established implicitly between the optimization space and validation space, as shown in Figure 6.1. The main advantage of the ISM method is that only one high-fidelity LS-DYNA finite element analysis is required for each of the design iteration. This implies that the total number of analyses required for the optimization process to achieve the optimal design and meet the crashworthiness requirements can significantly be reduced as compared to the traditional DOE/RSM based optimization methodology.

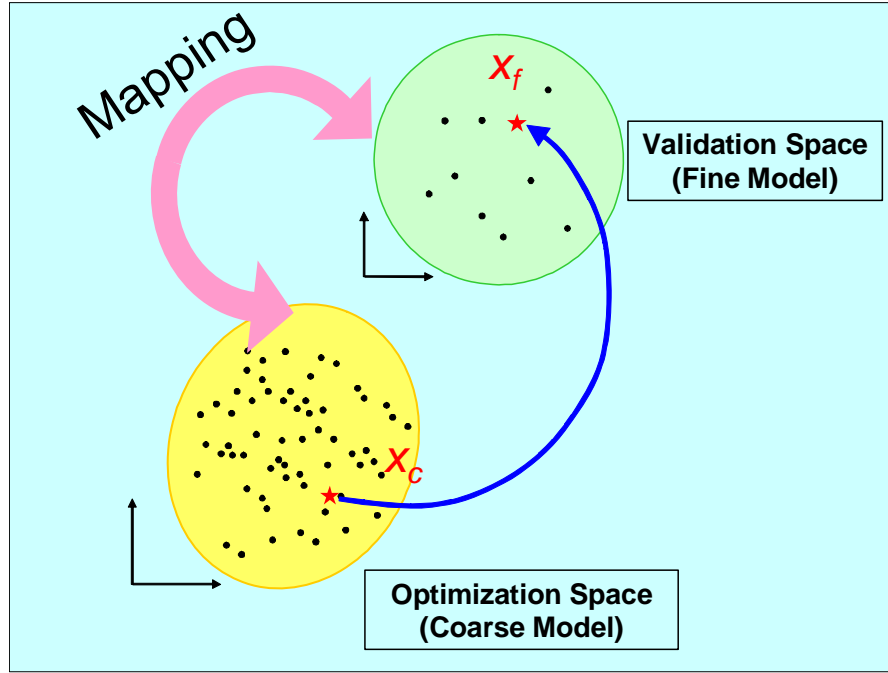


Figure 6.1 Schematic of Implicit Space Mapping Optimization Algorithm Concepts

### 6.3.1 Implicit Space Mapping Optimization Algorithm

The general design optimization problem can be formulated as:

$$\mathbf{x}_f^* = \arg \left\{ \min_{\mathbf{x}_f} U(\mathbf{R}_f(\mathbf{x}_f)) \right\} \quad 6.19$$

where  $\mathbf{x}_f^*$  is the optimal fine model design,  $U(\mathbf{R}_f(\mathbf{x}_f))$  is the scalar objective function, and  $\mathbf{R}_f$  is the fine model response. For complex engineering systems, direct solving Equation 6.19 may be prohibitive.

ISM takes advantage of the accuracy of fine model and efficiency of coarse model to match the coarse model responses with fine model responses. That is, at the  $j$ th iteration, ISM seeks to establish an implicit mapping  $Q$  between fine model space

$\mathbf{x}_f$  and coarse mode space  $(\mathbf{x}_c, \mathbf{p})$ . The preassigned parameter  $\mathbf{p}^{(j)}$  is obtained indirectly by solving an optimization problem w.r.t.  $\mathbf{p}$  for the mapping:

$$\mathbf{Q}(\mathbf{x}_f, \mathbf{x}_c, \mathbf{p}) = 0 \quad 6.20$$

such that

$$\mathbf{R}_f(\mathbf{x}_c^{*(j-1)}) \approx \mathbf{R}_c(\mathbf{x}_c^{*(j-1)}, \mathbf{p}^{(j)}) \quad 6.21$$

ISM then utilizes the mapping to obtain a prediction of  $x_f$  by optimizing a mapped coarse model as in the following:

$$\mathbf{x}_c^{*(j)} = \arg \min_{\mathbf{x}_c} U(\mathbf{R}_c(\mathbf{x}_c, \mathbf{p}^{(j)})) \quad 6.22$$

We then set the fine model design variables as

$$\mathbf{x}_f = \mathbf{x}_c^{*(j)} \quad 6.23$$

The process is repeated iteratively until

$$\left\| \mathbf{R}_f(\mathbf{x}_c^{*(j-1)}) - \mathbf{R}_c(\mathbf{x}_c^{*(j-1)}, \mathbf{p}^{(j)}) \right\| \leq \varepsilon \quad 6.24$$

In the next section, we demonstrate how to employ the ISM methodology to improve the energy absorption of a rectangular tube crush problem. Figure 6.2 illustrates the flowchart of the ISM optimization algorithm.

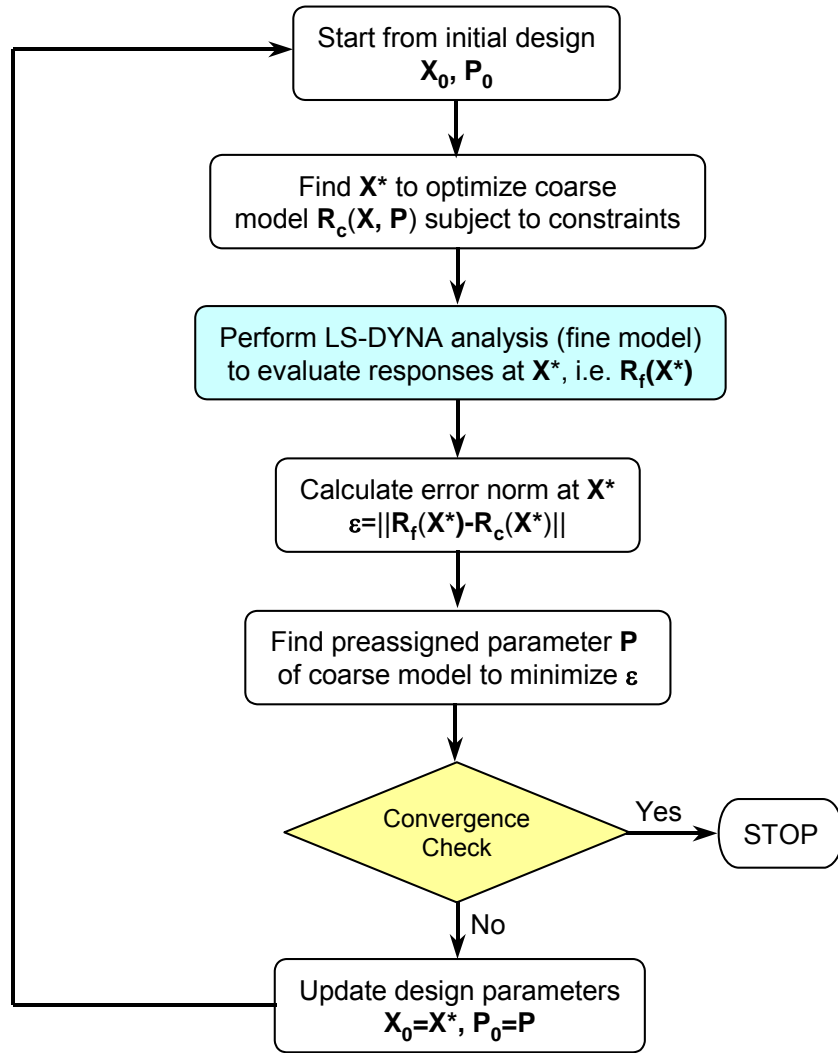


Figure 6.2 Implicit Space Mapping Optimization Algorithm

### 6.3.2 Finite Element Models

A rectangular tube crush model is developed using the explicit nonlinear finite element code, LS-DYNA, to demonstrate Crashworthiness optimization using Implicit Space Mapping (ISM) technique. Two finite element models are required in the ISM optimization: fine (high-fidelity) model and coarse (low-fidelity). Figure 6.3 shows the fine model of the rectangular tube. Note that this model is same as the one presented in

Figure 4.11. Figure 6.4 shows the coarse model of the rectangular tube, which is imposed by a rigid body with the same velocity and mass as in the fine model. The fine model contains 3,197 shell elements and 3,261 nodes while the coarse model contains 857 shell elements and 895 nodes. Note that the fine model not only has more number of elements but also has more details in crush trigger or crush initiator modeling. The critical time step 0.52  $\mu$ sec and 2.24  $\mu$ sec for the fine model and coarse model respectively. The simulation time is selected to be 20 msec. The computational time for the fine model is 5 minutes and 30 seconds while the coarse model is 30 seconds running on an IBM Intellistation with 2.8 GHz speed using 1 CPU. That is, the fine model is 11 times more expensive than the coarse model computationally.

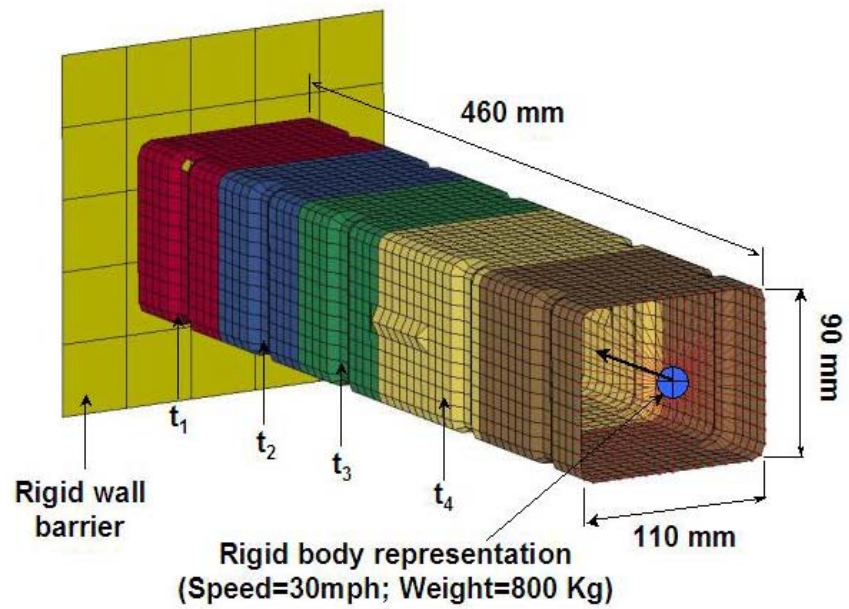


Figure 6.3 Fine LS-DYNA Finite Element Model for Rectangular Tube Crush Problem

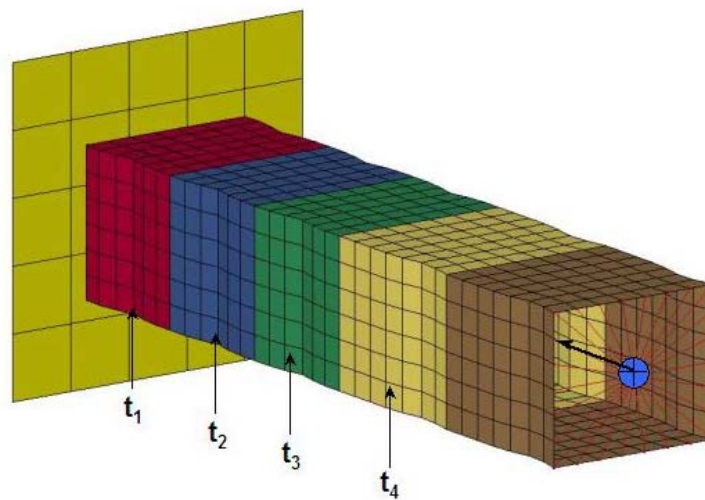


Figure 6.4 Coarse LS-DYNA Finite Element Model Rectangular Tube Crush Problem



### 6.3.3 Problem Definition

The main thrust of this problem is to increase the impact performance by increasing the internal energy while reducing or maintaining the initial crush peak force and structural weight. Four thickness design variables are selected as shown in Figures 6.1 and 6.2. The optimization problem is formulated as:

Find the thickness design variable  $x_i$  ( $i=1\sim4$ ) to

Maximize:  $IE$  6.25

Subject to:  $g_1: W \leq 3.1 \text{ kg}$

$g_2: IE_{2ms} \leq 850 \text{ J}$

$g_3: IE_3 \leq IE_4$

Side constraints  $0.7 \leq x_i \leq 3.0$

$IE_{2ms}$ : Internal energy in the first 2 msec

$IE_3$ : Internal energy of design variable component 3

$IE_4$ : Internal energy of design variable component 4

Note that we impose 15% structural weight penalty on the constraint  $g_1$ . Constraint  $g_2$  is imposed to control the initial peak force within the peak value of the baseline model. Constraint  $g_3$  is used to manage the energy distribution so that the progressive collapse mode will not initiated at the rear end of the rectangular tube. Note that the design domain in this problem is larger than the one presented in Chapter 4.

After the optimal design is found by the optimization process as shown in formulation of 6.25, the next step in the ISM optimization algorithm is to perform the parameter extraction. A preassigned (or auxiliary) parameter  $p$  needs to be selected for

the coarse model in the ISM optimization. The preassigned parameter is used to tune the coarse model so that the responses match with the fine model. Therefore the preassigned parameter must be influential to the responses. The preassigned parameters can be geometry, material property, density, dynamic property etc. In this paper, we propose to select the scale factor of the plastic strength in the material stress-strain curve as the preassigned parameter in the ISM optimization process, as shown in Figure 6.5.

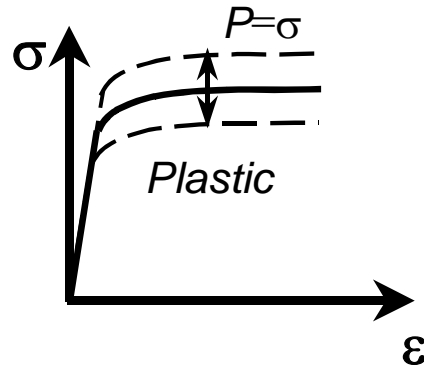


Figure 6.5 Plastic Strength Scale Factor for the Preassigned Parameter in the ISM Optimization Algorithm

Specifically, the optimization problem of the parameter extraction in the ISM process can be formulated as:

Find the preassigned parameter  $p$  to

$$\text{Minimize: } \left\| \mathbf{R}_f(\mathbf{x}^*) - \mathbf{R}_c(\mathbf{x}^*, \mathbf{p}) \right\| \quad 6.26$$

where:  $\mathbf{R}_f$ : Fine model responses

$\mathbf{R}_c$ : Coarse model responses

#### 6.3.4 Numerical Results

As discussed earlier, there are two optimization processes in the ISM optimization algorithm. The first optimization process, as formulated 6.25, is to find the optimal design of the design variables by performing the optimization on the coarse model. The second optimization process is the parameter extraction to find the optimal preassigned parameter for minimal error norm of the responses between the fine and coarse models, as formulated in 6.26. While any optimization technique can be applied to solve these two formulations, we choose the SQP gradient-based direct optimization algorithm. Using direct optimization to solve crash problem involves several technical challenges. One of the challenges is that the responses (such as forces, accelerations etc.) in the impact problem are typically very noisy due to the complex physics phenomena involved such as impact-contact algorithm, large deformation, large rotation, transient, dynamics, failure etc. The noisy behavior of these responses results in tremendous difficulty in computing ‘reliable’ sensitivity to perform direction optimization using finite difference method. To encounter the difficulty, we choose to formulate the crashworthiness optimization formulation using energy responses and

select larger step size (5%) for computing sensitivity using finite difference method in both optimization processes for formulations 6.25 and 6.26

The ISM optimization results for the rectangular tube crush problem are given in this section. Figure 6.6 shows design history of the objective functions internal energy and the error norm in the parameter extraction process. The ISM optimization process converges in three design iterations to a feasible design with no constraint violation, as shown in Figure 6.7 (design history for the normalized constraint functions) and Table 6.2. Constraint  $g_3$  is violated in the 1<sup>st</sup> design iteration and is corrected in the 2<sup>nd</sup> and 3<sup>rd</sup> design iterations. After 3 design iterations, the total internal energy (objective function) of the design variable components is increased from 5,633 J to 9,073 J (or 67% improvement) as shown in Table 6.1.

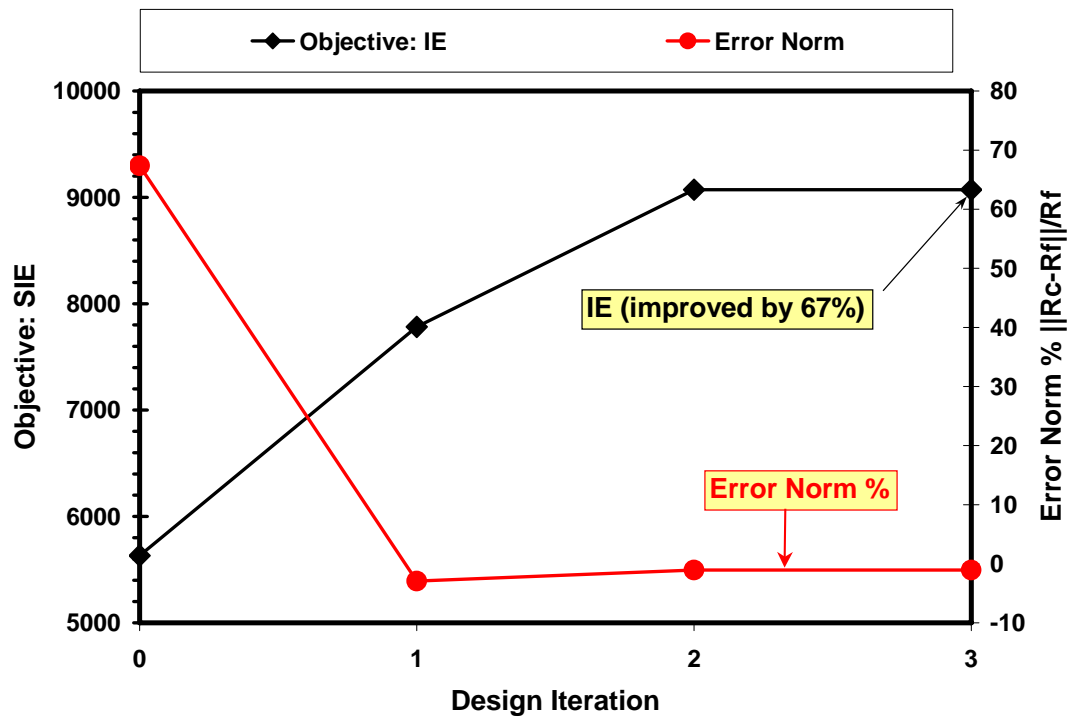


Figure 6.6 Objective Function Design History for Rectangular Tube Crush Problem Using ISM Optimization Algorithm

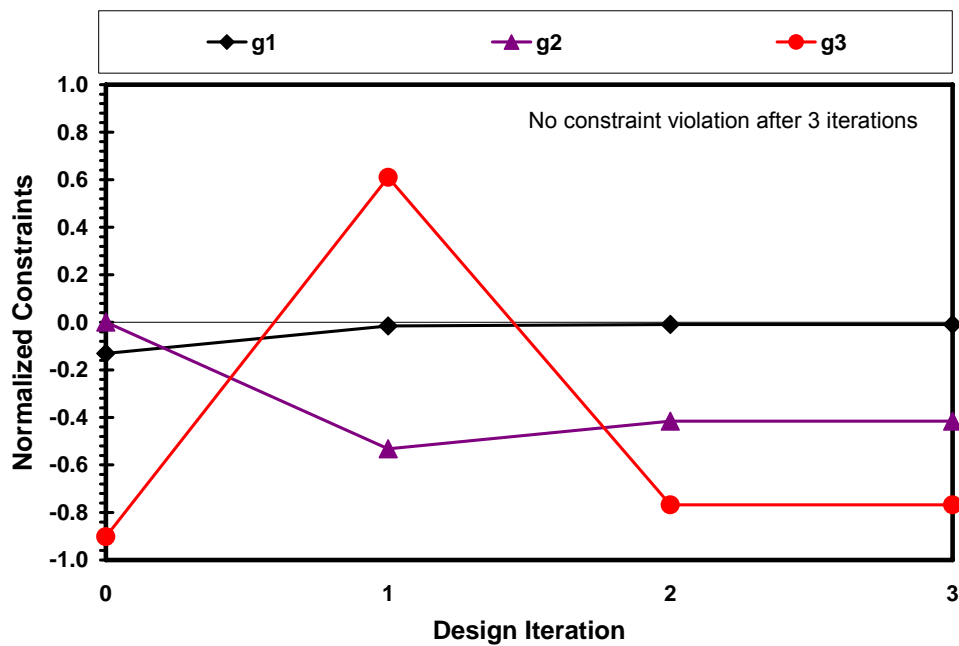


Figure 6.7 Constraint Function Design History for Rectangular Tube Crush Problem Using ISM Optimization Algorithm

Table 6.1 Design History of Structure Weight and Internal Energy for Rectangular Tube Crush Problem Using ISM Optimization Algorithm

Iteration No.	Weight (Kg)	IE <sub>1</sub> (J)	IE <sub>2</sub> (J)	IE <sub>3</sub> (J)	IE <sub>4</sub> (J)
Baseline	2.7	5633	843	1888	186
1	3.1	7784	394	471	759
2	3.1	9073	493	1626	377
3	3.1	9073	493	1626	377
Obj. or Constr.	$\leq 3.1$	Maximize	$\leq 843$	$\geq IE_4$	$\leq IE_3$

Table 6.2 Design History of Normalized Constraints, SIE and Error Norm for Rectangular Tube Crush Problem Using ISM Optimization Algorithm

Iteration No.	Objective IE	g <sub>1</sub> $W \leq 3.1$	g <sub>2</sub> $IE_2 \leq 843$	g <sub>3</sub> $IE_4 \leq IE_3$	SIE (J/Kg)	Improvement (%)	Error Norm $  Rc-Rf  /Rf$
0	5633	-0.13	0.00	-0.90	2091	0	67.4
1	7784	-0.02	-0.53	0.61	2551	22.0	-2.9
2	9073	-0.01	-0.42	-0.77	2954	41.3	-1.0
3	9073	-0.01	-0.42	-0.77	2954	41.3	-1.0

Initially, the coarse model is much stiffer than the fine model primarily due to the fact that the mesh size of the coarse model is too large. The discrepancy results in 67% of error norm of the internal energy. This error norm is minimized in the parameter extraction process by selecting a proper preassigned parameter  $p$  in the optimization process. Figure 6.6 shows that the error norm is reduced to within 1% after 3 design iterations. Figure 6.8 and Table 6.3 show the design history of the design variables and preassigned parameter. Note that the preassigned parameter is reduced from 1.0 initially to 0.634 after the 1<sup>st</sup> iteration. This also implies the stress strength of the coarse model material needs to be decreased to reduce its structural stiffness or energy absorption capability in order to match with the fine model.

Table 6.3 Design Variables and Preassigned Parameter Design History for Rectangular Tube Crush Problem Using ISM Optimization Algorithm

No.	X1	X2	X3	X4	P
0	1.500	1.500	1.500	1.500	1.000
1	1.440	0.907	3.000	1.883	0.634
2	2.220	1.027	2.340	1.757	0.634
3	2.220	1.027	2.340	1.757	0.634

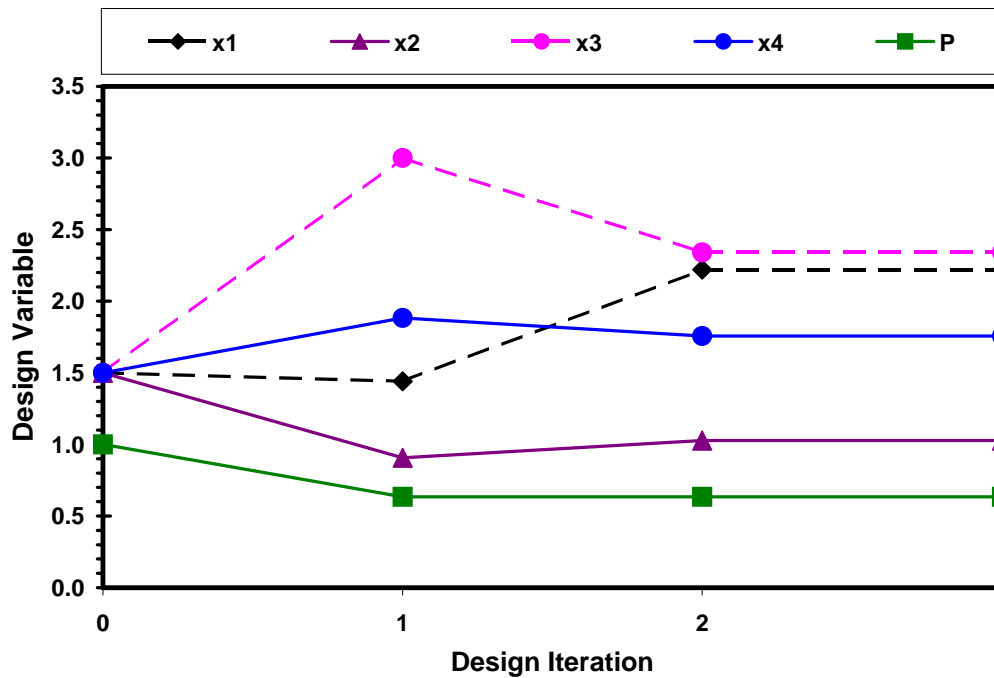


Figure 6.8 Design Variables and Preassigned Parameter Design History for Rectangular Tube Crush Problem Using ISM Optimization Algorithm

Figure 6.9 shows internal energy comparison for the design variable components between baseline and optimal designs. The optimal design absorbs 67% more energy than the baseline. With the 15% weight penalty, the optimal design improves the energy absorption efficiency by 41% in terms of SIE. It is noted that the internal energy of the optimal design in the first 2 msec is less than the baseline, which

also implies that the initial peak force is lowered, as shown in Figure 6.10. The buckling collapse mode of the optimal design is altered. It is also indicated that the second and third buckling modes of the optimal design are much higher and thus the tube is more crashworthy (i.e. more energy absorption).

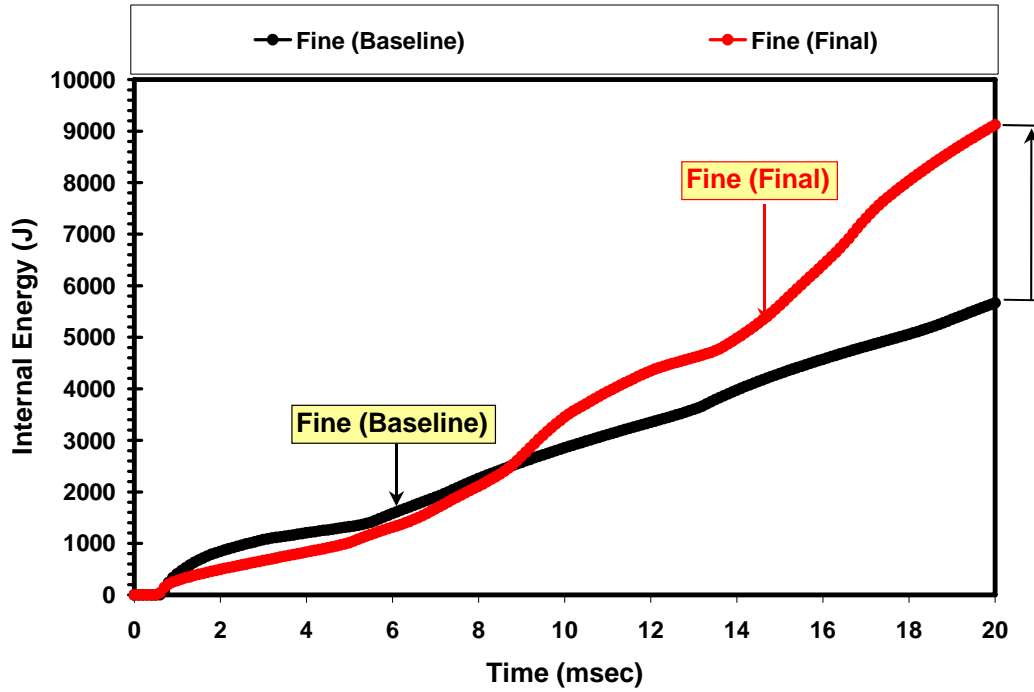


Figure 6.9 Original and Final Internal Energy Comparison for Rectangular Tube Crush Problem Using ISM Optimization Algorithm



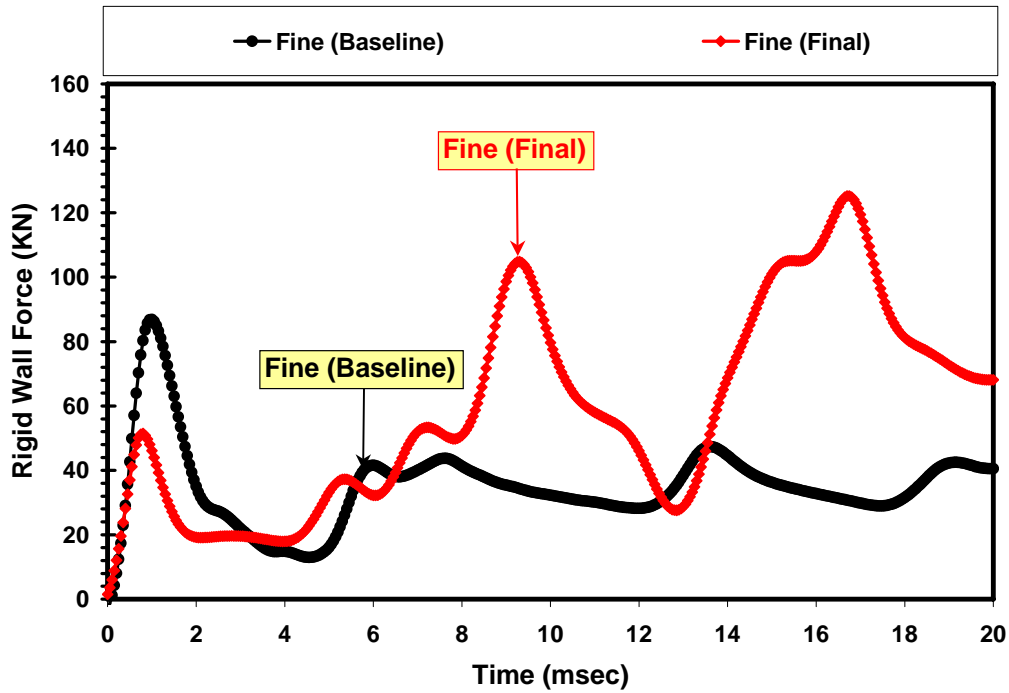
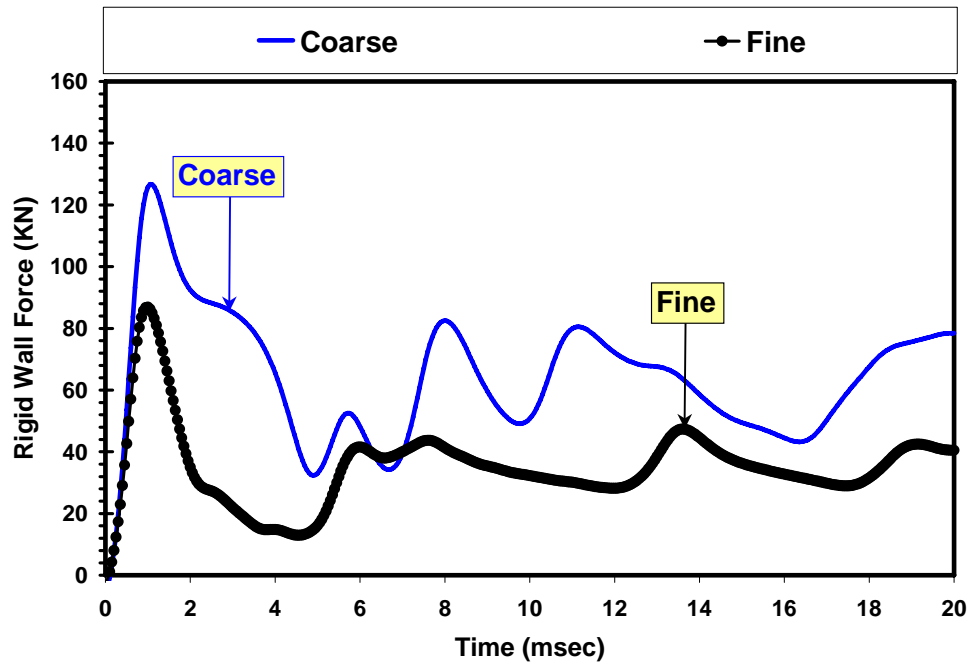


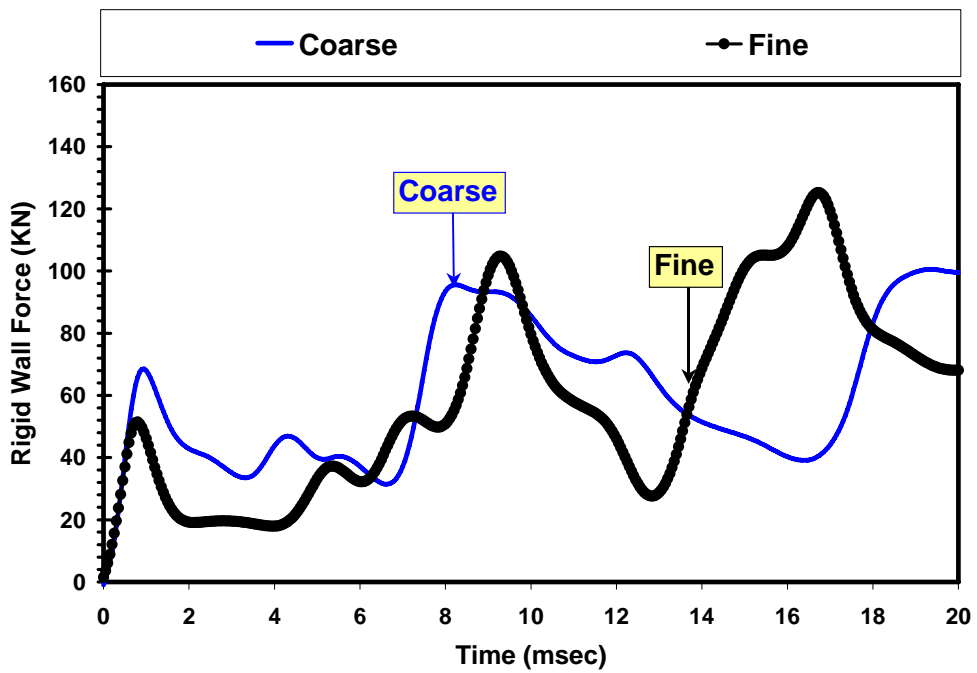
Figure 6.10 Original and Final Rigid Wall Force Comparison for Rectangular Tube Crush Problem Using ISM Optimization Algorithm

Figures 6.11 (a) and 6.11 (b) show the rigid wall force comparison of the baseline rectangular tube fine and coarse models before and after performing ISM optimization, respectively. The internal energy comparison before and after ISM is shown in Figures 6.12 (a) and 6.12 (b), respectively. It can be seen that there is significant difference in both models as the coarse model is much stiffer resulting in higher rigid wall force as well as internal energy. The internal energy of the coarse model is about 67% more than the fine model. In the parameter extraction process during the ISM optimization, the preassigned parameter  $p$  is iteratively tuned so that the coarse model responses match with the fine model within a tolerance limit. Table 6.3

shows the design history of the preassigned parameter whose initial design is 1.0. After performing ISM optimization,  $p$  converges to 0.634. The value implies how much the structural stiffness of the coarse model needs to be adjusted to favorably represent the fine model in terms of crush responses. It is clearly shown that the discrepancy is improved significantly. The error norm is reduced from 67% initially, as shown in Figure 6.12 (a), to 1% in Figure 6.12 (b) for the mapped coarse model.

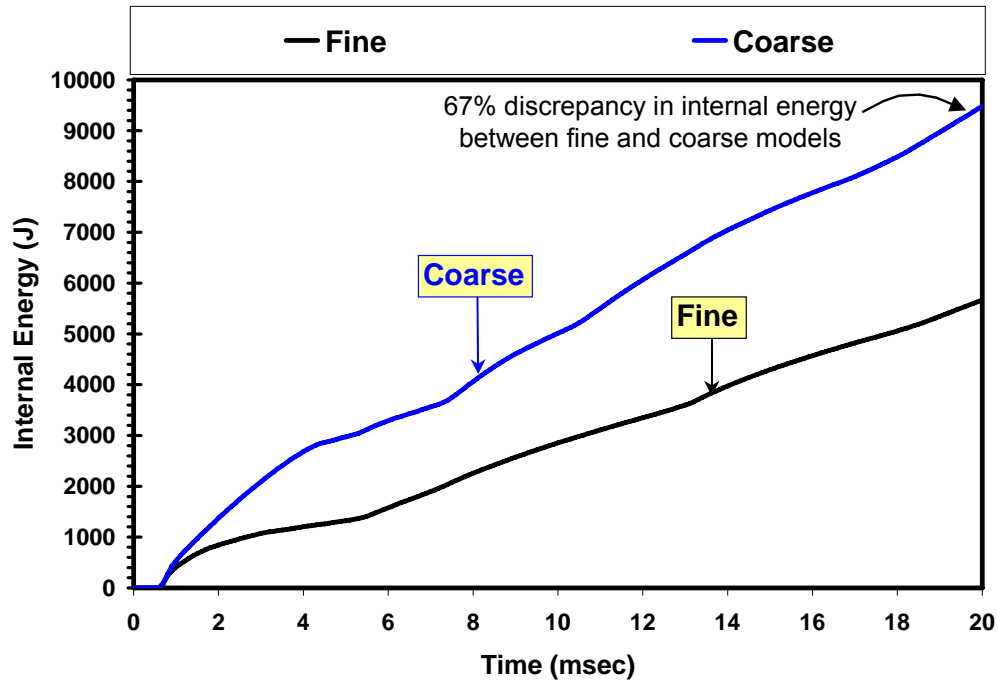


(a)

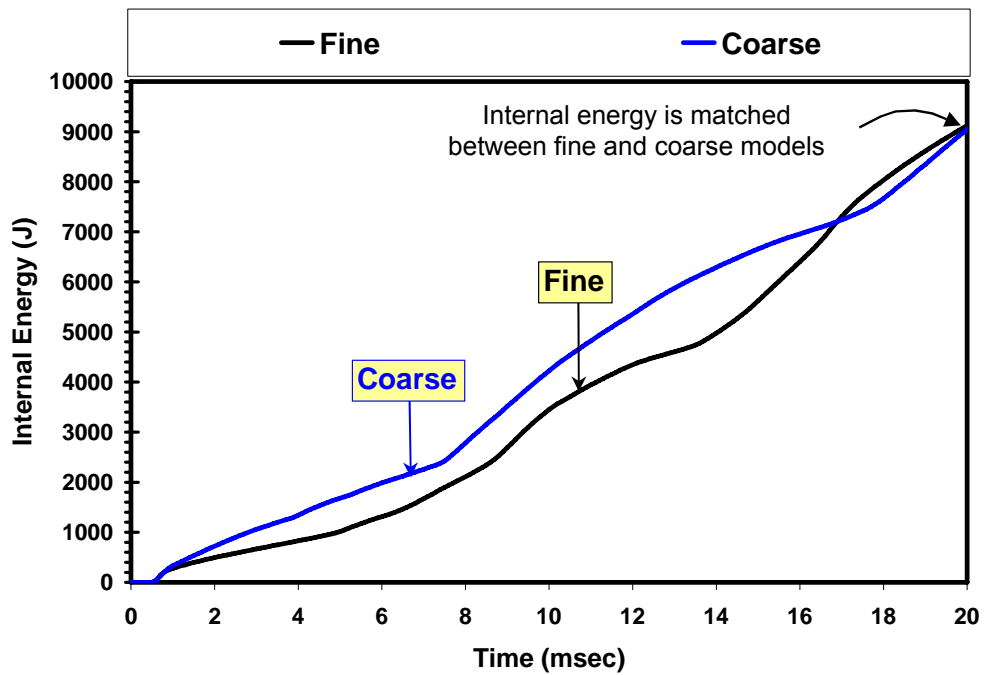


(b)

Figure 6.11 Rigid Wall Force for Rectangular Tube Crush Problem Using ISM Optimization Algorithm: (a) Before ISM, (b) After ISM



(a)



(b)

Figure 6.12 Internal Energy for Rectangular Tube Crush Problem Using ISM Optimization Algorithm: (a) Before ISM, (b) After ISM

The total structural deformation history of the baseline and optimal designs is given in Figure 6.13. While the deformation is not constrained in the optimization formulation, the total deformation of the optimal design is reduced by 2.6 mm from 166.1 mm to 163.5 mm. Figures 6.14 and 6.15 show the crash mode animation sequence for the fine model and coarse model, respectively.

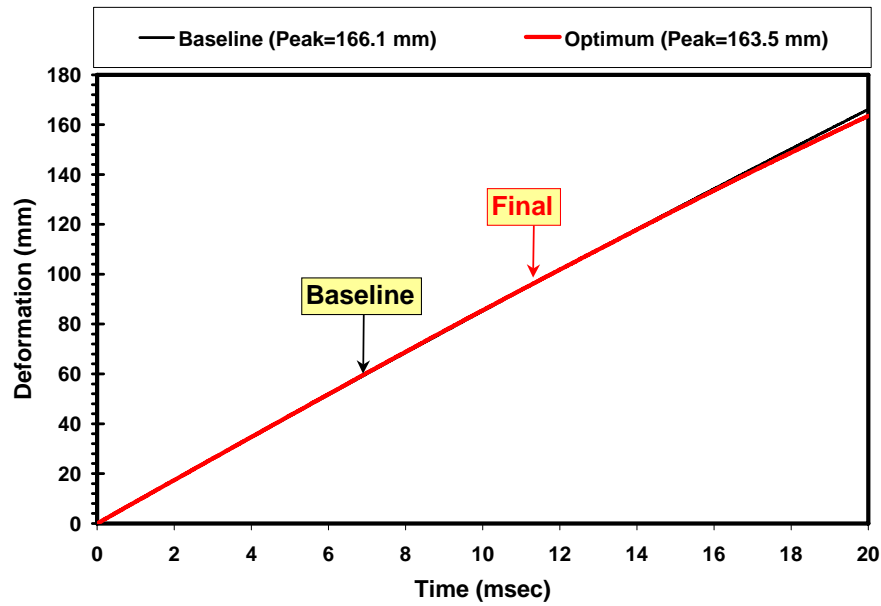


Figure 6.13 Original and Final Structural Deformation Comparison for Rectangular Tube Crush Problem Using ISM Optimization Algorithm

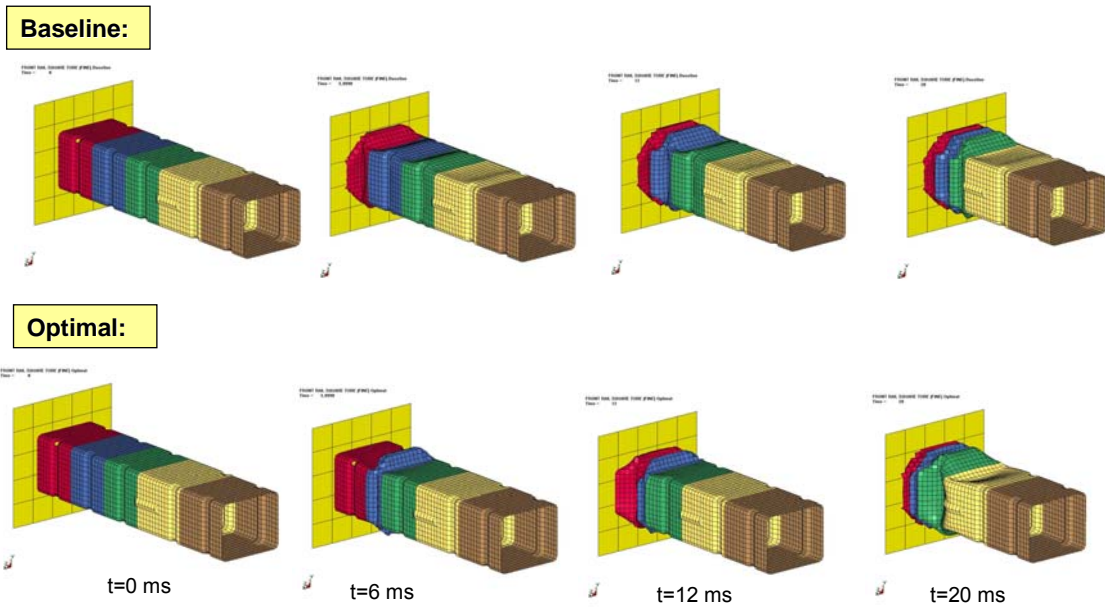


Figure 6.14 Original and Final Structural Crash Mode Comparison of Fine Model for Rectangular Tube Crush Problem Using ISM Optimization Algorithm

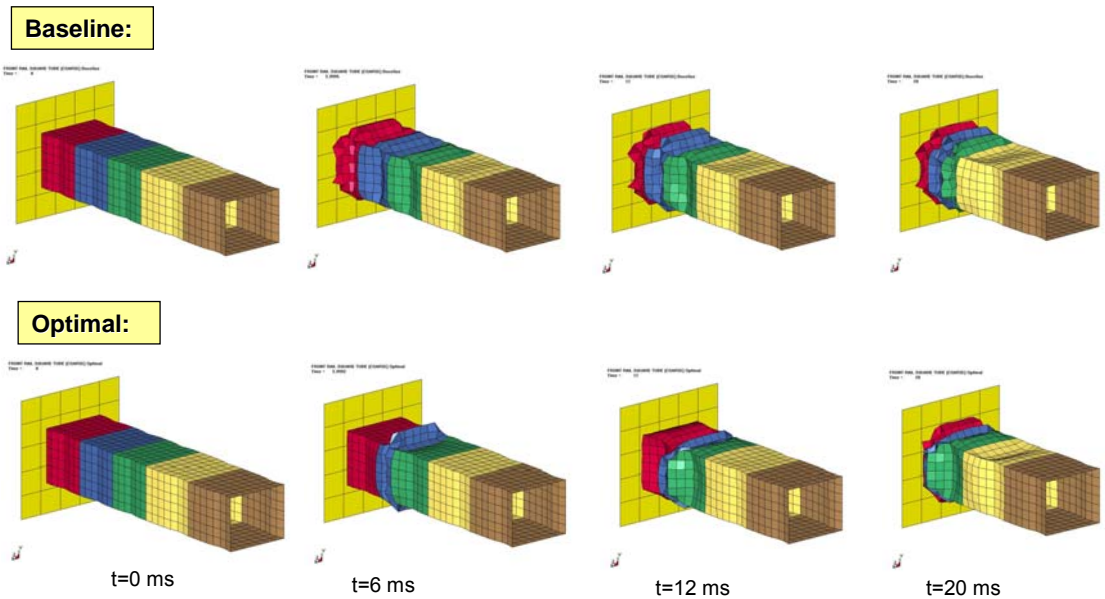


Figure 6.15 Original and Final Structural Crash Mode Comparison of Coarse Model for Rectangular Tube Crush Problem Using ISM Optimization Algorithm

## 6.4 Conclusions

In this Chapter, we have successfully demonstrated the feasibility of employing the Implicit Space Mapping (ISM) optimization methodology to improve the structural energy absorption efficiency of a rectangular tube crush problem. For the demonstrated problem, the ISM solution converged to a feasible design in three design iterations with no constraint violation. The design improved the energy absorption efficiency and increased the Specific Internal Energy (SIE) by 41% while reducing the initial peak force and maintaining the progressive collapse mode. The optimal design was achieved by using only  $1N$  high-fidelity finite element analyses as compared to the traditional DOE/RSM based methodology which typically requires at least  $3N$  to  $4N$  analyses.

Modeling the coarse finite element model is non-trivial and sometimes is very time-consuming since the ISM might not converge if the difference of the initial response between the fine model and coarse model is significant. A straightforward way to construct a coarse crash model for the nonlinear explicit analysis is to employ the mass-scaling technique by adding a lumped mass at the critical element that controls the overall numerical time step. By doing so, the computational time can be reduced significantly while the dynamic responses of the coarse model may be deviated depending on the mass scaling value. However, the responses can later be corrected in the ISM parameter extraction process through the preassigned parameter process.

## CHAPTER 7

### CONCLUSIONS AND RECOMMENDATIONS

#### 7.1 Conclusions

This dissertation has presented the crashworthiness optimization algorithms and frameworks using efficient surrogate models in lieu of expensive simulation based finite element analyses to solve for large-scale systems. The method overcomes several key technical barriers over the traditional gradient-based optimization method for nonlinear transient-dynamic crashworthiness applications: long computational time, noisy crash responses, unavailability of reliable sensitivity analysis etc. In addition, the method offers several advantages over the DOE/RSM based optimization method: large number of function evaluations or analyses for large number of design variables, low response surface accuracy for small DOE sample size.

The original contributions of this dissertation are:

1. Proposed, developed and implemented an effective and robust framework based on the Sequential Regularized Multiquadric with Output Space Mapping (SRMQ/OSM) algorithm for solving large-scale, computational expensive simulation-based design optimization problems.



2. Developed and implemented an efficient optimization framework based on the Implicit Space Mapping (ISM) technique for large-scale, nonlinear crashworthiness design optimization problems.

The proposed method has been demonstrated on several real-world crashworthiness applications including the large-scale full vehicle frontal impact optimization, hard landing of helicopter skid landing gear optimization, and rectangular tube crush optimization. The method has proven to be effective. For the demonstrated problems, as much as up to 50~70% of computational time has been reduced when compared to the traditional DOE/RSM or gradient-based optimization method.

#### 7.2 Recommendations for Future Study

The following studies are recommended to broaden the application of the proposed SRMQ/OSM and ISM based crashworthiness optimization algorithms: (1) conduct numerical convergence study; (2) systematic approach to find optimal regularization parameter; (3) systematic method to construct coarse model.

APPENDIX A

DERIVATION OF THE GENERAL FORM OF THE  
REGULARIZATON THEORY

In regularization problems, the cost function to be minimized is the summation of the standard error (or empirical error) and the structural error. That is, find the function  $F(x)$  to minimize the overall cost function  $\varepsilon(F)$ :

$$\varepsilon(F) = \frac{1}{2} \sum_{i=1}^N (y_i - F(x_i))^2 + r \|DF\|^2 = \varepsilon_s(F) + r\varepsilon_c(F) \quad \text{A.1}$$

where  $y_i$  is the  $i^{th}$  desired response,  $x_i$  is the  $i^{th}$  input vector, and  $F(\cdot)$  is the system output,  $r$  is the regularization parameter,  $D$  is a differential operator.

Note that the standard error is essentially the mean square error of the total difference between the desired response and system output where the structural error is related to the geometric property of the approximating function  $F(\cdot)$ . By differentiating Equation B.1 we obtain:

$$D^* DF(x) = \frac{1}{r} \sum_{i=1}^N (Y - F(x_i)) \delta(x - x_i) \quad \text{A.2}$$

where  $\delta(\cdot)$  is the Dirac's function. One can show that the solution of Equation B.2 is:

$$F(x) = \frac{1}{r} \sum_{i=1}^N (Y - F(x_i)) G(x, x_i) \quad \text{A.3}$$

where  $G(\cdot)$  is the Green's function. Therefore, regularization theory leads to an approximator that is an expansion on a set of Green's function  $G(x, x_i)$  of the operator  $D^* D$ . By definition, Green's function of the operation  $P$  centered in  $x_i$  is:

$$PG(x, x_i) = \delta(x - x_i) \quad \text{A.4}$$

The shape of these functions depends only on the differential operator  $D$ , i.e. on the former assumptions about the characteristics of the mapping between input and

output space. Thus the choice of  $D$  completely determines the basis functions of the approximator. In particular if  $D$  is invariant for rotation and translation Green's function is:

$$G(x, x_i) = G(\|x - x_i\|) \quad \text{A.5}$$

Note that the function is the radial basis distance that depends on the distance  $\|x - x_i\|$ .

The coefficients of the approximation in the matrix form can be expressed as:

$$C = \frac{1}{r}(Y - F) \quad \text{A.6}$$

$$F = GC \quad \text{A.7}$$

where:

$$F = \begin{bmatrix} F(x_1) \\ F(x_2) \\ \vdots \\ F(x_N) \end{bmatrix} \quad Y = \begin{bmatrix} y_1 \\ y_2 \\ \vdots \\ y_N \end{bmatrix} \quad C = \begin{bmatrix} c_1 \\ c_2 \\ \vdots \\ c_N \end{bmatrix} \quad \text{A.8}$$

$$G = \begin{bmatrix} G(x_1, x_1) & G(x_1, x_2) & \cdots & G(x_1, x_N) \\ G(x_2, x_1) & G(x_2, x_2) & \cdots & G(x_2, x_N) \\ \vdots & \vdots & \ddots & \vdots \\ G(x_N, x_1) & G(x_N, x_2) & \cdots & G(x_N, x_N) \end{bmatrix} \quad \text{A.9}$$

Finally we obtain the following expression from Equations A.6 and A.7:

$$(G + rI)C = Y \quad \text{A.10}$$

Note that the matrix  $G$  is symmetric and for some operator is positive definite. It is always possible to choose a proper value of the regularization parameter  $r$  such that  $(G + rI)$  is invertible that leads to:

$$C = (G + rI)^{-1}Y \quad \text{A.11}$$

The optimal coefficients (or weights) can be expressed as:

$$C = (G^T G + rI)^{-1} G^T Y \quad \text{A.12}$$

Note that the expression is same as Equation 4.10.

## APPENDIX B

### COMPUTER INTEGRATION IMPLEMENTATION FOR IMPLICIT SPACE MAPPING OPTIMIZAION ALGORITHM

Figure B.1 shows the flow chart the computer implementation of the ISM based crashworthiness optimization as described in Chapter 6.

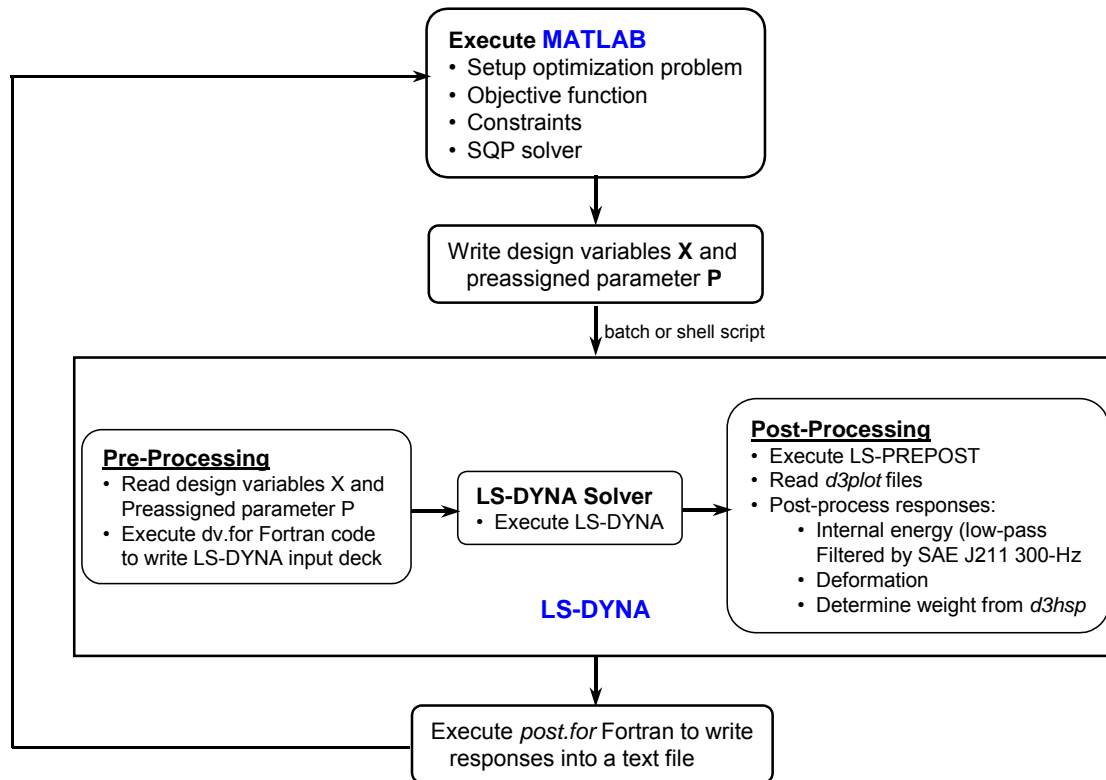


Figure B.1 Flow Chart for Implementation of ISM Based Crashworthiness Optimization

## REFERENCES

1. P. Alotto, M. Gaggero, G. Molinari, and M. Nervi, "A Design of Experiment and Statistical Approach to Enhance the Generalized Response Surface Method in the Optimization of Multim minima Problems", IEEE Transactions on Magnetics, Vol. 33, No. 2, 1897–1899, 1997.
2. J. Andersson, M. Redhe, "Response Surface Methods and Pareto Optimization in Crashworthiness Design", Proceedings of DETC'03, ASME 2003 Design Engineering Technical Conferences and Computers and Information in Engineering Conferences, DETC2003/DAC-48752, 2003.
3. J. Arora, C. Kim, and A. Mijar, "Simplified Models for Automotive Crash Simulation and Design Optimization", White Paper.
4. V. O. Balabanov, G. Venter, "Multi-Fidelity Optimization with High-Fidelity Analysis and Low-Fidelity Gradients", 10th AIAA/ISSMO Multidisciplinary Analysis and Optimization Conferences, AIAA 2004-4459, 2004.
5. M. H. Bakr, J. W. Bandler, K. Madsen, J. Sondergaard, "Review of the Space Mapping Approach to Engineering Optimization and Modeling", Optimization and Engineering, 1, 241–276, 2000.
6. M. H. Bakr, J. W. Bandler, K. Madsen, J. Sondergaard, "An Introduction to the Space Mapping Technique", Optimization and Engineering, 2, 369–384, 2001.
7. J. W. Bandler, R. M. Biernacki, S. H. Chen, P. A. Grobelny, and R. H. Hemmers, "Space Mapping Technique for Electromagnetic Optimization", IEEE Transactions on Microwave Theory and Techniques, Vol. 42, No. 12, 2536–2544, 1994.



8. J. W. Bandler, R. M. Biernacki, S. H. Chen, R. H. Hemmers, and K. Madsen “Electromagnetic Optimization Exploiting Aggressive Space Mapping”, IEEE Transactions on Microwave Theory and Techniques, Vol. 43, No. 12, 2874–2882, 1995.
9. J. W. Bandler, S. A. Dakrouy, A. S. Mohamed, M. H. Bakr, K. Madsen, J. Sondergaard, “Space Mapping: The State of the Art”, IEEE Transactions on Microwave Theory and Techniques, Vol. 52, No. 1, 337–361, 2004.
10. J. W. Bandler, Q. S. Cheng, N. K. Nikolova, M. A. Ismail, “Implicit Space Mapping Optimization Exploiting Preassigned Parameters”, IEEE Transactions on Microwave Theory and Techniques, Vol. 52, No. 1, 378–385, 2004.
11. S. D. Beattie, D. K. Lin, “Designing Computer Experiments Rotated Factorial Designs”, White Paper.
12. T. Belytschko, J. Lin and C. S. Tsay, “Explicit Algorithms for Nonlinear Dynamics of Shells”, Computer Methods in Applied Mechanics and Engineering, Vol. 17, 225–251, 1984.
13. R. Blumhardt, “FEM – Crash Simulation and Optimization”, International Journal Design, Vol. 26, No. 4, 331–347, 2001.
14. D. S. Broomhead and D. Lowe, “Multivariate Functional Interpolation and Adaptive Networks”, Complex Systems, Vol. 2, 321–355, 1988.
15. M. D. Buhmann, “Multivariate Cardinal Interpolation with Radial Basis Functions”, Constructive Approximation, Vol. 6, 225–255, 1990.
16. R. N. Cadete, J. P. Dias, M. S. Pereira, “Optimization in Vehicle Crashworthiness Design Using Surrogate Models”, 6th World Congresses of Structural and Multidisciplinary Optimization”, 2005.

17. S. Y. Chen, "An Approach for Impact Structure Optimization using the Robust Genetic Algorithm", *Finite Elements in Analysis and Design* 37, 431–446, 2001.
18. C. Cheng, E. Lee, "Fuzzy Regression with Radial Basis Function Network", *Fuzzy Sets and Systems* 119, 291–301, 2001.
19. T. Chung, Y. Lee, C. Kim, and H. Kim, "Design of Aluminum Space Frame for Crashworthiness Improvement", SAE Paper 960167, 1996.
20. G. R. Cowper and P. S. Symonds, "Strain Hardening and Strain Rate Effects in the Impact Loading of Cantilever Beams", Technical Report No. 28 from Bown University to the Office of Naval Research, 1957.
21. K. J. Craig, N. Stander, D. A. Dooge, S. Varadappa, "Automotive Crashworthiness Design Using Response Surface-Based Variable Screening and Optimization", *International Journal for Computer-Aided Engineering and Software*, Vol. 22, No. 1, 38–61, 2005.
22. N. Cressie, "Kriging Nonstationary Data", *Journal of the American Statistical Association*, 625–634, 1986.
23. M. A. Effroymsen, "Multiple Regression Analysis", *Mathematical Methods for Digital Computers* (eds A. Ralston and H. Wilf), Wiley, New York, 191–203, 1960.
24. L. Etman, J. Adriaens, M. Slaughter, A. Schoofs, "Crashworthiness Design Optimization using Multipoint Sequential Linear Programming", *Structural Optimization* 12, 222–228, 1996.
25. T. Evgeniou, M. Pontil and T. Poggio, "Regularization Networks and Support Vector Machines", *Advances in Computational Mathematics*, 13, 1–50, 2000.

26. H. Fang, M. Rais-Rohani, Z. Liu, M. F. Horstemeyer, “A Comparative Study of Metamodeling Methods for Multiobjective Crashworthiness Optimization”, *Computers and Structures*, 83, 2121–2136, 2005.
27. H. Faure, “Good Permutation for Extreme Discrepancy”, *Journal of Number Theory*, 42:47–56, 1992.
28. FHWA/NHTSA National Crash Analysis Center, The George Washington University, <http://www.ncac.gwu.edu>.
29. J. Forsberg, L. Nilsson, “Evaluation of Response Surface Methodologies Used in Crashworthiness Optimization”, *International Journal of Impact Engineering*, 32, 759–777, 2006.
30. R. Franke, “Scattered Data Interpolation: Tests of Some Methods”, *Mathematical Computation*, 48, 181–200, 1982.
31. L. A. Fredriksson, U. Schramm, “Combining Response Surface Optimization and Stochastic Analysis for Crashworthiness Design – An Introductory Study”, White Paper.
32. S. Galanti, A. Jung, “Low-Discrepancy Sequences: Monte Carlo Simulation of Option Prices”, *Journal of Derivatives*, 63–83, 1997.
33. F. Girosi, M. Jones and T. Poggio, “Regularization Theory and Neural Network Architectures”, *Neural Computation*, Vol. 7, 219–269, 1995.
34. L. Gu, R. J. Yang, C. H. Tho, M. Makowski, O. Farauque and Y. Li, “Optimization and Robustness for Crashworthiness of Side Impact”, *International Journal of Vehicle Design*, 2000.
35. J. Halquist, LS-DYNA Theoretical Manual, Livermore Software Technology Corporation, 1998.

36. J. H. Halton, "On the Efficiency of Certain Quasi-Random Sequences of Points in Evaluating Multi-Dimensional Integrals", *Numerische Mathematik*, 2:84–90, 1960.
37. R. L. Hardy, "Multiquadratic Equations of Topography and Other Irregular Surfaces", *Journal of Geophysics*, Res. 76, 1905–1915, 1971.
38. C. L. Ignatovich, A. R. Diaz, "Physical Surrogates in Design Optimization for Enhanced Crashworthiness", 9th AIAA/ISSMO Symposium on Multidisciplinary Analysis and Optimization, AIAA 2002-5537, 2002.
39. T. Ishikawa, and M. Matsunami, "An Optimization Method Based on Radial Basis Function", *IEEE Transactions on Magnetics*, Vol. 33, No. 2, 1868–1871, 1997.
40. R. Jin, W. Chen, and T. Simpson, "Comparative Studies of Metamodeling Techniques under Multiple Criteria", AIAA–2000–4801, 2001.
41. R. Jin, W. Chen, A. Sudijianto, "On Sequential Sampling for Global Metamodeling in Engineering Design", *Proceedings of DETC'02, ASME 2002 Design Engineering Technical Conferences and Computers and Information in Engineering Conference*, 2002.
42. K. Johnson, K. Bauer, J. Moore, and M. Grant, "Metamodeling Techniques in Multidimensional Optimality Analysis for Linear Programming", *Mathematical Computational Modeling* Vol. 23, NO. 5, 45–60, 1996.
43. H. Jurtaran, A. Eskandarian, D. Marzougui, N. E. Bedewi, "Crashworthiness Design Optimization Using Successive Response Surface Approximation", *Computational Mechanics*, 29, 409–421, 2002.
44. E. J. Kansa, "Multiquadrics – A Scattered Data Approximation Scheme with Applications to Computational Fluid Dynamics", *International Computational Mathematics Application*, 19, 127–145, 1990.

45. H. S. Kim, T. Wierzbicki, C. H. Tho and R. J. Yang, "Crash Optimization of an Aluminum Foam-Filled Front Side Rail", Proceedings of the 9th ASME Symposium on Crashworthiness, Occupant Protection, and Biomechanics in Transportation, 129–143, 2000.
46. H. S. Kim, Crash Behavior of Three Dimensional Thin-Walled Structures under Combined Loading, Ph.D. Dissertation, Massachusetts Institute of Technology, 2001.
47. J. Kleijnen, R. Sargent, "A Methodology for Fitting and Validating Metamodels in Simulation", European Journal of Operational Research, 120, 14–29, 2000.
48. D. Kocman, "Bending Collapse of Rectangular Section Tubes in Relation to the Bus Roll Over Problem", Ph.D. Dissertation, Cranfield Institute of Technology, Cranfield, England, 1979.
49. S. Kodiyalam, J. S. Lin and B. A. Wujek, "Design of Experiments Based Response Surface Models for Design Optimization", iSIGHT technical paper.
50. S. Kodiyalam, J. S. Sobieski, "Multidisciplinary Design Optimization – Some Formal Methods, Framework Requirements, and Application to Vehicle Design", International Journal Vehicle Design, Vol. 25, No. ½, 2001.
51. T. Krishnamurthy, "Comparison of Response Surface Construction Methods for Derivative Estimation Using Moving Least Squares, Kriging and Radial Basis Functions", 46th AIAA/ASME/ASCE/AHS/ASC Structures, Structural Dynamics & Materials Conference, AIAA 2005–1821, 2005.
52. H. Kurtaran, A. Eskandarian, D. Marzougui, N. E. Bedewi, "Crashworthiness Design Optimization Using Successive Response Surface Approximations", Computational Mechanics 29, 409–421, 2002.

53. L. Lanzi, L. Castelletti, M. Anghileri, “Multi-Objective Optimization of Composite Absorber Shape Under Crashworthiness Requirements”, *Composite Structures* 65, 433–441, 2005.
54. P. Lancaster and K. Salkauskas, *Surfaces Generated by Moving Least Squares Methods*, *Math Comp.*, 37, 141–158, 1981.
55. S. Lu and D. K. Cheng, “Building Layered Models to Support Engineering Decision Making: A Machine Learning Approach”, *Journal of Engineering of Industry*, ASME Transactions 13(1), 1–9, 1991.
56. H. F. Mahmood, A. Paluszny, “Axial Collapse of Thin Wall Cylindrical Column”, *Fifth International Conference on Vehicular Structural Mechanics*, SAE Paper No. 840727, 1984.
57. T. Masanori and A. Funahashi, “Energy Absorption by the Plastic Deformation of Body Structural Members”, SAE Paper No. 780368, 1978.
58. C. L. Magee, P. H. Thornton, “Design Consideration in Energy Absorption by Structural Collapse”, SAE Paper No. 780434, 1978.
59. D. B. McDonald, W. J. Grantham, W. L. Tabor, “Response Surface Model Development for Global/Local Optimization using Radial Basis Function, 8th AIAA/ NASA/ USAF/ ISSMO Symposium on Multi-disciplinary Analysis and Optimization, 2000.
60. M. McKay, R. Beckman and W. Conover, “A Comparison of Three Methods for Selecting Values of Input Variables in the Analysis of Output from a Computer Code”, *Technometrics* 21(2), 239–245, 1979.

61. H. Miura, Y. Umezu, M. Harada, S. Kodiyadam, "Improvement of Crash Characteristics through a Design Optimization Application", iSIGHT technical paper.
62. W. Morokoff, and R. Caflisch, "Quasi-Monte Carlo Integration", Journal of Computational Physics, 122, 218–230, 1995.
63. A. A. Mullur, A. Messac, "Higher Metamodel Accuracy Using Computationally Efficient Pseudo Response Surfaces", 46th AIAA/ASME/ASCE/AHS/ASC Structures, Structural Dynamics & Materials Conferences, AIAA 2005–2058, 2005.
64. R. H. Myers, and D. C. Montgomery, "Response Surface Methodology: Process and Product Optimization Using Designed Experiments", John Wiley & Sons, New York, 1995.
65. N. O. Myklestad, K L. Lawrence, "Transient Beam Response Calculations Using Euler's Method", Journal of American Institute of Aeronautics and Astronautics, 1967.
66. H. Niederreiter, "Random Number Generation and Quasi-Monte Carlo Methods", CBMS-NFS Regional Conference Series in Applied Mathematics, 63, 1992..
67. Y. Ohkubo *et al.*, "Mean Crushing Strength of Closed-Hat Section Members", SAE Paper No. 740040, 1974.
68. H. D. Patterson, "The Erros of Lattice Sampling", Journal of the Royal Statistical Society, Series B, 16, 140–149, 1954.
69. A. Polynkin, F. Keulen, V. Toropov, "Optimization of Geometrically Nonlinear Thin-Walled Structures using the Multipoint Approximation Method", Structural Optimization 9, 106–116, 1995.

70. M. Redhe, L. Eng, L. Nilsson, "Using Space Mapping and Surrogate Models to Optimize Vehicle Crashworthiness Design", 9th AIAA/ISSMO Symposium on Multidisciplinary Analysis and Optimization, AIAA 2002-5536, 2002.
71. M. Redhe, L. Nilsson, "Structural Optimization Using Space Mapping and Surrogate Models", 7th International LS-DYNA Users Conference, 2002.
72. M. Redhe, L. Nilsson, "A Multipoint Version of Space Mapping Optimization Applied to Vehicle Crashworthiness Design", Structural Multidisciplinary Optimization 31: 134-146, 2006.
73. R. Rikards, "Elaboration of Optimal Design Models for Objects from Data of Experiments", Optimal Design with Advanced Materials, 1993.
74. W. J. Roux, N. Stander, and R. T. Haftka, "Response Surface Approximation for Structural Optimization", International Journal for Numerical Methods in Engineering, 42, 517-534, 1998.
75. J. Sacks, S. B. Schiller, W. J. Welch, "Designs for Computer Experiments", Technometrics, Vol. 31, No. 1, 41-47, 1989.
76. U. Schramm, D. Schneider, H. Thomas, "Structural Optimization in Occupant Safety and Crash Analysis", OptiCON'98, California, 1998.
77. U. Schramm, H. Thomas, "Crashworthiness Design Using Structural Optimization", AIAA 98-4729, 1998.
78. T. Simpson, J. Allen, and F. Mistree, "Spatial Correlation Metamodels for Global Approximation in Structural Design Optimization", Proceedings of DETC98, ASME Design Engineering Technical Conference, 1998.
79. T. Simpson, T. Mauery, J. Korte, F. Mistree, "Comparison of Response Surface and Kriging Models for Multidisciplinary Design Optimization", 7th



AIAA/USAF/NASA/ISSMO Symposium on Multidisciplinary Analysis & Optimization, Vol. 1, 381–391, 1998.

80. J. S. Sobieski, S. Kodiyalam, R. J. Yang, “Optimization of Car Body under Constraints of Noise, Vibration, and Harshness (NVH), and Crash”, 41st AIAA Structures, Structural Dynamics and Materials, 2000.
81. I. M. Sobol, “The Distribution of Points in a Cube and the Accurate Evaluation of Integrals (in Russian”, *Ah. Vychisl. Mat. I Mat. Phys.*, 7:784–802, 1967.
82. N. Stander, W. Roux, M. Giger, M. Redhe, N. Fedorova, J. Haarhoff, “A Comparison of Metamodeling Techniques for Crashworthiness Optimization”, 10th AIAA/ISSMO Multidisciplinary Analysis and Optimization Conference, AIAA 2004-4489, 2004.
83. N. Stander, W. Roux, M. Giger, M. Redhe, N. Fedorova, J. Haarhoff, “Crashworthiness Optimization in LS-OPT: Case Studies in Metamodeling and Random Search Techniques”, 4th European LS-DYNA Users Conference, 2003.
84. C. H. Tho, C. Sparks, A. Sareen, M. Smith, C. Johnson, “Efficient Helicopter Skid Landing Gear Dynamic Drop Simulation Using LS-DYNA”, Journal of the American Helicopter Society, Vol. 49, No. 4, 483–492, 2004.
85. C. H. Tho, R. J. Yang and B. P. Wang, "Metamodeling Techniques for Large-Scale Crash Optimization Problems", Symposium on Design Optimization Applications in Industry, 6th U. S. National Congress on Computational Mechanics, 2001.
86. A. N. Tikhonov, “Solution of Incorrectly Formulated Problems and the Regularization Method”, Soviet Mathematic. Doklady., 4:1035–1038, 1963..

87. V. Toropov, A. Filatov and A. Polynkin, "Multiparameter Structural Optimization using FEM and Multipoint Explicit Approximations", *Structural Optimization* 5, 7–14, 1993.
88. B. P. Wang, "Parameter Optimization in Multiquadric Response Surface Approximations", *Structural and Multidisciplinary Optimization*, Vol. 26, No. 3–4, 219–223, 2004.
89. B. P. Wang, "Parameter Optimization in Radial Basis Function Response Surface Approximations", *Proceedings of 43rd AIAA/ASME/ASCE/AHS/ACS Structure, Structural Dynamics and Material Conference*, Denver, Colorado, AIAA-2002-1344, 2002.
90. X. Wang, Y. Liu, E. Antonsson, "Fitting Functions to Data in High Dimensional Design Space", *Proceedings of DETC'99, 1999 ASME Design Engineering Technical Conference*, 1999.
91. T. Wierzbicki and T. Akerstrom, "Dynamic Crushing of Strain Rate Sensitive Box Columns", *SAE Paper No. 770592*, 1977.
92. T. Wierzbicki, W. Abramowics, "On The Crushing Mechanics of Thin-Walled Structures", *Journal of Applied Mechanics*, Vol. 50, 727–773, 1983.
93. T. Vasylykevych, I. Skrypnyk, J. Spoormaker, "Optimization of Plastic Products Against Buckling using Multipoint Approximation Method and Nonlinear Visco-Elasticity Model", *White Paper*, 2001.
94. R. J. Yang, L. Tseng, L. Nagy, J. Cheng, "Feasibility Study of Crash Optimization", *Proceedings of the American Society of Mechanical Engineers, DE-Vol. 69-2, Advances in Design Automation*, 549–556, 1994

95. R. J. Yang, C. H. Tho, C. C. Wu, D. Johnson, J. Cheng, "A Numerical Study of Crash Optimization", Proceedings of DETC 99, 1999 ASME Design Engineering Technical Conferences, 1999.
96. R. J. Yang, L. Gu, Y. Fu, C. H. Tho, "Experience with Sequential Stochastic Design Improvement Methods", Proceedings of the Second MIT Conference on Computational Fluid and Solid Mechanics, Cambridge, 2003.
97. R. J. Yang, L. Gu, C. H. Tho, "Recent Development in Multidisciplinary Design Optimization of Vehicle Structures", 9th AIAA/ISSMO Symposium on Multidisciplinary Analysis and Optimization, Atlanta, 2002.
98. R. J. Yang, L. Gu, C. H. Tho, K. K. Choi, B. D. Youn, "Reliability-Based Multidisciplinary Design Optimization of a Full Vehicle System", 43rd AIAA/ASME/AHS/ASC Structures, Structural Dynamics, and Materials, 2002.
99. R. J. Yang, N. Wang, C. H. Tho, J. P. Bobineau and B. P. Wang, "Metamodeling Development for Vehicle Frontal Impact Simulation", Proceedings of the ASME 2001 Design Engineering Technical Conference, Pittsburgh, Pennsylvania, September 9-12, DETC-2001/DAC-21012, 2001.
100. R. J. Yang, L. Gu, C. H. Tho, J. Sobieszczanski-Sobieski, "Multidisciplinary Design Optimization of a Full Vehicle with High Performance Computing", 42nd AIAA/ASME/AHS/ASC, Structures, Structural Dynamics, and Materials, AIAA 2001-1273, 2001.
101. R. J. Yang, L. Gu, L. Liaw, C. Gearhart, C. H. Tho, X. Liu and B. P. Wang "Approximations for Safety Optimization of Large Systems", Proceedings of the ASME 2000 Design Engineering Technical Conference, Baltimore, Maryland, September, DETC2000/DAC-14245, 2000.

## BIOGRAPHICAL INFORMATION

Cheng-Ho Tho received his Master of Science in Mechanical Engineering focusing on Solid Mechanics from the University of Texas at Arlington in 1997. After graduation, he worked as a Research Engineer at the Ford Research Laboratory of Ford Motor Company from 1998 to 2002 to develop vehicle crash safety optimization and robustness methodology.

Cheng-Ho is currently an Engineering Specialist at the Flight Technology and Simulation Department (Structural Dynamics Group) of Bell Helicopter Textron Inc since 2002. Since joining Bell Helicopter, he has been involved in the Survivable, Affordable, Repairable Airframe Program (SARAP) and NRTC/RITA R&D programs working on advanced crashworthy energy attenuating structures. His current responsibilities are to develop advanced survivability technology for tiltrotors and helicopters, including developing nonlinear crashworthiness modeling and simulation methodologies for fluid-structural interaction problems such as bird strike analysis, rotorcraft external airbag protection system, helicopter fuel tank drop impact analysis, fuselage multi-terrain impact analysis etc.

Cheng-Ho was the winner of the Robert Lichten Award (National level) for the best technical paper presented by the American Helicopter Society in 2003. He has also won several awards across the Textron business units, including the most prestigious Textron Chairman's award for developing an innovative method for impact analysis in

2006, the Bell and Textron Systems Innovation award in 2006, as well as the Lawrence D. Pioneer award for innovation excellence presented by Bell Helicopter Textron Inc in 2006.